DYNAMICS OF A PULSE DETONATION ENGINE DRIVEN LINEAR POWER GENERATOR

by

UMANG UMESHKUMAR DIGHE

Presented to the Faculty of the Graduate School of
The University of Texas at Arlington in Partial Fulfillment
of the Requirements
for the Degree of

DOCTOR OF PHILOSOPHY

THE UNIVERSITY OF TEXAS AT ARLINGTON
December 2019

To my mother,

who set the example and made me who I am.

To my father,

who saw the dream and always stood by me.

To my sister Utkarsha,

who gave me the clarity and strength to keep going.

I could not have done this without all three of you.

ACKNOWLEDGEMENTS

I would like to express my gratitude to Prof. Frank Lu for his support and guidance throughout my time as a graduate student at the University of Texas at Arlington. I am grateful to him for providing an amicable environment and trusting me with many responsibilities. I really appreciated the raquetball sessions and the discussions I had with Prof. Lu after long days at the Aerodynamics Research Center.

I would like to thank Dr. Donald Wilson, Dr. Brian Dennis, Dr. Daejong Kim and Dr. Michael Niestroy for serving on my dissertation committee. Their valuable feedback during my comprehensive exam helped improve the overall quality of the work presented in this dissertation.

I greatly acknowledge the meaningful discussions I had about my work with colleagues and friends at the Aerodynamics Research Center. The discussions with Vijay Gopal, Nandakumar Vijaykumar, Rohit Pulimidi and Ananth Jayamani were particularly helpful and encouraging.

I would like to thank all of the MAE staff, past and present, for their help and encouragement while I have been at UTA. I especially want to thank Mr. David Carter for his support and for keeping us safe at an experimental facility.

During my stay in Arlington, I was lucky to have many amazing apartment mates over the past ten years. Saifullah Shaikh, Adeetya Ravisankar, Ninad Kawle, Kiriti Mamidi, Harish Raja and Srinivasan Venkadasamy have become my extended family away from home and I really appreciate their help and support during challenging times. I am also thankful to my past apartment mates Sumit Patel and Sunil

Subeydhi. They were instrumental in helping me navigate a new country as a young student.

I am thankful to Kedar Durve, Preeti Durve, Neha Bhanot, Ajay Sharma and Amelia Sharma for their support during the past ten years and helping me make Arlington a home away from home. I am grateful to Kshitija Gavand for her patience, for pushing me to be a better person and encouraging me to be brave and chase my dreams.

Most importantly, I cannot thank my family enough for being the wind beneath my wings. They were all the way across the world but never far away. Without the support and sacrifices of my mother, father and, sister, I would have never pursued and completed a doctoral degree and for that, I will be forever grateful.

November 25, 2019

ABSTRACT

DYNAMICS OF A PULSE DETONATION ENGINE DRIVEN LINEAR POWER GENERATOR

Umang Umeshkumar Dighe, Ph.D.
The University of Texas at Arlington, 2019

Supervising Professor: Frank K. Lu

The dynamics of a pulse detonation engine driven linear power generator were studied. For an ideal pulse detonation engine, the thrust generated is in the form of a piecewise function given by the Endo–Fujiwara model. Nonlinear electromagnetic damping is also introduced in the system due to the rare earth permanent magnets present in the linear generator architecture. Various linear generator topologies were studied using static magnetic analysis. Two configurations of a single degree-of-freedom oscillator system, one with a linear spring restoring force and another with geometric nonlinear spring restoring force, were investigated to study any potential advantages of using nonlinear spring restoring force. The governing equations for the coupled system in both cases are nonsmooth, nonautonomous, and nonlinear. As closed-form solutions for the governing equations do not exist, numerical simulations are required to understand the dynamics and power generation characteristics of the system. Special treatment is needed in the neighborhood of the discontinuity hypersurface to locate the discontinuity and continue the integration of the governing equations.

The governing equations for two configurations of the coupled pulse detonation engine and linear generator were numerically integrated using adaptive Runge–Kutta method. The power generated using the geometric nonlinear spring was considerably higher compared to the configuration with linear springs for low values of non-dimensional parameter β.

The study of the stability of the coupled system under unsteady and intermittent loading is carried out using a Poincaré map and its Jacobians. As the dynamical system is characterized by a multi-segment problem, a Poincaré map attached to each discontinuity surface is first generated. Then, using the notions of embedding and projection, a composite differentiable Poincaré map is generated and its Jacobian is used to determine the stability characteristics of the coupled system. The results of stability analysis are verified using Lyapunov exponents derived from the time-series simulation data. For all the configurations studied, the maximal Lyapunov exponent approached a value of zero, indicating a critically stable system.

In lieu of carrying out numerical simulations for each set of parameter values, bifurcation analysis enables the study of the persistence of periodic solutions under variation of parameters. Using the Poincaré maps, Jacobians and continuation methods, a bifurcation analysis was carried out. In all the cases studied, period doubling and Neimark–Sacker bifurcations were observed. Tangent bifurcation was not observed in any of the cases studied.

TABLE OF CONTENTS

Appendix

LIST OF ILLUSTRATIONS

LIST OF TABLES

Table Page

NOMENCLATURE

A	Piston surface area impacted by PDE exhaust
B	Magnetic field in LPG stator tooth
C	Damping coefficent
c	Number of cables in LPG stator slot
d	Width of LPG stator side
F	Force
I	Current at the terminals of generator
k	Spring constant
L	Circuit inductance
m	Mass of translator including piston
n	Total number of poles
P	Output power of generator
q	Winding ratio
$R, \mathbb{R}$	Resistance
$\mathbf{R}$	Set of Real numbers
t	Time
V	Voltage at the terminals
w	Width
z	Position of translator
$\dot{z}$	Velocity of translator
$\ddot{z}$	Acceleration of translator
γ	Ratio of specific heats at constant pressure and volume of gas mixture

δ	Equivalent Load angle
θ	Electric position
λ	Eigenvalues of Jacobian matrix
μ	Generator efficiency
τ	Period of solution orbit
$\boldsymbol{\varphi}, \mathbf{\Phi}$	Solution orbit vector
Ψ	Magnetic flux
ω	Electric angular frequency

Subscripts

cj	Time at which detonation wave breaks out from the open end of PDE
em	Electromagnetic
ex	Time at which $p_w = p_1$
ext	External
p	Pole
pl	Time at which thrust plateau ends
t	Tooth
w	Closed end of a PDE tube
1	Undisturbed region ahead of detonation wave
2	Chapman–Jouguet surface of detonation wave
3	Rear boundary of decelerating rarefaction wave

Abbreviations

LPG	Linear power generator
PDE	Pulse detonation engine

CHAPTER 1

INTRODUCTION

1.1 Motivation

In recent decades, energy shortage has increasingly become a major challenge. New and innovative technologies to generate electricity are being researched by scientists all over the world. Even though the world is transitioning to a renewable energy future, the majority of power generation in the world still relies on conventional fossil fuel sources. Natural gas and coal still remain the biggest fuel sources for power plants around the world. In this scenario, any improvement in the efficiency of converting these fossil fuels to electricity will have a global impact on the availability of total power and also on the carbon footprints of power plants.

Conventional power plants around the world use a process known as deflagration to convert the chemical energy stored in the fossil fuels to heat and then- converting to electricity. Although deflagration has been pivotal in the development of human civilization, it is theoretically not the most efficient way to convert chemical energy to other forms of energy. A different form of combustion, namely, detonation, has been studied extensively since the late 19th century. The early interest in detonations revolved around mining and in military applications. In the past few decades, the possibility of using detonation to generate electricity has been explored by many researchers. Several patents have also been issued for concepts that involve coupling a detonation-based engine with different systems to drive a generator to produce electricity. [8–10]

Braun et al. [11] investigated the possibility of converting the kinetic energy of propagating detonation waves to electricity and experimentally studied a coupled detonation engine–linear generator concept. In preliminary studies, the pulse detonation engine (PDE) thrust was modeled using the Friedlander equation [12] and the system damping did not account for the electromagnetic damping arising from the linear generator. In the current study, the PDE thrust is modeled using the Endo–Fujiwara model [4], which represents the PDE thrust more accurately. The electromagnetic damping from the linear generator is also modeled into the governing equations for the coupled PDE–LPG system. As a result, the coupled system is modeled as a mass-spring-damper system with electromagnetic damping and a piecewise continuous excitation force.

The various possible configurations of the mass-spring-damper system, the intermittent and thrust generated by the PDE and the time-varying electromagnetic damping of the linear generator make this an interesting and challenging research topic. In the nonlinear configuration with a piecewise continuous external loading, the numerical simulation of the governing equation of the coupled system requires careful treatment of the discontinuity and is capable of highlighting interesting dynamics that may affect the power generation and stability of the system.

The first step towards properly understanding the energy conversion setup is to understand the phenomenon of detonation. Therefore, a brief description of the detonation phenomenon is given below. The subsequent chapters discuss the pulse detonation engine, the linear generator, the coupled system, and its dynamics.

1.2 Fundamentals of Detonations

1.2.1 What is Detonation?

The possibility of utilizing a train of detonation waves in a propulsion device or for energy conversion has attracted significant attention over the past few decades [13]. A pulse detonation engine (PDE) is an example of a practical application of using detonation waves. PDEs have higher theoretical efficiencies, have fewer moving parts and are easy to manufacture and maintain than conventional turbomachinery-based engines.

In general, there are two types of self-propagating combustion waves, namely, deflagration and detonation. While deflagration is the commonly known subsonic combustion, detonation is a supersonic form of combustion which involves a reacting shock wave. After the ignition of the reactant mixture, a combustion wave forms and propagates away from the ignition source. As the combustion wave propagates, it burns the reactant mixture. The combustion wave produces burned products at drastically different pressure, temperature, and velocity depending on whether a deflagration or detonation wave transformed the combustible mixture. The formation of a deflagration wave or a detonation wave in the combustible mixture is governed by the initial mixture composition, ignition source, and boundary conditions, i.e., the manner of confinement of the reactant mixture [14]. Hence, it is useful to understand the conditions that lead to each type of combustion wave.

The mechanisms governing the propagation of deflagration and detonation waves through a reactant mixture is described by Glassman and Yetter [6]. In a long tube with both ends open, if the reactant mixture is ignited, a self-propagating deflagration wave traveling with a relatively low subsonic velocity will be observed. As deflagration is an expansion wave, the pressure drops in the reaction zone and the combustion products accelerate away in the direction that is opposite to the deflagration wave propagation.

A detonation wave can be initiated in a long tube with one of its ends closed. If the fuel-oxidizer mixture is ignited near the closed end, a self-propagating detonation wave will start traveling towards the open end. In general, the initiation of a detonation wave is not immediately achieved after ignition. In the presence of a strong ignition source near the closed end, a detonation wave can be initiated. In such a case, burned products will expand behind a wave traveling inside the tube. The expansion wave generates disturbances that coalesce and form fast traveling compression waves. These compression waves are sustained by rapid heat release and form a detonation wave. This type of detonation wave initiation is known as deflagration–to–detonation transition (DDT). The transition from deflagration to detonation can be facilitated using devices such as Shchelkin spiral, grooves, etc. Another method to instantly form a detonation wave is to introduce a shock wave or a detonation wave from a secondary device and transmit it to the reactant mixture. This method is known as a shock- or detonation-induced detonation.

As the detonation wave is supersonic in nature and propagates at speeds on the order of thousands of meters per second, the reactants ahead of the detonation wave are not affected prior to the arrival of the wave and maintain their initial state. As the reacting shock wave propagates, the reactants are compressed, heated and ignited. This results in a propagating shock with a combustion zone attached to the shock. The combined shock wave and combustion zone can be considered as a single discontinuity surface acting as the boundary between the burned and unburned gases. This discontinuity surface is known as the detonation wave. While deflagration is the common type of combustion that propagates with a velocity of less than $O(10\text{ m/s})$, detonations propagate at supersonic velocities and are a rare class of combustion. Table 1.1 shows the qualitative differences between detonations and deflagrations.

Table 1.1: Qualitative difference between detonations and deflagrations in gases [6]

Parameter	Detonation	Deflagration
u_1/c_1	5-10	0.0001-0.03
u_2/u_1	0.4-0.7	4-16
p_2/p_1	13-55	0.98-0.976
T_2/T_1	8-21	4-16
ρ_2/ρ_1	1.4-2.6	0.06-0.25

Subscripts 1 and 2 for the properties represent the initial state of the reactants and final state of the products respectively. In Table 1.1, u is the velocity of the wave, c is the speed of sound, p is the pressure, T is the temperature and ρ is the density.

1.2.2 Thermodynamics of Detonation

Detonations were first scientifically studied in the late 19th century by Berthelot, Vieille and Le Chatelier [15, 16]. There are two well-known theories that are currently used to describe detonations. The first one is known as *Chapman–Jouguet* (CJ) theory, which was proposed separately by Chapman [17] and Jouguet [18]. The second theory was proposed in the early 1940s and was the result of individual works by Zel'dovich [19], von Neumann [20] and Doering [21]. The theory is thus known as the *Zel'dovich–von Neumann–Doering* (ZND) theory that describes a shock wave sustained and driven by heat addition. A brief discussion of detonation waves using CJ theory is presented in this section to help understand the dynamics of detonation and to understand the potential use of detonation waves in applications such as thrust generation. Figure 1.1 shows a schematic of a steadily propagating, one-dimensional combustion wave. The subscripts 1 and 2 for the parameters represent the initial state of the reactants and final state of the products respectively.

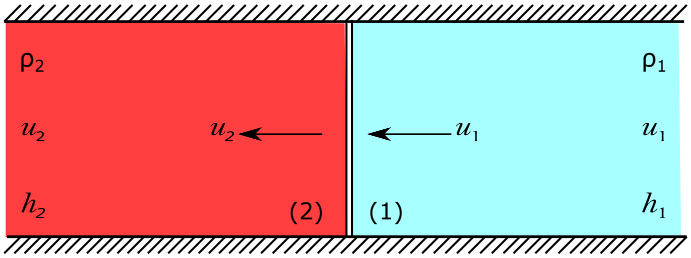

Figure 1.1: Chapman-Jouguet detonation wave schematic.

The conservation of mass, momentum and energy equations, along with the equation of state for one-dimensional combustion wave shown in Fig. 1.1 are given by

$$\rho_1 u_1 = \rho_2 u_2 \tag{1.1}$$

$$p_1 + \rho_1 u_1^2 = p_2 + \rho_2 u_2^2 \tag{1.2}$$

$$c_{p,1} T_1 + \frac{1}{2} u_1^2 + q = c_{p,2} T_2 + \frac{1}{2} u_2^2 \tag{1.3}$$

$$p_1 = \rho_1 R_1 T_1 \tag{1.4}$$

$$p_2 = \rho_2 R_2 T_2 \tag{1.5}$$

It is assumed that all combustion events have coalesced into a discontinuity. The initial condition of the gas is assumed to be known and q in Eq. 1.3 represents the heat added due to the release of chemical energy. The unknown properties u_1, u_2, ρ_2, p_2 and T_2 can be obtained using the equations given above.

The total enthalpy, which constitutes both the sensible and chemical enthalpies, is defined as $h = c_p T + h^0$ with h^0 being the specific heat of formation in the standard state. The heat added via energy release in the energy equation can be given by $q = h_1^0 - h_2^0$. Using the conservation of mass equation, Eq. 1.1, the expression for u_2 can be substituted into the momentum equation, Eq. 1.2, and expression for u_1 as a function of pressure and density can be derived as

$$u_1^2 = \frac{1}{\rho_1^2}\left[(p_2 - p_1)\Big/\left(\frac{1}{\rho_1} - \frac{1}{\rho_2}\right)\right] \tag{1.6}$$

In a similar manner, Eq. 1.6 can be substituted back into the mass conservation equation to obtain

$$u_2^2 = \frac{1}{\rho_2^2}\left[(p_2 - p_1)\Big/\left(\frac{1}{\rho_1} - \frac{1}{\rho_2}\right)\right] \tag{1.7}$$

Subtracting Eq. 1.7 from Eq. 1.6 yields

$$u_1^2 - u_2^2 = \left[(p_2 - p_1)\left(\frac{1}{\rho_1} + \frac{1}{\rho_2}\right)\right] \tag{1.8}$$

Similarly, Eq. 1.8 can be substituted into the energy equation to yield

$$c_{p,2}T_2 - c_{p,1}T_1 = q + \frac{1}{2}\left[(p_2 - p_1)\left(\frac{1}{\rho_1} + \frac{1}{\rho_2}\right)\right] \tag{1.9}$$

Lastly, substituting back into Eq. 1.3 results in

$$q = \frac{\gamma}{\gamma - 1}\left(\frac{p_2}{\rho_2} - \frac{p_1}{\rho_1}\right) - \frac{1}{2}\left[(p_2 - p_1)\left(\frac{1}{\rho_1} + \frac{1}{\rho_2}\right)\right] \tag{1.10}$$

Equation 1.10 is valid for a shock wave when $q = 0$. Equations 1.8 and 1.10 can be used to obtain the inert Hugoniots for an inert gas with constant specific heat. Similarly, Equations 1.8 and 1.9 can be solved iteratively to determine all the possible combinations of pressure and specific volume for a valid Hugoniot curve as shown in Fig. 1.2. For a reactive mixture, two curves can be obtained representing states of before and after heat release.

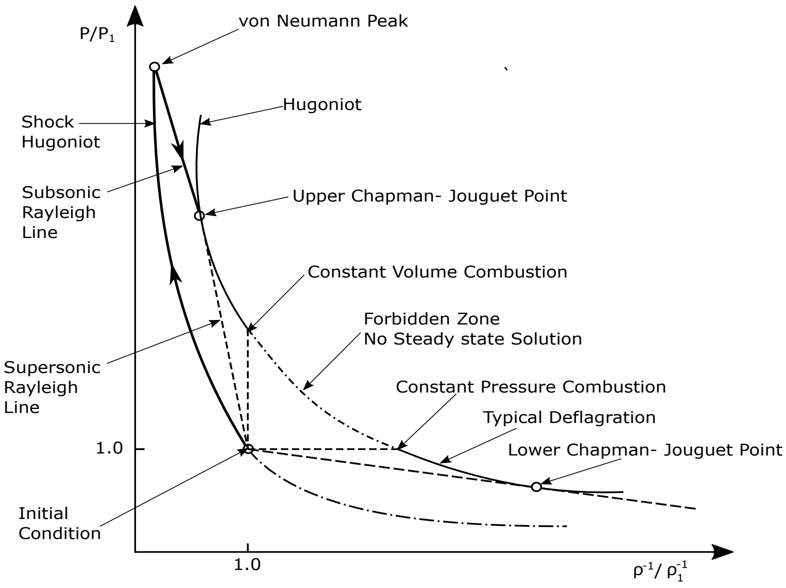

Figure 1.2: Hugoniot curve, adapted from [1].

Figure 1.3 shows the real gas Hugoniot curve for a stoichiometric H_2–air mixture. α is the shape factor and can be defined as

$$\tan\alpha = \frac{p_2 - p_1}{1/\rho_1 - 1/\rho_2} \tag{1.11}$$

The shock Hugoniot curve represents a series of solutions for shock and expansion waves without combustion under the adiabatic flow assumption. When combustion takes place, the heat addition due to combustion effectively pushes the Hugoniot curve to the right, and the attainable points on the detonation Hugoniot must be found with respect to the initial state of the mixture. From Fig. 1.3, the two tangency points created through α are known as upper CJ and lower CJ points. The upper CJ point is a high-speed compression wave, and the lower point is a low-speed expansion wave. Chapman showed that the upper point corresponds to a condition for $P_2 > P_1$ and $\rho_2 > \rho_1$ and represents a detonation. On the other hand, the lower point corresponds to a deflagration wave.

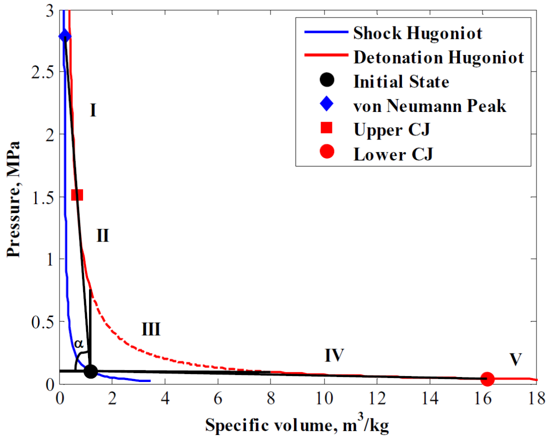

Figure 1.3: Hugoniot curve for stoichiometric H_2–air combustion [2].

The horizontal, vertical and tangent lines from the initial condition point divide the Hugoniot curve into five regions, as shown by Roman numerals I-V in Fig. 1.3. Region I corresponds to a strong detonation. The gas velocity before the detonation wave is supersonic, while the velocity is subsonic after the wave. Region II is the weak detonation zone with the gas velocities being supersonic both before and after the wave. In region III, the wave velocity calculated using the governing equations results in a negative velocity, which is not a feasible solution. This is shown with a dashed line. In region IV, the gas flow stays subsonic before and after the wave and this corresponds to a weak deflagration. The solution in region V predicts an increasing gas velocity from subsonic to supersonic regime indicating a strong deflagration. This condition is physically impossible. The von Neumann peak represents the state of the gas which has been compressed using a shock wave and heat addition has taken place. A stable detonation is possible only when the final conditions of the products correspond to the upper CJ point. This implies that the velocity of the wave is equal to the speed of the combustion products plus their mass velocity resulting in a self-sustained detonation wave. The dashed blue and red lines in Fig. 1.4 show inert Hugoniot and the detonation Hugoniot respectively. The corresponding von Neumann peak and upper CJ point for this case are also shown. The ideal pulse detonation engine cycle is shown using the solid blue line. In the cycle, the path between points 0 and 3 represents compression via a shock. Heat addition due to chemical energy released from combustion takes place during the path between points 3 and 4. Path 4 to 10 represents the isentropic expansion which is followed by path 10 to 0 representing heat rejection. The area enclosed by the PDE cycle in the $p - v$ diagram represents the work output of the engine and the area enclosed in the $T - s$ diagram represents the heat release of the engine.

Having discussed the concept of detonation, the next step in understanding the

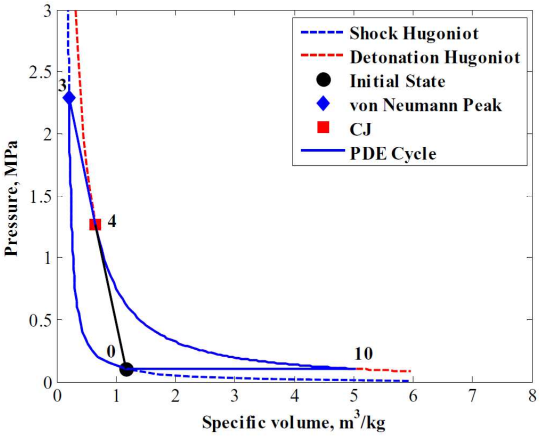

Figure 1.4: A $p-v$ diagram of a pulse detonation engine operating with a hydrogen-air mixture [2].

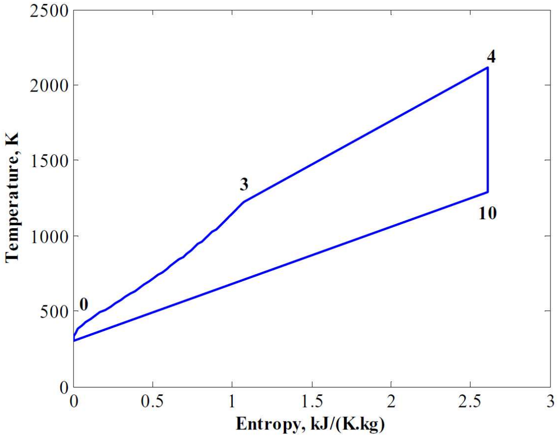

Figure 1.5: A $T - s$ diagram of the pulse detonation engine cycle [2].

process would be to understand the ideal properties of detonation waves at the upper CJ state for a variety of conditions. Recall from the solution of the Hugoniot equation that the gas moves with a compression wave. Since the reactants at the closed end of the tube must be stationary, the gas in the tube must be decelerating from the detonation front to the wall in a rarefaction wave. This rarefaction wave is known as Taylor expansion wave [22]. Endo and Fujiwara incorporated these properties to develop a model for the performance of an ideal pulse detonation engine [4].

The variation of the detonation properties as a function of the equivalence ratio exhibit interesting trends. Figures 1.6 and 1.7 show that the CJ state does not correspond to the maximum pressure and temperature ratios. Figures 1.8 and 1.9 also show that fuel-rich mixtures generally have higher property ratios as compared to the CJ states.

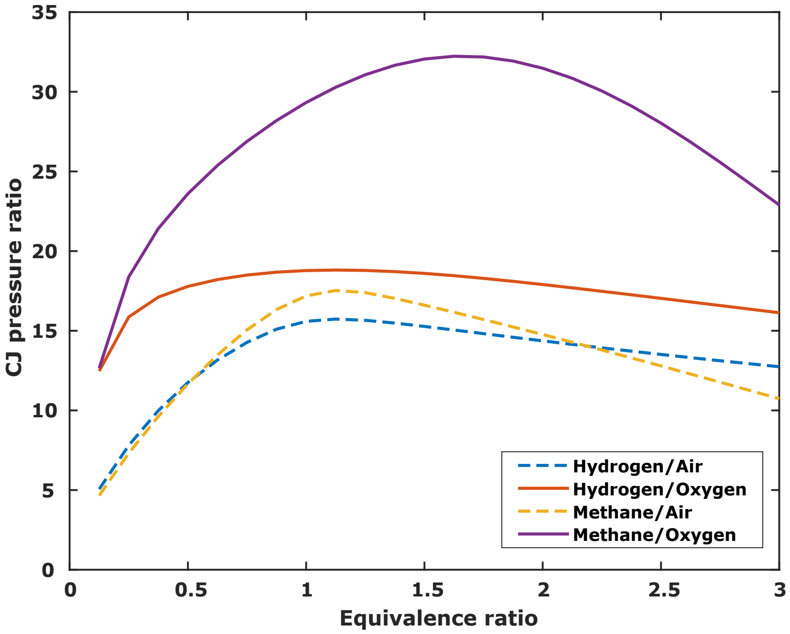

Figure 1.6: Variation of Chapman–Jouguet pressure ratio as a function of equivalence ratio for initial $T = 298$ K and $p = 1$ bar.

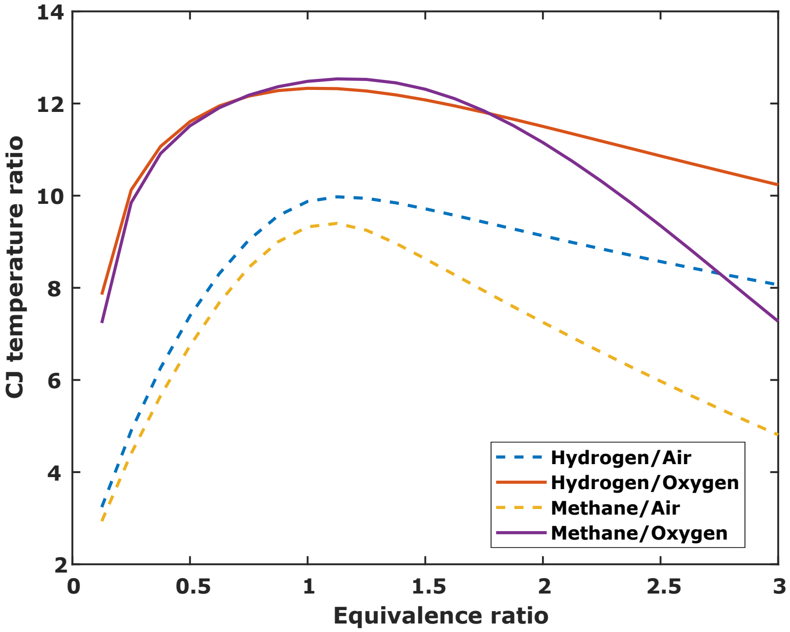

Figure 1.7: Variation of Chapman–Jouguet temperature ratio as a function of equivalence ratio for initial $T = 298$ K and $p = 1$ bar.

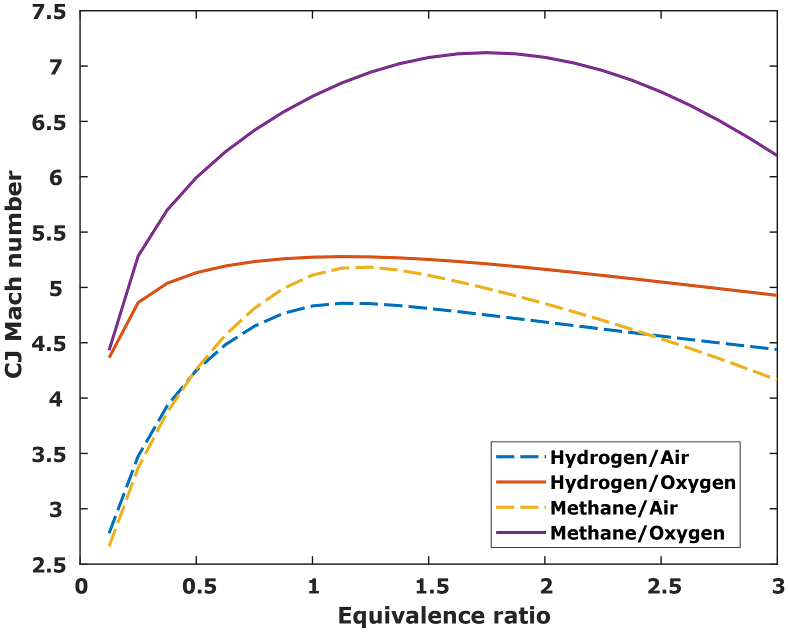

Figure 1.8: Variation of Chapman–Jouguet Mach number as a function of equivalence ratio for initial $T = 298$ K and $p = 1$ bar.

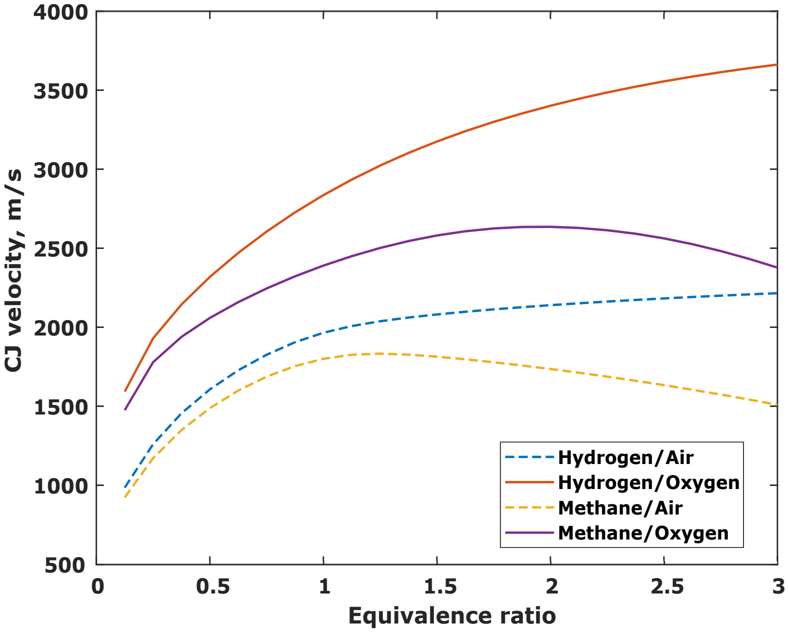

Figure 1.9: Variation of Chapman–Jouguet velocity ratio as a function of equivalence ratio for initial $T = 298$ K and $p = 1$ bar.

The plots above show that the detonation wave properties change in a smooth and continuous manner based on the initial conditions. However, achieving these results is not an easy task in practice. The theoretical results for CJ pressure and velocity for a given initial reactant mixture may not always match experimental results under certain conditions [13]. For the purpose of the current study, it is assumed that a detonation wave is achieved and operates under ideal conditions such that theoretical and experimental results match. In order to get any useful work from detonation waves, a well designed, stable and reliable detonation engine is required. Any analytical study using the thrust of a PDE would also require a good theoretical model and experimental method to accurately measure the unsteady thrust generated by a PDE [2]. In the following chapter, a brief discussion on the operation of a PDE is provided and the governing equations for an ideal cycle of PDE given by the Endo–Fujiwara model [4] are discussed.

CHAPTER 2

Building Blocks of a Linear Power Generation System

2.1 Power Generation Using Reciprocating Devices

The possibility of generating electrical power using reciprocating devices has been studied for almost 100 years now. Researchers and inventors have proposed various configurations of reciprocating devices to harvest electrical power from a variety of sources. The earliest patents for such devices were awarded beginning in the early 1920s and used internal combustion engines to drive the generators (Figs. 2.1 and 2.2). Over the years, the designs and the power sources for reciprocating devices have seen major evolution. In addition to internal combustion engines, energy sources like wave energy, human motion, and detonation engines have been proposed. The detailed design features of the linear generator vary and need to be optimized based on the application and available energy that can be harvested.

This research focuses on utilizing detonations for power generation. The previous chapter introduced the concept of detonation and distinguished clearly the differences between the common combustion phenomena of deflagration and the rare type of combustion called detonation. The current chapter introduces a device known as a pulse detonation engine (PDE) which uses detonation waves for propulsion and power generation applications. A detailed description of the linear power generator is also provided. Later, two possible configurations of a system that couples a PDE and linear generator are presented.

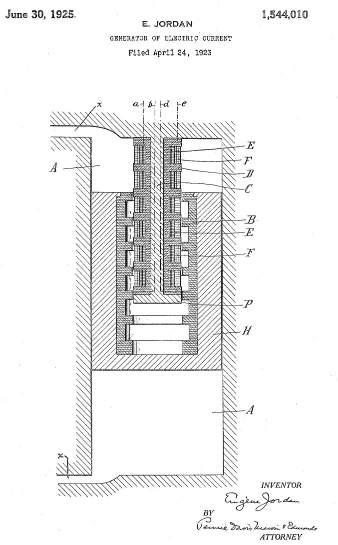

Figure 2.1: Linear generator patent by Jordon (1923).

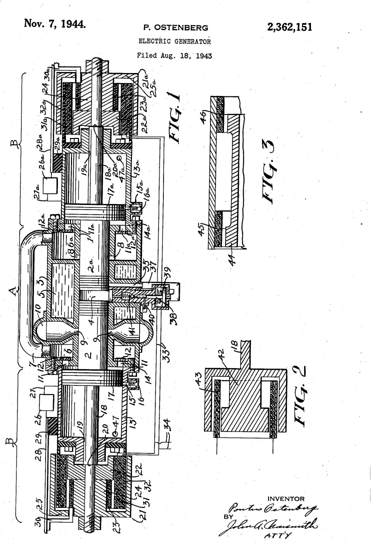

Figure 2.2: Linear generator patent by Pontus (1943).

2.2 Pulse Detonation Engine

The pulse detonation engine (PDE) is a device that uses intermittent detonations to generate thrust. The feasibility of using detonations for propulsion has been explored for the past 50 years. Unlike existing rocket and airbreathing engines that use the constant pressure, deflagrative mode of combustion, the PDE uses the pressure gain mode of combustion called detonation. The use of detonation waves reduces or eliminates the need for any mechanical compression and the associated turbomachinery. Additionally, the use of detonation minimizes the entropy gain during the heat addition process, which leads to a higher theoretical thermal efficiency as compared to conventional engines. These advantages make PDEs attractive for use in propulsion and power generation applications. In general, a simple PDE configuration consists of a straight, constant area tube that acts as the thrust chamber. The tube is closed at the head end, and open at the other. The head end houses a series of fuel and oxidizer injection ports and an ignition source for providing the required energy to achieve a weak deflagration.

2.2.1 PDE Operating Cycle

Figure 2.3 shows a schematic of a typical PDE system and corresponding details of the operating cycle. The PDE cycle usually consists of several phases, which typically include propellant fill, ignition, gas dynamic blowdown, and purge.

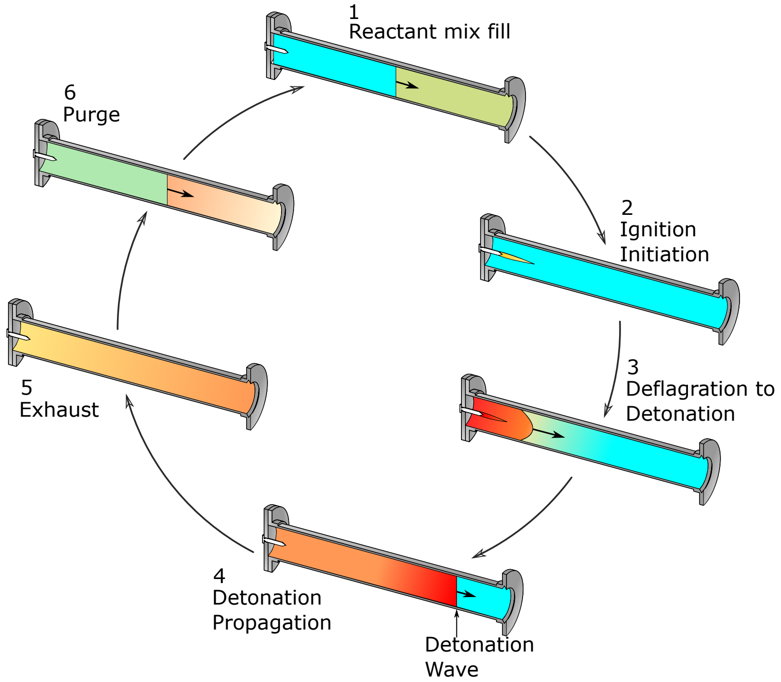

Figure 2.3: Typical pulse detonation engine operation cycle, adapted from [3].

During phase 1, the tube, initially at ambient conditions, is filled with a reactive gaseous mixture. In phase 2, as the reactants approach the open end of the tube, the igniter is activated from the closed end and a weak deflagration wave is initiated. The deflagration wave rapidly accelerates away from the closed end until abruptly transitioning into a self-propagating detonation wave, which accounts for phase 3 of the PDE cycle. In phase 4, the detonation wave propagates through the remaining length of the PDE thrust chamber while converting all the reactants into burned products. Once the detonation wave exits the chamber, an expansion wave travels back into the thrust chamber from the open end towards the closed end. The expansion wave reduces the pressure in the thrust chamber to ambient conditions and concludes phase 5. The last phase of operation consists of purging any remaining burned products at elevated temperatures from the thrust chamber with a colder inert purge gas so that refilling with a fresh reactive mixture can begin. Consequently, the PDE is an unsteady thrust producing propulsion system and the cyclic operation of a PDE requires consideration of length and time scales [23].

2.2.2 Endo–Fujiwara Model of Ideal PDE Cycle

The cycle of an ideal PDE was analyzed by Endo and Fujiwara [4]. The model assumes that the detonation wave is initiated at the closed end of the tube and propagates to the open end. When the wave reaches the open end, a rarefaction wave starts to propagate from the open end to the closed end, known as the thrust wall. The period $0 \leq t \leq t_{pl}$ in Fig. 2.4 corresponds to the combustion phase. The entire detonation process takes place during this time and the detonation wave reaches the open end of the tube at t_{pl}. At this time, a rarefaction wave starts to propagate into the tube from the open end towards the closed end. Through this rarefaction wave, the burned gases are exhausted from the tube and decay in pressure is observed. The exhaust process lasts until $t = t_{ex}$. After this time, the tube is refilled with a fresh detonable mixture. At $t = t_{cy}$, the refill process is complete and a new detonation wave is initiated.

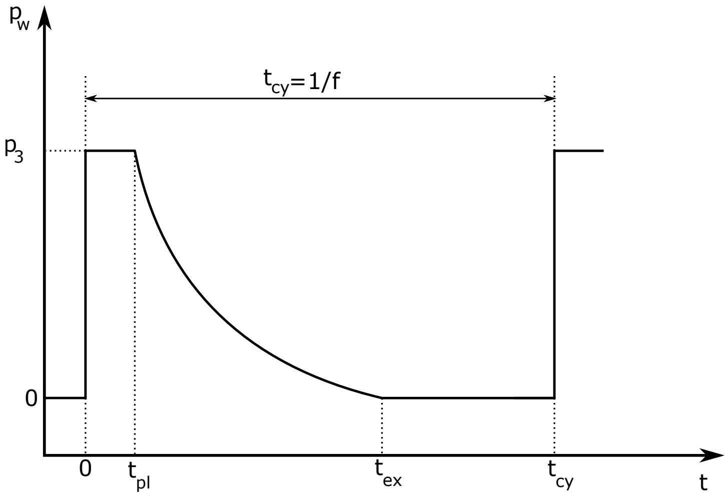

Figure 2.4: Thrust history of pulse detonation engine by Endo-Fujiwara model [4].

The analytical model starts with the introduction of some PDE parameters that are dependent on specific heat ratios and are given by

$$k_I = \frac{\gamma_2 + 1}{2\gamma_2} \tag{2.1a}$$

$$k_{II} = \frac{\gamma_2 - 1}{2\gamma_2} \tag{2.1b}$$

$$k_{III} = \frac{k_I}{k_{II}} = \frac{\gamma_2 + 1}{\gamma_2 - 1} \tag{2.1c}$$

$$k_{IV} = \frac{2[(\gamma_2 k_1)^{k_{III}} - 1]}{\gamma_2 k_{II}} \tag{2.1d}$$

$$k_V = 2{k_I}^{-k_{III}/2} \tag{2.1e}$$

The time for the detonation wave to reach the CJ state is given by

$$t_{cj} = \frac{L}{D_{cj}} \tag{2.2}$$

where D_{cj} is the Chapman–Jouguet detonation speed. The time at which the pressure plateau ends and the expansion wave initiates a pressure decay is given by

$$t_{pl} = k_V t_{cj} \tag{2.3}$$

Using the above equations, a new set of parameters was introduced by Endo and Fujiwara, which are given by

$$K_I = k_{IV}\left[\left(\frac{\gamma_1}{2\gamma_2}\right)^{k_{II}} k_I^{k_I} M_{cj}^{2k_{II}} - 1\right] + k_V \tag{2.4a}$$

$$K_{II} = k_V + \frac{k_{IV}}{k_{III}}\left[1 - \left(\frac{K_1 - k_V}{k_{IV}} + 1\right)^{-k_{III}}\right] \tag{2.4b}$$

$$K_{III} = \frac{K_{II}\left(\dfrac{K_I - k_V}{k_{IV}} + 1\right)^{1/k_{II}} - K_I}{\left(\dfrac{K_I - k_V}{k_{IV}} + 1\right)^{1/k_{II}} - 1} \tag{2.4c}$$

$$K_{IV} = \frac{K_{III}}{\gamma_1 M_{cj}^2}\left[\left(\frac{K_I - k_V}{k_{IV}} + 1\right)^{1/k_{II}} - 1\right] \tag{2.4d}$$

The time at which the pressure at the thrust wall is the same as the initial pressure is known as the exhaust time and can be determined by

$$t_{ex} = t_{cj} K_I \tag{2.5}$$

Endo and Fujiwara obtained a functional form of the thrust–density history, showing a plateau followed by decay as given by

$$p_w = \begin{cases} p_3 & \text{if} \quad 0 \le t \le t_{pl} \\ p_3 \left[\dfrac{k_{IV}\ t_{cj}}{(t - t_{pl}) + k_{IV}\ t_{cj}} \right]^{-k_{II}} & \text{if} \quad t_{pl} \le t \le t_{ex} \end{cases} \tag{2.6}$$

In the above equation,

$$p_3 = \frac{\gamma_1}{\gamma_2} k_I^{k_{III}/2} M_{cj}^2 p_1 \tag{2.7}$$

The thrust generated by the PDE is used to drive the LPG to convert the chemical energy of the fuel–oxidizer mixture to electricity. The parameters such as D_{cj} can be calculated for a given reactant mixture and initial conditions using NASA CEA applet [24].

2.3 Linear Power Generator

A linear generator is an electromagnetic device that converts the mechanical energy of linear reciprocating motion to electrical energy. Topologically, linear generators are equivalent to the 'unfolded' version of their rotary counterparts. Since linear generators come in a variety of designs, many different methods of classifying linear generators exist in literature [25, 26]. Figure 2.5 shows the classification of linear generators based on the mode of excitation. The first type of linear generator uses electrostatic properties to move the translator of the generator. The second type uses the electromagnetic behavior of reciprocating machines to generate power. The last two types use piezoelectric and magnetostrictive properties to interact with a mover. The piezoelectric generator works under an electric field and is typically used in smaller devices. Also, the stroke length for both the piezoelectric and magnetostrictive generators are smaller compared to electrostatic and electromagnetic generators.

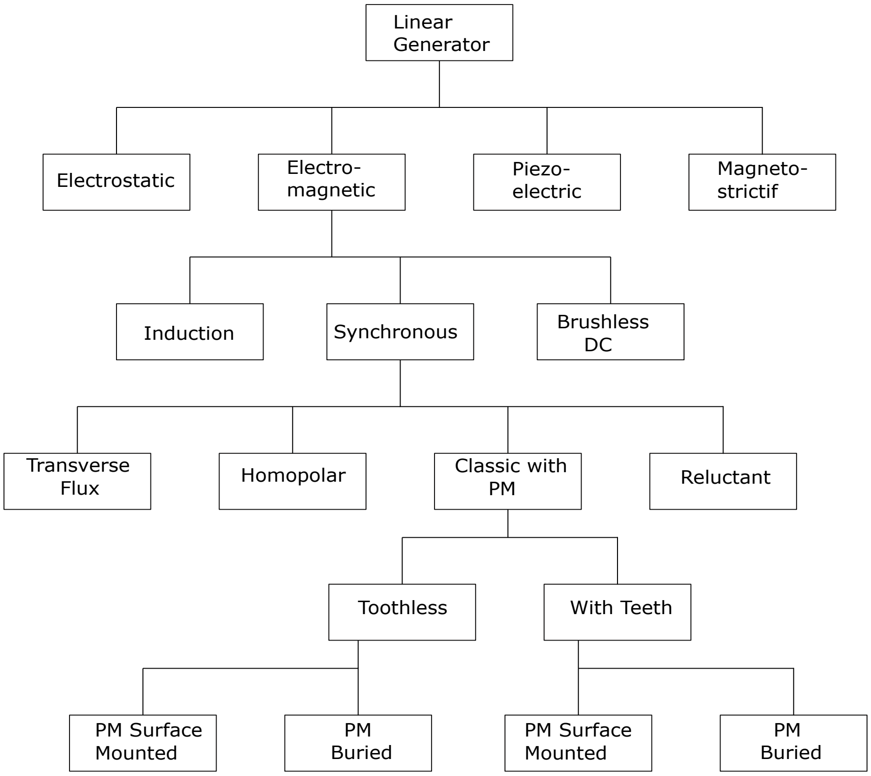

Figure 2.5: Classification of linear generators based on mode of excitation.

Electromagnetic linear generators can further be divided into three main classes, namely, induction generators, synchronous generators, and DC generators. The excitation in synchronous and DC generators is produced using magnets, while induction generators have a self-induced excitation mode. The most commonly used type of linear generator is the synchronous machine with permanent magnets.

Another method of classifying linear generators is based on construction geometry. Broadly, linear generators can be classified as flat or tubular type linear generators on the base of their geometries. Each of these types can also be designed as a single-sided or a double-sided machine.

A linear generator can also be categorized in one of the following types

(i) Moving coil type

(ii) Moving magnet type

(iii) Moving iron type

These are shown in Figs. 2.6, 2.7 and 2.8 respectively.

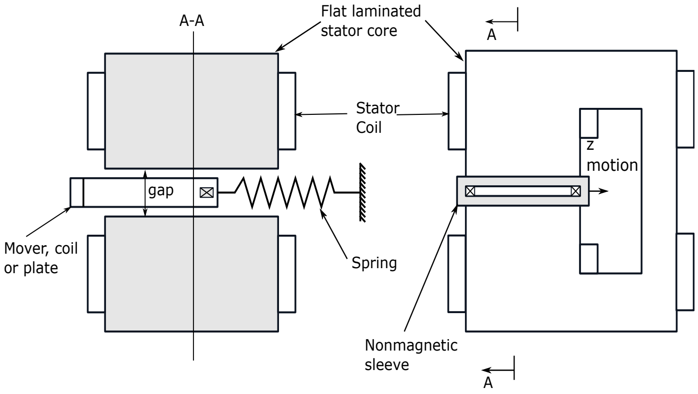

Figure 2.6: Moving coil linear generator.

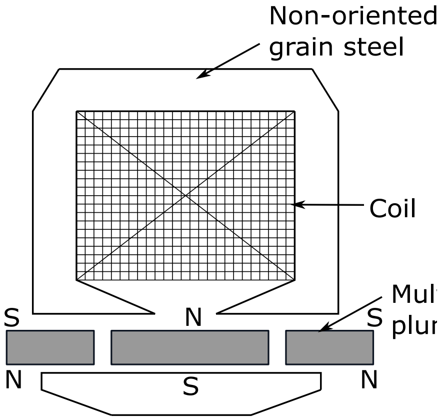

Figure 2.7: Moving magnet linear generator.

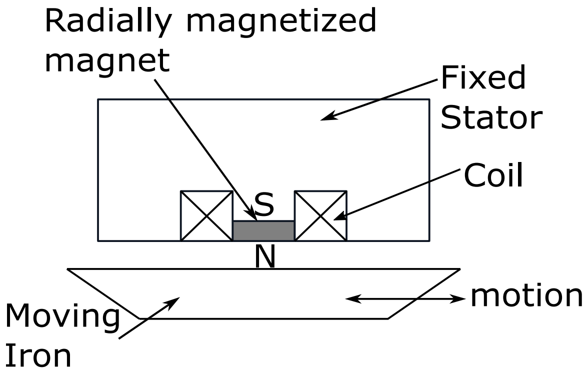

Figure 2.8: Moving iron linear generator.

Each type of linear generator mentioned above has its set of advantages and disadvantages. The moving coil generator uses flexible leads. A major drawback of this feature is that the leads tend to regularly wear out in high-power machines. This makes moving coil generators unsuitable for any significant power generation application. The moving magnet linear generators also suffer from issues such as large magnet leakage fields, continuous vibration exposure to the permanent magnets that leads to demagnetization, limitations on power conversion due to stroke length and magnet dimensions dictated by the airgap. Despite many advantages and being rugged, moving iron generators tend to be relatively heavier. Due to their practicality in the application, only moving magnet generators were studied for this research.

The manner of arrangement of permanent magnets in a linear generator can also be used as a classification criterion. The arrangement of the permanents plays a critical role in determining the excitation flux in the air gap. The magnets can be mounted on the translator or be buried in the translator or combined to form a Halbach array. These three families of permanent magnet arrangements are shown in Fig. 2.9. All three of these arrangements can also be used in a double-sided arrangement as shown in Fig. 2.9(b), (d), (f) and Fig. 2.10 and 2.11.

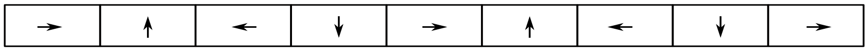

(a) Single sided Halbach array

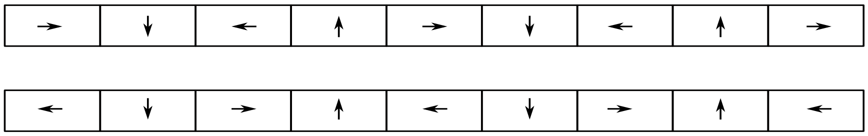

(b) Double sided Halbach array

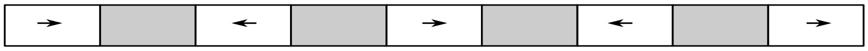

(c) Single sided buried magnets

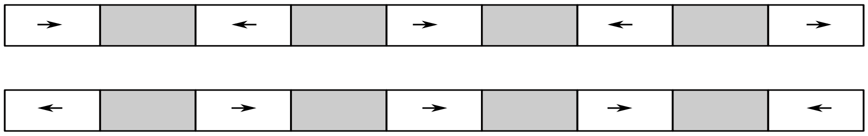

(d) Double sided buried magnets

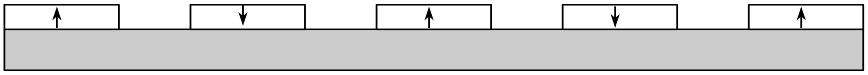

(e) Single sided surface mounted magnets

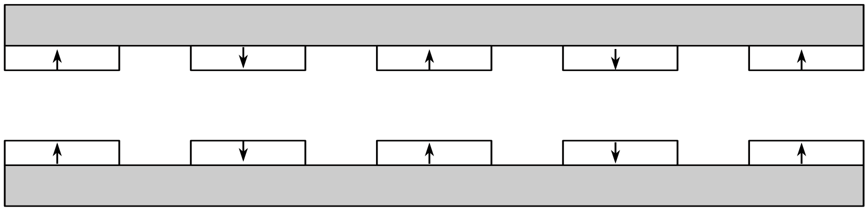

(f) Double sided surface mounted magnets

Figure 2.9: Various arrangements of permanent magnets in a linear generator.

Typically, the buried magnet topology, as shown in Fig. 2.9(c), consists of a longitudinal magnetization path, while the surface-mounted topology gives rise to a transverse magnetization path. On the other hand, the Halbach array uses a particular arrangement of magnets that results in the magnetic flux being enhanced on one side (strong side) and canceled on the other side. The most common type of linear generator used currently is the toothed permanent magnet synchronous generator as shown in Fig. 2.12.

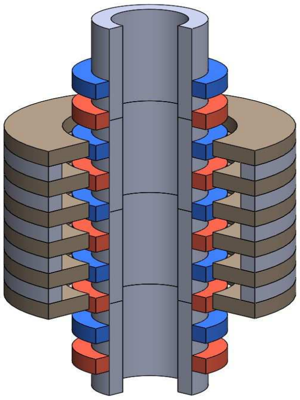

Figure 2.10: Surface mounted tubular topology.

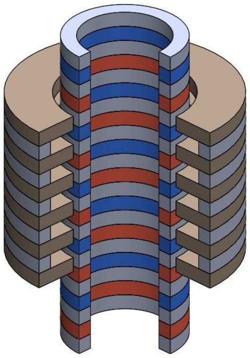

Figure 2.11: Buried magnet tubular toplogy.

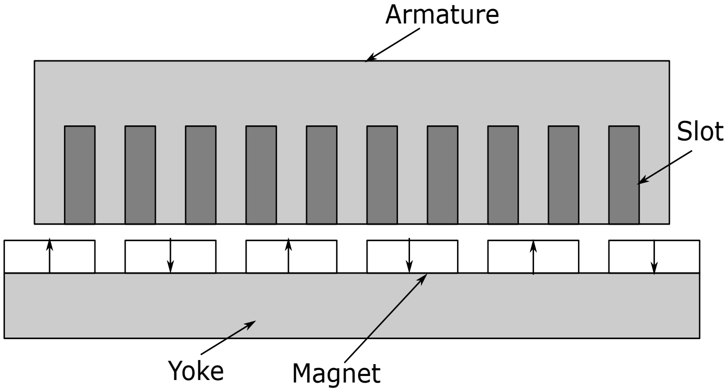

Figure 2.12: A toothed single-sided synchronous generator.

The flat type generator can be further improved by adding many sides, forming an enclosed structure. This leads to a minimization of normal force on the machine, which can be harmful to routine operations. In theory, the tubular type machine has inherently zero radial force between the stator and the translator but they can be more complex to manufacture. One reason why double-sided machines are used in the flat configuration is to reduce the normal forces between the stator and the translator. Another reason to use double-sided design is better utilization of magnetic material and space, resulting in enhanced flux linkage.

The following sections review Maxwell's theory and the magnetic properties of permanent magnets. A good understanding of these theories is critical for performing electromagnetic simulations, which can be used to determine a suitable linear generator for the current application.

2.3.1 Review of Maxwell's Theory

The well-known Maxwell's equations for electromagnetic coupling and induction form the basis of the field-based approach of modeling a generator.

$$\nabla . \boldsymbol{D} = \rho_c \tag{2.8}$$

$$\nabla . \boldsymbol{B} = 0 \tag{2.9}$$

$$\nabla \times \boldsymbol{E} = -\frac{\partial \boldsymbol{B}}{\partial t} \tag{2.10}$$

$$\nabla \times \boldsymbol{H} = \boldsymbol{j} + \frac{\partial \boldsymbol{D}}{\partial t} \tag{2.11}$$

In the above equations, $\boldsymbol{B}$ is the magnetic flux density, $\boldsymbol{D}$ refers to the displacement field, $\boldsymbol{E}$ is the electric field and $\boldsymbol{H}$ is the magnetizing field. On the right-hand side, ρ_c is the charge density and $\boldsymbol{j}$ is the free current density. To obtain a field model of a generator, a magnetic circuit is required. This magnetic circuit can originate from electromagnets or permanent magnets mounted on the translator. For rotary generators, a two-dimensional geometry is frequently chosen with a cross-section normal to the axis of rotation. An error is later introduced to model the losses in the end windings. The simulations of the generator are based on mathematical models of magnetic fields. Usually, three main simplifications are made in simulating the generator. First, the displacement field $\partial \boldsymbol{D}/\partial t$ is neglected for low frequencies of less than 100 Hz. Next, the magnetic field is solved for a two-dimensional section. The last simplification relates to the end effects of the stator windings, which are modeled as impedances in an electric circuit. Based on these simplifications, Maxwell's equations can be combined into Eq. 2.12

$$\sigma \frac{\partial A_z}{\partial t} - \nabla . \left(\frac{1}{\mu} \nabla A_z \right) = -\sigma \nabla V \tag{2.12}$$

The finite element method (FEM) can be used to solve the above equation to study the performance of the generator. Figure 2.13 shows a four-sided topology. The stator side closest to the viewer is hidden in this view for clarity. The magnets are mounted on the surface of the translator with alternating polarity. ANSYS Maxwell ® was used to study the static magnetic characteristics of the linear generator. The materials used in the simulation are typical materials used in the construction of such electrical machines.

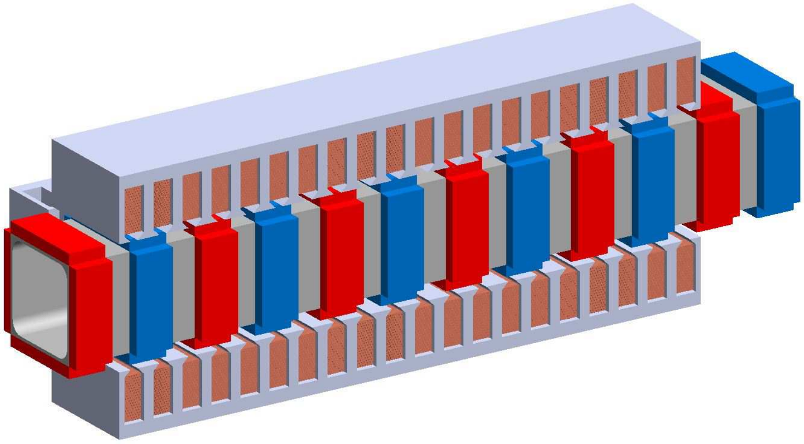

Figure 2.13: A four-sided flat type linear generator.

To finalize a linear generator topology best suited to be used with a PDE, finite element simulations of various topologies can provide crucial insights. The first step in using simulations for studying the characteristics of a particular topology is to understand the material properties. The following section introduces some of the useful properties of a hard nonlinear magnetic material known as rare earth neodymium-iron-boron magnet.

2.3.2 Rare Earth NdFeB Magnets and Their Properties

The magnetic material used for generating the magnetic field in the current study is sintered neodymium-iron-boron (NdFeB). NdFeB magnets are categorized as hard nonlinear materials. Neodymium magnets were invented in the 1980s. They are one of the strongest and most affordable rare earth magnets. NdFeB magnets are available in various grades based on the strength of the magnetic field that can be generated. Since magnetic material properties change with temperature, users of permanent magnets are often challenged to design machines that operate at acceptable levels over a wide temperature range. Understanding how these properties change is, therefore, a necessary requirement for sound design.

The relationship between magnetic flux density $\boldsymbol{B}$, magnetic field $\boldsymbol{H}$, and polarization $\boldsymbol{J}$ within magnets is given by

$$\boldsymbol{B} = \mu_0 \boldsymbol{H} + \boldsymbol{J} \tag{2.13}$$

where $\mu_0 = 4\pi \times 10^{-7}$ H/m is the magnetic permeability of vacuum. The equation shows that the magnetic flux density $\boldsymbol{B}$ within a magnetic material can be expressed as a function of magnetic field $\boldsymbol{H}$ and polarization $\boldsymbol{J}$ of the magnetic body. Since the magnetic field $\boldsymbol{H}$ is normally known, only the polarization $\boldsymbol{J}$ needs to be determined in order to calculate magnetic flux density $\boldsymbol{B}$. The magnitude of polarization $\boldsymbol{J}$ of the magnetic material varies with the magnetic field.

A plot showing this relationship is known as a $\boldsymbol{J}$–$\boldsymbol{H}$ loop and is shown in Fig. 2.14. The value of the external magnetic field-, $\boldsymbol{H}$-, applied to the material is plotted on the abscissa and the magnitude of the polarization $\boldsymbol{J}$ is plotted on the ordinate. Since the relationship between $\boldsymbol{J}$ and $\boldsymbol{H}$ depends on the path followed, the $\boldsymbol{J}$–$\boldsymbol{H}$ plot represents a hysteresis loop. When a magnetic field is applied to a permanent magnet which is in the neutral state of $\boldsymbol{J} = 0$, the polarization $\boldsymbol{J}$ increases with an increasing magnetic field. After a sufficiently large magnetic field has been applied, the material reaches a saturation point. The curve 0-*a*-*b*-*c* is called the initial magnetization curve and creating a permanent magnet from a neutral state in this manner is known as magnetizing. The magnitude of the polarization at the point c where the material is completely magnetized and cannot be magnetized any further is called the saturation magnetization J_s.

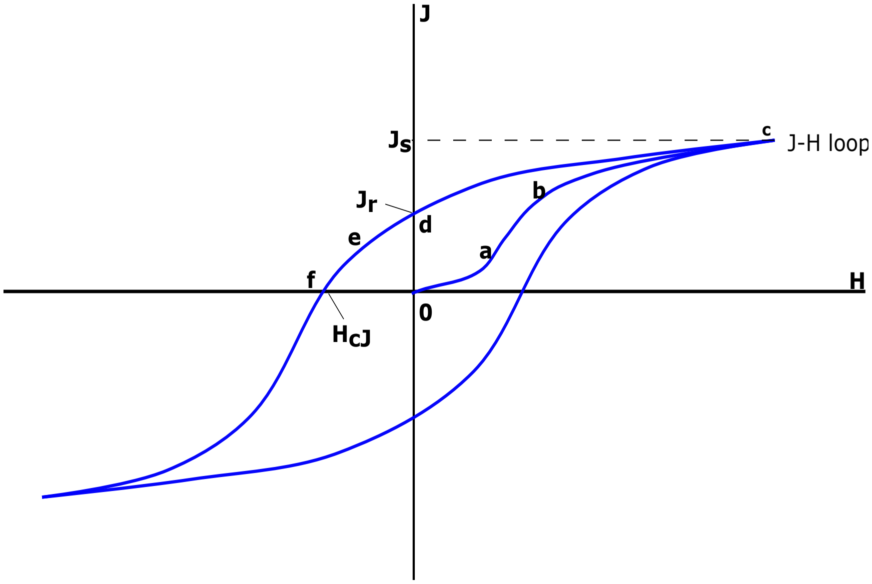

Figure 2.14: J–H loop showing magnetization and demagnetization of magnetic material.

From the saturated state, a reduction in the magnetic field will result in a new curve *c*-*d* that does not pass through the original curve as the polarization reduces gradually. The magnitude of polarization at point d when the magnetic field is zero is known as remanent magnetization J_r. If the magnetic field is further reduced, meaning, increased in the opposite direction, the magnetization does not immediately become zero. This is a feature of hard magnetic materials. When the magnetic field is further reduced, the polarization traces the curve *d*-*e*-*f*. Point *f* corresponds to a zero polarization state with a non-zero magnetic field. This magnetic field is known as coercive force H_{cJ} and the curve *d*-*e*-*f* is known as the demagnetization curve.

When evaluating the magnetic properties of a permanent magnet, the demagnetization curve ($\boldsymbol{J}$–$\boldsymbol{H}$ curve) in an adequately magnetized state is used. On the other hand, in the actual usage state for the magnetic material, in addition to the polarization $\boldsymbol{J}$, the external magnetic field $\boldsymbol{H}$ is also taken into account and sometimes, it is more appropriate to evaluate the $\boldsymbol{B}$–$\boldsymbol{H}$ curve which shows the relationship between the magnetic flux density $\boldsymbol{B}$ and the external magnetic field $\boldsymbol{H}$. Figure 2.15 shows a $\boldsymbol{J}$–$\boldsymbol{H}$ loop and a $\boldsymbol{B}$–$\boldsymbol{H}$ loop of a permanent magnet. As given by Eq. 2.13, the flux density $\boldsymbol{B}$ is the constant multiple of the magnetic field $\boldsymbol{H}$ added to the polarization $\boldsymbol{J}$. Therefore, the $\boldsymbol{B}$–$\boldsymbol{H}$ curve has a higher shoulder in the first quadrant.

In the demagnetization curve, left on the normal magnetic field H axis is positive. The value of magnetic flux density when the magnetic field is zero is known as the remanent flux density, B_r. This value is the same as the remanent polarization, J_r. The magnitude of the magnetic field for which the magnetic flux density becomes zero is called the coercive force. To distinguish the coercive force from the magnetic field H_{cJ}, the coercive force due to the magnetic flux density is labeled as H_{cB}.

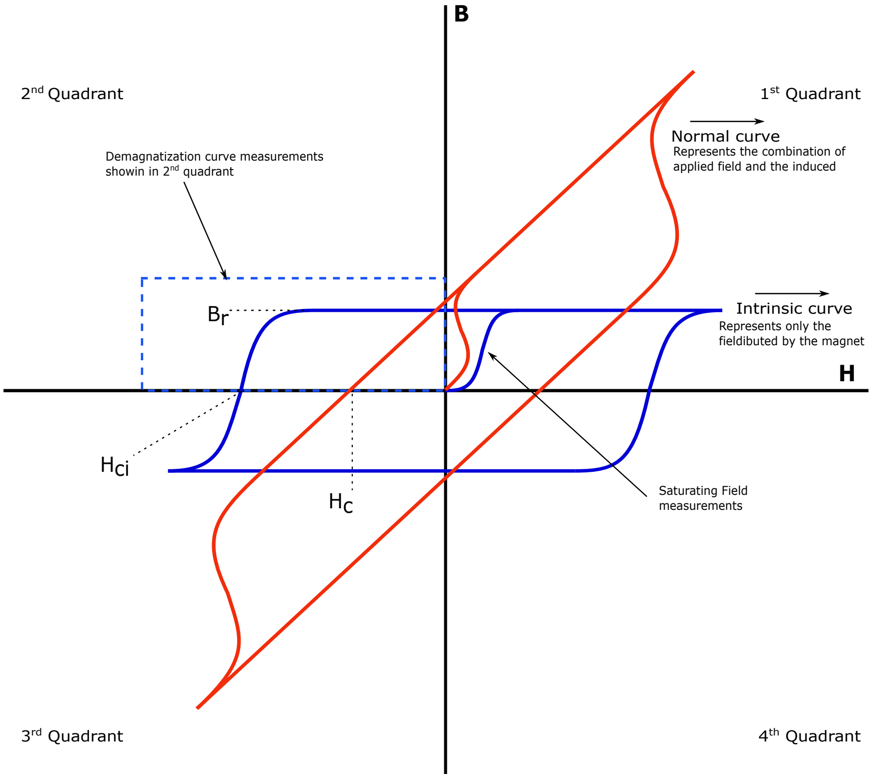

Figure 2.15: The hysteresis loop for magnetic materials.

The magnitude of energy that can be taken out from a magnet is proportional to the product of the magnetic flux density B and the magnetic field on the ***B*–*H*** curve. The maximum value of this product of the magnetic flux density and the magnetic field is called the maximum energy product $(\mathrm{BH})_{\mathrm{max}}$. A powerful magnet with a large maximum energy product has a large value of remanent flux density B_r and coercive force H_{cB} on the ***B*–*H*** curve must be large.

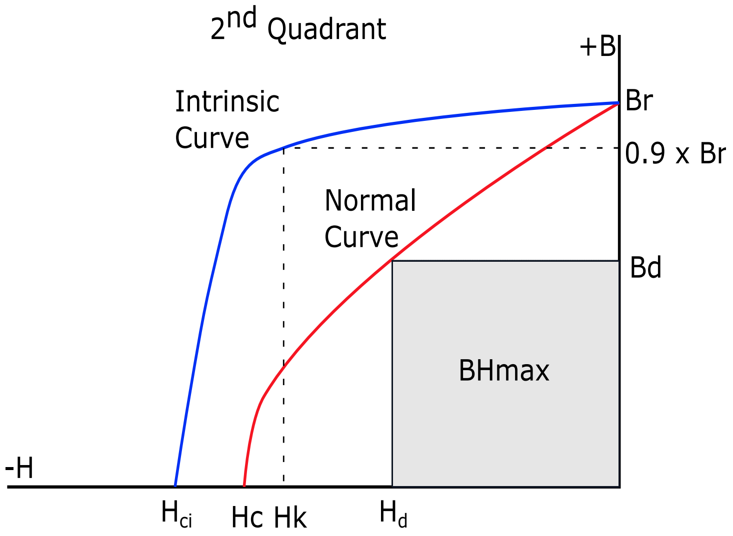

Figure 2.16: Details of second quadrant of hysteresis loop.

Figure 2.17 shows the demagnetization curve for the N52 NdFeB magnet used in the simulation of linear generator configurations for this research.

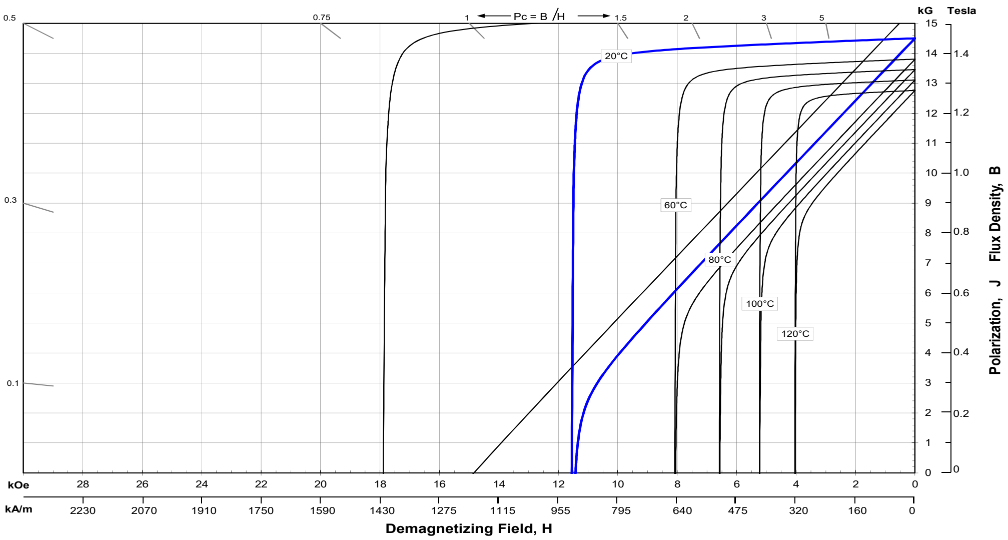

Figure 2.17: Demagnetization curve of N52 magnetic material shown in second quadrant, adapted from [5]

Table 2.1 lists the magnetic properties of the N52 magnet.

Table 2.1: Magnetic properties of N52 grade NdFeB magnet [5]

Parameter	Units	Minimum	Nominal	Maximum
Residual Induction, Br	Gauss	14,200	14,500	14,800
	T	1.42	1.45	1.48
Coercivity, Hc	Oesterd	10,500	12,300	14,100
	kA/m	836	979	1122
Intrinsic Coercivity, Hc_j	Oesterd	11,000	–	–
	kA/m	876	–	–
Maximum Energy Product, $BHmax$	MGOe	49	51	53
	kJ/m^3	390	406	422

The materials used for the construction of other parts of a linear generator are generally made of alloys containing iron and either cobalt, nickel, or silicon. These alloys are known as soft magnetic materials. The chosen material is used in the form of lamination sheets to manufacture the stator and translator for the electrical machine.

After a geometry and materials are chosen, a simulation can be carried out using one of the many commercially available software to determine the performance characteristics of the designed machine. This is the focus of the discussion of the next section.

2.3.3 Simulation Results: Static Magnetic Analysis

ANSYS ® Maxwell ™ is a commercially available software used for high-fidelity simulations for the design and analysis of electrical machines. The software includes solvers for magnetostatic and transient simulations. However, for transient simulations with reciprocating motion, the solver can only be used for a sinusoidal external excitation force. Since the PDE thrust is not sinusoidal and continuous, the software can only be used for static simulation and the results can then be used for further analysis using other techniques.

The software was used to simulate a four-sided topology, a tubular topology, and a double-sided topology. For the four-sided and tubular geometries, the mass of the permanent magnets used in the design was kept constant. The unstructured mesh in the air gap is refined to include a minimum of three elements between the permanent magnets and the Iron alloy of the stator. An adaptive unstructured mesh with tetrahedral elements was generated for all three topologies. A cross-section of the mesh created for the four-sided topology is shown in Fig. 2.18.

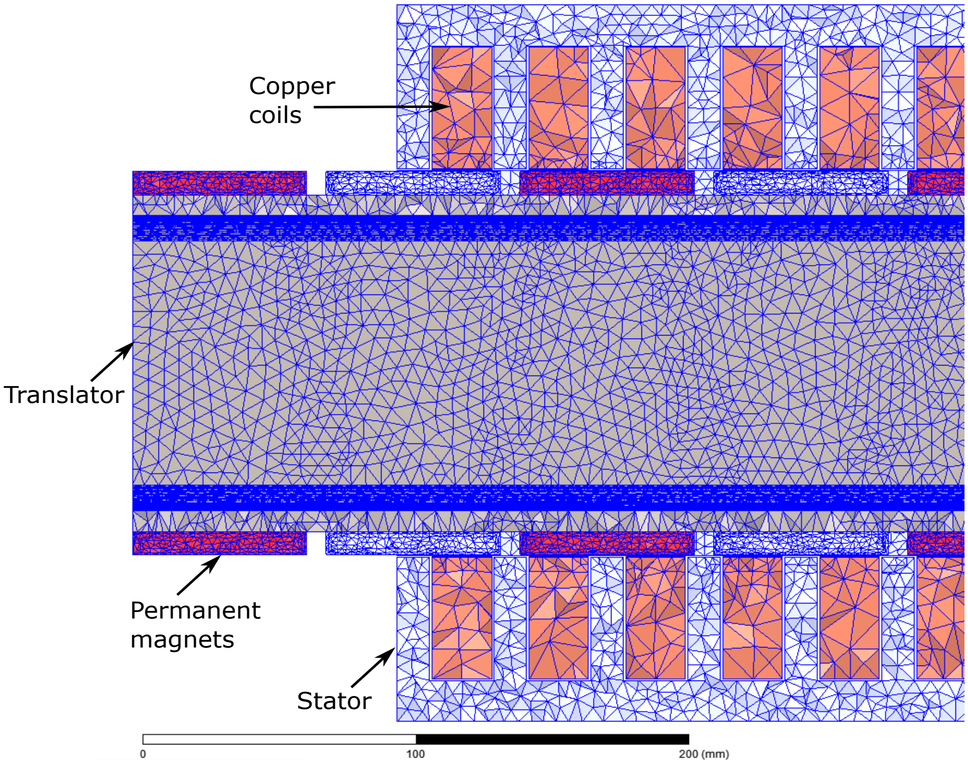

Figure 2.18: Section of four-sided generator topology showing tetrahedral mesh.

The results of the simulation showing magnetic flux density $\boldsymbol{B}$ for the four-sided linear generator are shown in Fig. 2.19 and Fig. 2.20. In order to ensure normal completion of simulation and accuracy of results, the software provides several checks. The convergence criterion for simulation was set at an energy error percentage at 1% or less. This was achieved after the second pass as the energy error dropped from 4.5% to just below one percent after two passes. Figure 2.21 shows the growth of the number of tetrahedral elements due to the adaptive meshing passes as the energy error falls below the set criterion of one percent.

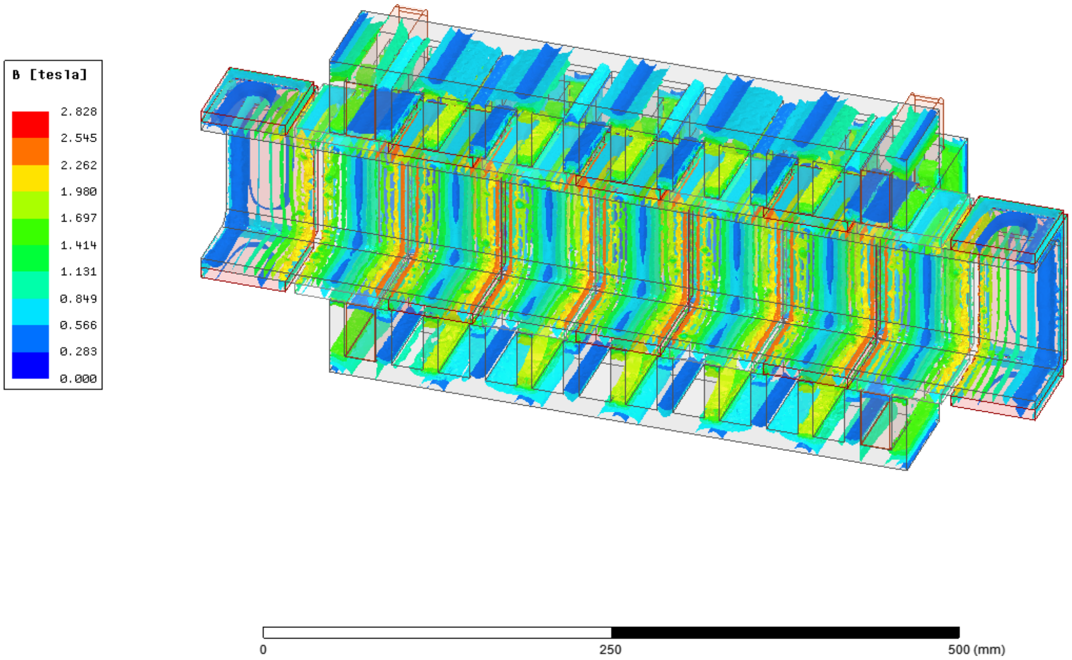

Figure 2.19: Cross-section showing magnetic flux density inside a four-sided linear generator.

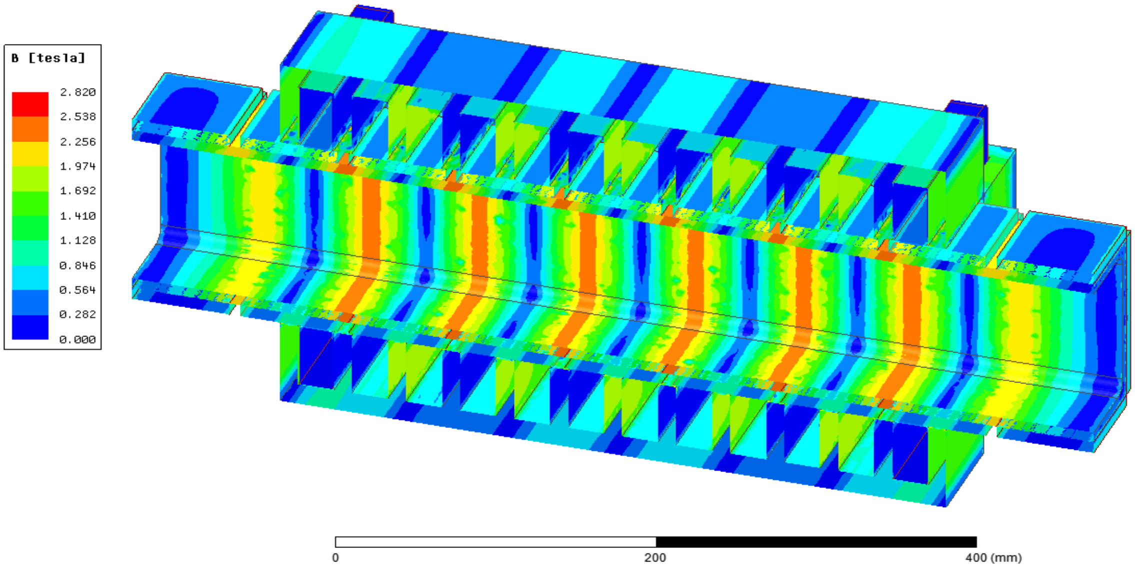

Figure 2.20: Cross-section showing magnetic flux density on the surface of a four-sided linear generator.

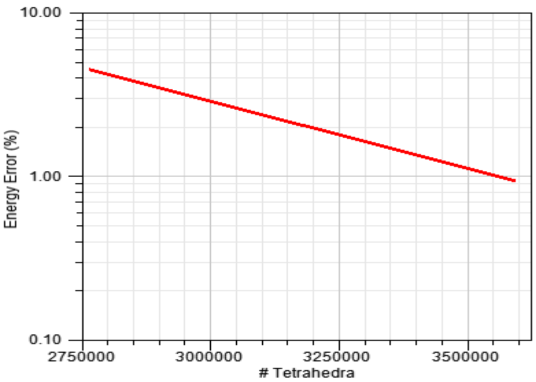

Figure 2.21: Energy error percentage vs. number of tetrahedra in four-sided topology linear generator.

The results for the static simulations for a tubular generator are shown in Fig. 2.22 and Fig. 2.23. Due to the geometry of the tubular generator, a cylindrical coordinate system was used for the simulation and ring magnets were used. As seen in Fig.

2.24, the criterion of energy error of 1% or less was satisfied with around 3 million tetrahedral elements and it was achieved with 3 adaptive mesh refinement passes.

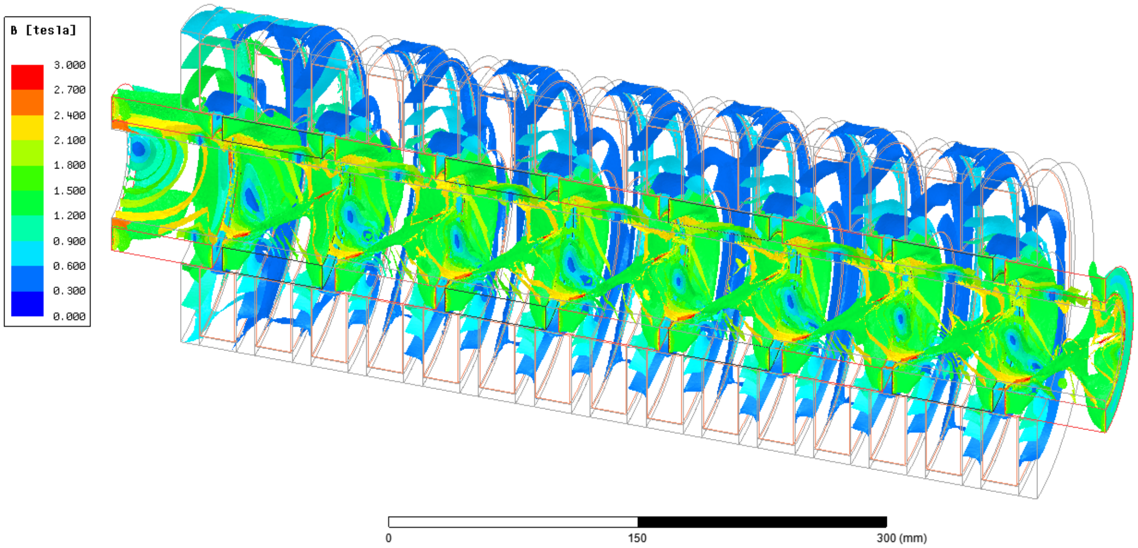

Figure 2.22: Cross-section showing magnetic flux density inside a tubular linear generator.

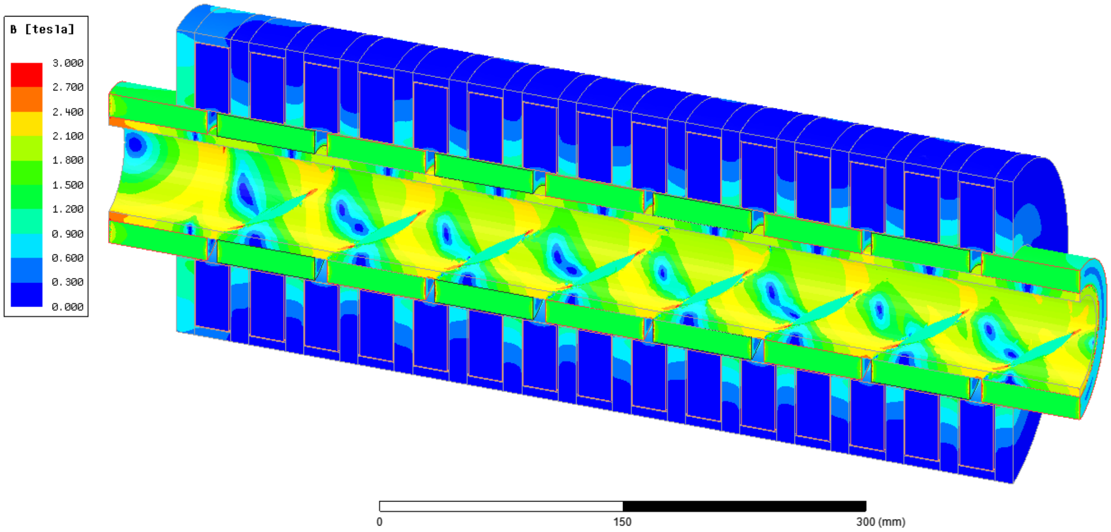

Figure 2.23: Cross-section showing magnetic flux density on the surface of a tubular linear generator.

Additional passes showed that reduction in energy error beyond 1% becomes computationally expensive. For a small improvement in the energy error criterion, the number of tetrahedra grew from approximately 3 million to about 4.4 million in one pass, as seen in Fig. 2.24.

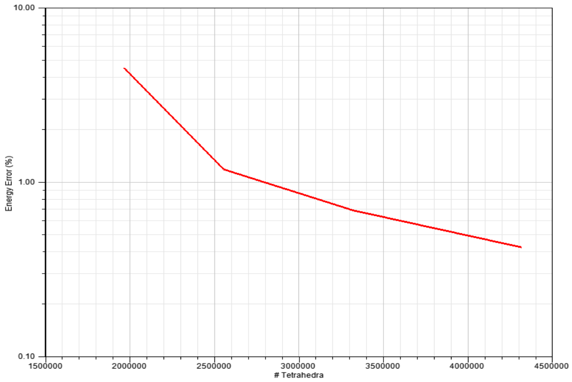

Figure 2.24: Energy error percentage vs. number of tetrahedra in tubular topology linear generator.

For both the cases, the magnetic flux density inside and on the surface are shown. The peak flux density in the four-sided generator was observed to be approximately 2.8 T while it was approximately 3 T in the tubular section. This shows that for the same mass of permanent magnets, neither of the compared geometries show any distinct advantage over the other. However, due to the ease of manufacturing of a four-sided generator over the tubular type, the four-sided generator may be preferred.

The third type of linear generator topology considered for this research is the double-sided geometry. Static finite element simulations were carried out for the double-sided geometry. The width of the double-sided and four-sided geometries was kept constant. The magnetic flux density of a double-sided generator is shown in Fig. 2.25. Computationally, the cost of the double-sided linear generator simulation was similar compared to the other two topologies as shown in Fig. **??** and Fig. 2.26. For the double-sided topology, only half of the geometry was simulated and symmetry was used. In order to avoid the influence of the edge effects, symmetry was not used in the four-sided and tubular topologies.

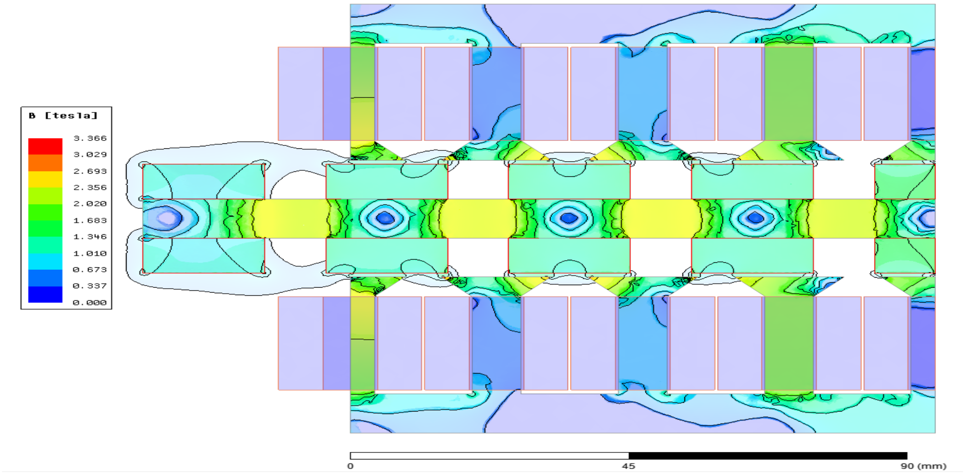

Figure 2.25: Cross-section showing magnetic flux density inside a double-sided linear generator.

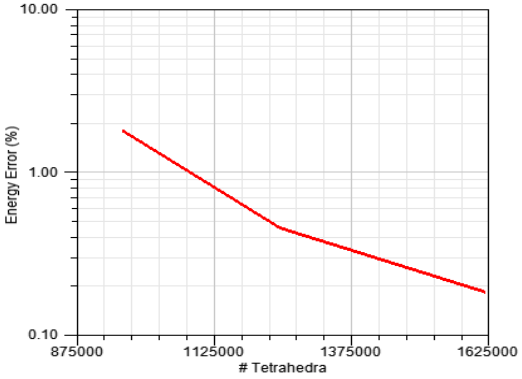

Figure 2.26: Energy error percentage vs. number of tetrahedra in double-sided topology linear generator.

2.3.4 Analytical Form of Electromagnetic Damping for Flat Double-Sided Generator

Electric power production using linear power generators has attracted significant attention in recent years. The most common application of linear generators is in converting wave energy to electricity. A literature survey to study the performance of linear generators resulted in an analytical form of the electromagnetic forces for the flat double-sided generator. As far as the author knows, analytical forms for four-sided and tubular topologies do not exist. Thorburn [27,28] provided a simplified analytical model to determine the induced EMF based on the geometry and magnetic properties of a flat double-sided linear generator. Zheng et al. [29] used the simplified model proposed by Thorburn and analyzed the electromagnetic damping of a linear generator. A brief discussion is provided below. This model will be used in the basic study to determine the electromagnetic characteristics of the generator.

Consider a linear generator with permanent magnets mounted on the translator with alternating polarity as shown in Fig. 2.27. The translator position and velocity are given by $z(t)$ and $\dot{z}(t)$ respectively.

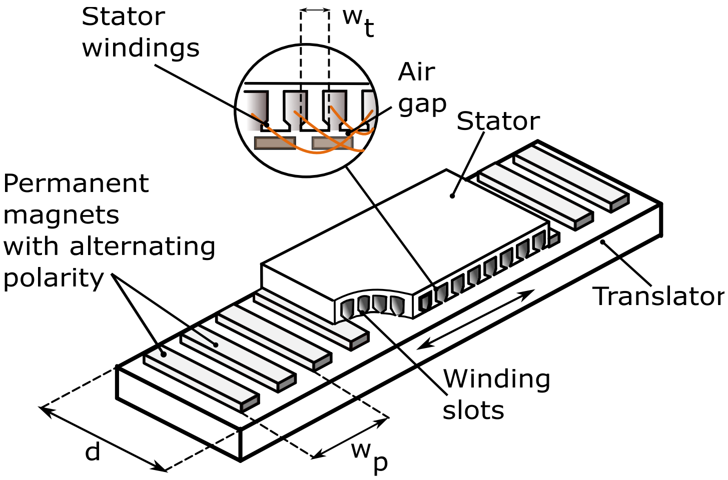

Figure 2.27: Linear power generator details.

If the pole pair width w_p is defined as the distance from one north pole to the next, then the angular frequency $\omega(t)$ is given by

$$\omega(t) = \frac{2\pi}{w_p}\dot{z}(t) \tag{2.14}$$

The electric position $\theta(t)$ is determined from $\omega(t)$ as

$$\theta(t) = \int_0^t \omega(\tau)d\tau \ = \frac{2\pi}{w_p}z(t) \tag{2.15}$$

The magnetic flux $\Psi(t)$ as a function of $\theta(t)$ is given by

$$\Psi(t) = k\cos(\theta(t) - \delta) = k\cos\left(\frac{2\pi}{w_p}z(t) - \delta\right) \tag{2.16}$$

where k is a proportionality constant and the angle δ is equal to the load angle, that is, the amount the voltage shifts during full load with respect to the no-load condition. The magnitude of the proportionality constant is given by

$$k = B_t \ w_t \ d \ n \ q \ c \tag{2.17}$$

where B_t is the magnetic field in the stator tooth, w_t is stator tooth width, d is the LPG stator side width, n is the total number of poles, q is the winding ratio and c is the number of cables in LPG stator slot. According to Faraday's law, the induced electromotive force $e(t)$ can be calculated as

$$e(t) = -\frac{d\Psi(t)}{dt} = \frac{2\pi \ B_t \ w_t \ d \ n \ q \ c}{w_p}\sin\left(\frac{2\pi}{w_p}z(t) - \delta\right)\dot{z}(t) \tag{2.18}$$

Using the equivalent circuit for a single-phase, the voltage at the terminals can be written as

$$V(t) = e(t) - RI(t) - L\frac{dI(t)}{dt} \tag{2.19}$$

where R and L are the circuit resistance and inductance respectively. The current is given by

$$I(t) = \frac{V(t)}{R_{load}} \tag{2.20}$$

where R_{load} is the external load resistance. As reported by Zheng et al. [29], we assume that the difference between $V(t)$ and $e(t)$ in this model is small and, therefore, the voltage $V(t)$ is approximated with $e(t)$ in the subsequent analysis. Therefore,

$$I(t) = \frac{e(t)}{R_{load}} \tag{2.21}$$

The output power of the linear generator is given by

$$P(t) = V(t)\ I(t) \tag{2.22}$$

According to the above equations, the magnetic force for a single-phase generator can be calculated as

$$F_{em}(t) = \frac{V(t)\ I(t)}{\dot{z}(t)\ \mu} \tag{2.23}$$

where μ is the generator efficiency. Researchers have reported a generator efficiency as high as 95%. Similarly, the total electromagnetic force for a n-phase generator can be expressed as

$$F_{em,n} = \frac{\sum\limits_{i=1}^{n} V_i(t)\ I_i(t)}{\dot{z}(t)\ \mu} \tag{2.24}$$

Using the above equations, the electromagnetic force for a single phase generator can be written as

$$F_{em}(t) = \frac{\left(\dfrac{2\pi\ B_t\ w_t\ d\ n\ q\ c}{w_p}\right)^2}{R_{load}\ \mu} \sin^2\left(\frac{2\pi}{w_p} z(t) - \delta\right) \dot{z}(t) \tag{2.25}$$

The electromagnetic force as calculated using Eq. 2.25 is the nonlinear damping force used in the mass-spring-damper model for the coupled PDE–LPG system [29]. The electrical damping thus calculated is crucial to optimize the power output of the coupled PDE–LPG system.

2.4 Coupled PDE–LPG Setup

Braun et al. [11, 13] established a proof-of-concept to use a PDE to drive an LPG and convert mechanical energy to electrical power. The preliminary work used the Friedlander model [12] to model the thrust generated by a PDE and did not study the effects of nonlinear damping on the performance of the energy conversion setup. The current work builds on the findings of the preliminary work and takes into account the nonlinear damping due to the architecture of the LPG. Since the Endo–Fujiwara model [4] is a more accurate representation of the thrust generated by a PDE, the current study uses the Endo-Fujiwara model. The proposed system to extract power consists of two main components. The first component is the PDE itself while the other component is the LPG fitted with the piston assembly. Both the subsystems are described in the earlier sections.

Depending on the configuration of the PDE and LPG coupling mechanism, the PDE thrust can generate many unique responses in the mass-spring-damper system. The optimum energy harvesting in any of these configurations requires a proper tuning between the energy harvesting device and the PDE operating frequency. A slight mistune can result in a large reduction in the power harvested. Depending on the configuration of the mass-spring-damper system, the governing equations of the configuration may not have a closed-form analytical solution. Therefore, it is not always possible to know the proper tuning parameters *a priori*.

In the following sections, two configurations of the mass-spring-damper system are introduced. The first configuration is a single degree-of-freedom vibration system with linear spring stiffness. The second configuration studied for this research is a vibration system with nonlinear softening spring stiffness. The merits and drawbacks of each configuration are also discussed.

2.4.1 Oscillator Configuration with Linear Spring Stiffness

The most common vibration-based energy harvesting configuration involves a resonant linear generator. Simple tuning and modeling methods make a linear configuration an attractive choice. However, good performance of linear configurations is limited to a narrow band of excitation frequency when the system operates at optimum tuning with its natural frequency coinciding with the external excitation frequency. The performance of the linear resonant oscillator drops off very rapidly away from the optimum tuning.

The linear single degree-of-freedom system set up is shown in Fig. 2.28. The piston is connected to the translator of the generator and is placed close to the open end of the PDE. A detonation wave exiting the PDE tube impacts a small area on the piston face and transfers energy to the piston, initiating reciprocating motion. The springs provide the restoring force and the linear generator provides the electromagnetic damping during the process of energy harvesting. The PDE is run at a predetermined frequency, such that the detonation waves transfer energy to the piston in an intermittent and optimum manner.

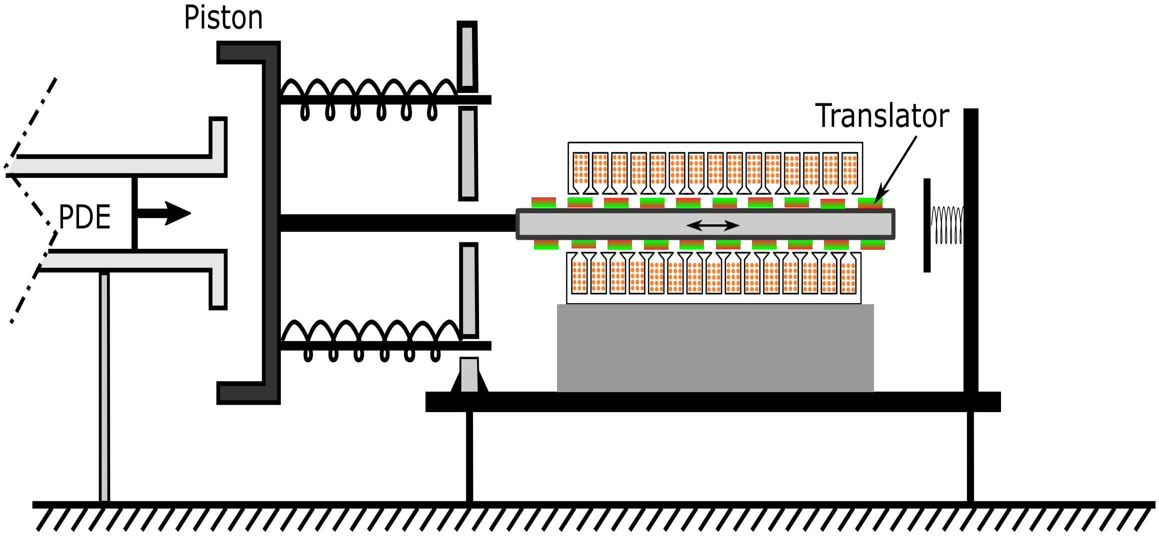

Figure 2.28: Energy conversion setup using a pulse detonation engine and a linear power generator.

The translator and piston assembly is constrained to move in a reciprocating manner only in the horizontal direction and it is assumed that there is no misalignment that can give rise to other degrees of freedom. Therefore, the system can be described as a single degree-of-freedom vibration system using

$$m\ddot{z}(t) + (C_m + C_{em}(t))\dot{z}(t) + kz(t) = F_{ext}(t) \tag{2.26}$$

where C_m is the mechanical damping coefficient, C_{em} is the electromagnetic damping coefficient and $F_{ext}(t)$ is the external force acting on the piston, which is given by

$$F_{ext}(t) = \begin{cases} Ap_3 & \text{if} \quad 0 \leq t \leq t_{pl} \\ Ap_3\left[\dfrac{k_{IV}\ t_{cj}}{(t - t_{pl}) + k_{IV}\ t_{cj}}\right]^{1/k_{II}} & \text{if} \quad t_{pl} \leq t \leq t_{ex} \end{cases} \tag{2.27}$$

where A is the area of piston impinged by the PDE exhaust. In the current model, it was assumed that the mechanical damping coefficient C_m was negligible compared to the electromagnetic damping coefficient C_{em} calculated using Eq. 2.25. Therefore, mechanical damping was not considered in analyzing the performance of the proposed system. It is assumed that the only source of nonlinearity in the system is the electromagnetic damping. The governing equation for the mass-spring-damper can be derived using Eqs. 2.25, 2.26, and 2.29. This results in a nonlinear differential equation with a piecewise continuous right-hand side. Since the governing equation has nonsmooth characteristics, special numerical treatment is needed to simulate the system. A review of the various numerical methods is the subject of the next chapter. Once a proper numerical integration scheme is selected, the system can be accurately simulated.

2.4.2 Oscillator Configuration with Nonlinear Softening Spring

Figure 2.29 shows a configuration of the mass-spring-damper system consisting of two linear springs connected to a mass and a damper with an inclination of $\pm\theta$ to the line perpendicular to the motion of the oscillator mass. The spring restoring force along the inclined axes is linear in nature but the arrangement results in a nonlinear restoring force in the direction of motion. This results in a softening nonlinear spring stiffness and under certain circumstances, a steeper displacement-time curve compared to the linear system.

Analysis of inclined springs: This section discusses the static analysis of the inclined spring arrangement and the resulting softening nonlinear spring stiffness. Figure 2.30 shows the inclined springs attached to the mass.

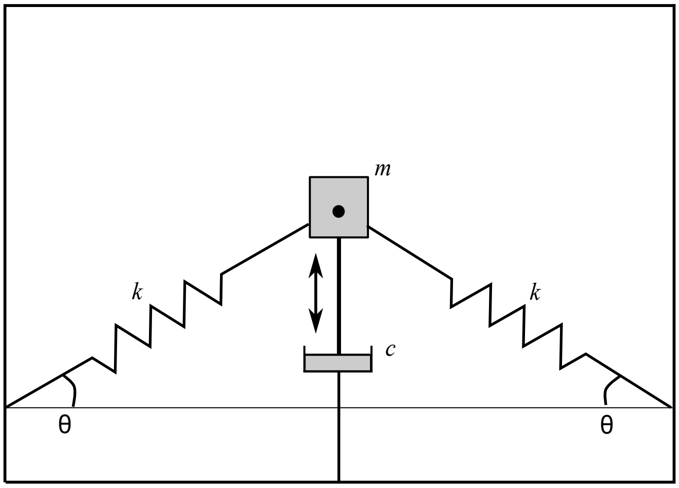

Figure 2.29: An arrangement of mass-spring-damper system leading to softening spring stiffness.

The total axial force F is given by

$$F = 2F_s \tag{2.28}$$

where F_s is the component of restoring force of each spring in x-direction. The total restoring force in the axial direction is given by

$$F = 2k(\sqrt{x^2 + l^2} - l_0)\sin\theta \tag{2.29}$$

where x is the displacement, $\sqrt{x^2 + l^2}$ is the length of the spring after deformation, l_0 is the undeformed length of the spring and θ is the angle of inclination of the spring. From Fig. 2.30,

$$\sin\theta = \frac{x}{\sqrt{x^2 + l^2}} \tag{2.30}$$

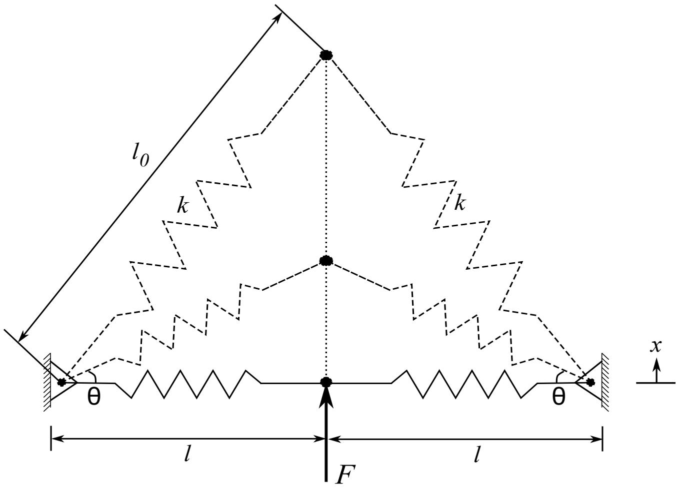

Figure 2.30: Spring arrangement and force acting on nonlinear oscillator with geometric nonlinearity.

Using (2.29) and (2.30), the restoring force F can be calculated as

$$F = 2k\left(1 - \frac{l_0}{\sqrt{x^2 + l^2}}\right)x \tag{2.31}$$

The restoring force in dimensionless form can be given by

$$\hat{F} = \left(1 - \frac{1}{\sqrt{\hat{x}^2 + \beta^2}}\right)\hat{x} \tag{2.32}$$

where $\hat{F} = \dfrac{F}{2kl_0}$, $\hat{x} = \dfrac{x}{l_0}$ and $\beta = \dfrac{l}{l_0}$. Figure 2.31 shows the dimensionless axial restoring force $\hat{F}$ for various values of the parameter β. The dimensionless stiffness of the system, $\hat{k} = \dfrac{d\hat{F}}{d\hat{x}}$ is

$$\hat{k} = 1 - \frac{\beta^2}{(\hat{x}^2 + \beta^2)^{\frac{3}{2}}} \tag{2.33}$$

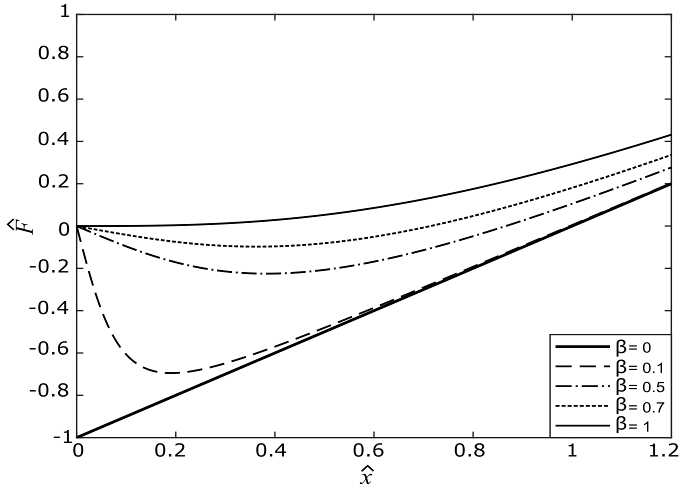

Figure 2.31: Dimensionless force $\hat{F}$ as a function of $\hat{x}$.

The change in dimensionless stiffness $\hat{k}$ of the system for various values of β is shown in Fig. 2.32. It can be observed that the dimensionless stiffness can be negative for certain values of β and $\hat{x}$, therefore, this arrangement is also known as a negative stiffness mass-spring-damper system.

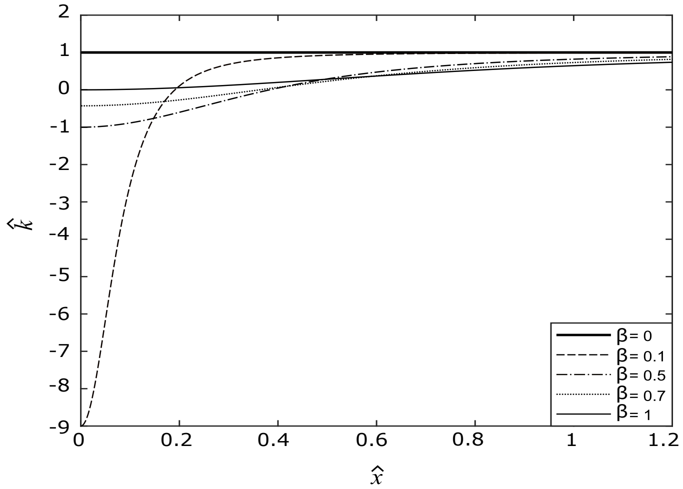

Figure 2.32: Dimensionless spring stiffness $\hat{k}$ as a function of $\hat{x}$.

The total potential energy of the system, E, is given by

$$E = 2\left[\frac{1}{2}k(\sqrt{x^2+l^2}-l_0)^2\right] \tag{2.34}$$

This dimensionless form of the total potential energy can be given by

$$\hat{E} = (\sqrt{\hat{x}^2+\beta^2}-1)^2 \tag{2.35}$$

where $\hat{E} = \dfrac{E}{kl_0^2}$. The variation of the dimensionless potential energy as a function of dimensionless displacement $\hat{x}$ is shown in Fig. 2.33.

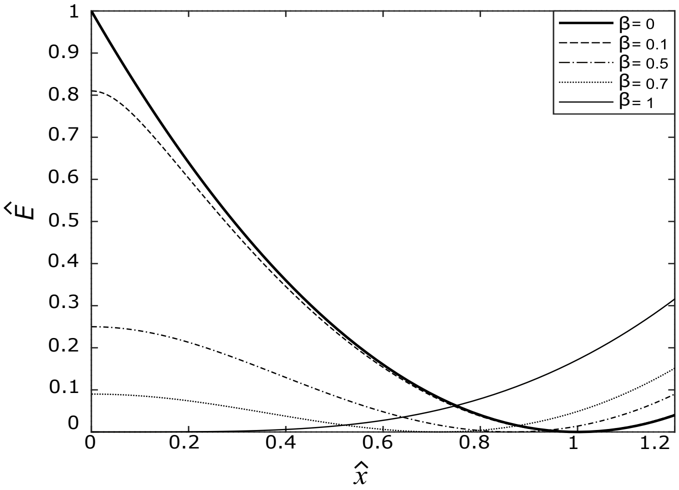

Figure 2.33: Dimensionless potential energy $\hat{E}$ as a function of $\hat{x}$.

The three equilibrium positions, $\hat{x}_{1,2,3}$ of the systems are given by

$$\hat{x}_{1,2} = \pm\sqrt{1-\beta^2} \quad \text{and} \quad \hat{x}_3 = 0 \tag{2.36}$$

The two equilibrium positions $\hat{x}_{1,2}$ are stable with minimum potential energy while the equilibrium position $\hat{x}_3$ is unstable with the maximum potential energy. The system will undergo a reciprocating motion around one of the two stable equilibrium positions for small-amplitude vibration. If the applied external force exceeds a critical value, the system will jump from one of the stable equilibrium positions to the other stable equilibrium position. The critical force required to enforce the snap-through is given by

$$\hat{F}_c = \frac{d\hat{F}}{d\hat{x}} = (1 - \beta^{\frac{2}{3}})^{\frac{3}{2}} \tag{2.37}$$

This shows that for smaller values of β, a larger force is required to change the behavior of the system and to enforce the oscillation to jump from one equilibrium position to the other. The position at which the jump occurs can be calculated by substituting $\hat{F}_c$ into Eq. 2.32 and is given by

$$\hat{x}_c = \beta^{\frac{2}{3}}\sqrt{(1 - \beta^{\frac{2}{3}})^{\frac{3}{2}}} \tag{2.38}$$

The results shown in Figs. 2.31, 2.32, and 2.33 only provide plots for the dimensionless force, dimensionless spring stiffness and dimensionless potential energy for a system oscillating about the equilibrium position given by $\hat{x} = +\sqrt{1-\beta^2}$. The results for the equilibrium point $\hat{x} = -\sqrt{1-\beta^2}$ would be symmetric about the vertical axis in the plots and would only be possible if there is a jump between the stable equilibrium positions.

Using Eqs. 2.25, 2.31, and 2.29, the equation of motion for a single degree-of-freedom nonlinear oscillator can be derived. Recall the nonlinear restoring force given by

$$F = 2k\left(1 - \frac{l_0}{\sqrt{x^2 + l^2}}\right)x \tag{2.39}$$

Using Taylor-series expansion to the third order, the nonlinear force can be written as

$$F = k_1 x \pm k_3 x^3 \tag{2.40}$$

Although Eq. 2.40 only shows the first couple of odd powers of x, the use of Taylor-series expansion permits the use of both odd and even powers of x in the description of the restoring force. Use of even powers of x in the expansion leads to a non-symmetric restoring force, which may be a desirable property in many cases. In practice, the second term in the above equation, $k_3 x^3$, is always positive. A cubic term with a negative sign leads to a trivial solution leading to all solutions of the governing equation exponentially tending to infinity.

Since both linear oscillator and the nonlinear oscillator governing equations consist of a nonsmooth term, the numerical simulation needs careful treatment in the neighborhood of the discontinuity. The following chapter introduces numerical techniques capable of handling the discontinuity and presents the results of numerical simulation for both types of oscillators.

CHAPTER 3

Numerical Methods for Nonsmooth Dynamical Systems

Dynamical systems with nonsmooth governing equations occur naturally in the description of physical processes. That is, the motion of such systems involves a smooth evolution interrupted by instantaneous events. Due to the widespread application of such systems to biological systems, control problems and bifurcation problems, nonsmooth dynamical systems are receiving a lot of attention. Brogliato [30], Kunze [31] and Liene et al. [32] are a comprehensive collection of recent advances made in the field of nonsmooth dynamics and bifurcation. The earlier studies of nonsmooth dynamics appeared mostly in East European literature. The works of Andronov et al. [33] on nonsmooth bifurcations, Feigin [34, 35] on C-bifurcations, Peterka [36] and Babitskii [37] on impact oscillators and Filippov [38] on sliding motion are notable. From this and other literature, one finds that nonsmooth dynamical systems are feature-rich and complex.

Only a small number of dynamical systems with nonlinear governing equations have closed-form solutions. Therefore, their studies rely heavily on simulation. The governing equations discussed in Ch. 2 are nonautonomous nonsmooth differential equations. It is essential to understand the numerical methods that are available for the proper treatment of the discontinuity in the governing equations. The work of Acary and Brogliato [39] provides a detailed description of the numerical methods for nonsmooth dynamical systems in mechanics and electronics. Dieci and Lopez [40] provided a survey of numerical methods that can be used to numerically integrate discontinuous differential equations.

In the following sections, a brief overview of two numerical methods from Dieci and Lopez is presented. These methods are evaluated for application to the system being studied for this research. Later, the governing equations introduced in Chapter 2 are simulated and the results are presented.

3.1 Introduction

Consider a dynamical system defined by

$$\dot{x} = f(x), \qquad x(0) \text{ given} \tag{3.1}$$

where $f : \mathbb{R}^m \mapsto \mathbb{R}^m$ is a given m-dimensional vector field. When solving Eq. 3.1 numerically, the convergence analysis of any numerical method relies on the assumption that the vector field f and the solution are *sufficiently smooth*. In the absence of smoothness, most stepsize control techniques and their local truncation error analysis fail to be valid locally in the neighborhood of the discontinuity. Therefore, a numerical method can possibly become inaccurate or inefficient, or both, in the regions of nonsmoothness in the solution or its derivatives.

Dieci and Lopez [40] compiled a survey of many numerical methods typically used to numerically integrate differential equations with discontinuous right-hand sides. One of the strategies to treat such discontinuities, known as *time stepping methods*, simply ignores the nonsmoothness and relies on the local error estimation to ensure that the error remains small and acceptable. Another strategy to treat any nonsmooth characteristics is to locate the discontinuity using an *event function* $h : \mathbb{R}^m \mapsto \mathbb{R}$. The function h can be used to define the discontinuity surface, generally represented by $\Sigma = \{x \in \mathbb{R}^s | h(x) = 0\}$ in the state space of the dynamical system. This method requires the knowledge of h. Once the numerical solution reaches the discontinuity hypersurface Σ, an *event point* is defined and the numerical integration can restart from this point. Such methods are known as *event-driven methods*. Piiorrnen et al. [41] presented an algorithm and a MATLAB routine to simulate Filippov-type systems using event-driven methods. The third course of action is to *regularize* or smoothing the dynamical system [42]. Regularization methods lead to simplification in theory as the modified systems can be treated with the classical theory of ODEs and the existence and uniqueness of solutions can be derived with well-established procedures. However, numerical methods with smoothing require small integration steps due to the large derivatives present in the system. This results in the regularized system becoming quite *stiff*. Another drawback of regularizing is the possibility of changing the dynamics of the original nonsmooth system [43]. Even in the presence of these shortcomings, regularization is a reasonable routine for conducting a preliminary exploratory study of a problem. To understand the behavior of dynamical systems with discontinuous right-hand side and their numerical treatment, let us start with an example used by Stewart [44]. The problem describes a brick moving on an inclined ramp as shown in Fig. 3.1.

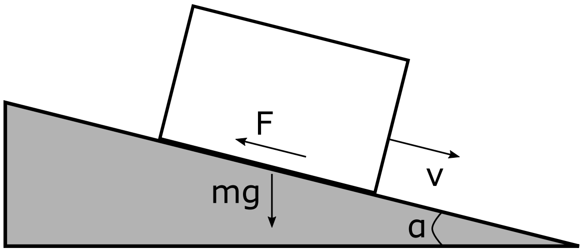

Figure 3.1: A block sliding down a ramp with Coulomb friction.

In this case, the two forces acting on the brick are gravity g and a friction force F. These two forces act opposite to each other: gravity would make the brick slide down the ramp, while friction would oppose the sliding motion. Using *Coulomb law*, the equation of motion for the brick becomes

$$m\dot{v}(t) = mg\sin\alpha - \mu mg\cos\alpha \; sgn[v(t)] \tag{3.2}$$

where "sgn" is the sign function defined as

$$sgn[v] = \begin{cases} 1, & v > 0, \\ 0, & v = 0, \\ -1, & v < 0. \end{cases} \tag{3.3}$$

The system can show interesting behavior depending on whether it satisfies one of the two following conditions

(i) $\sin\alpha - \mu\cos\alpha > 0$
(ii) $\sin\alpha - \mu\cos\alpha < 0$

In case (i), $v(t)$ keeps increasing forever. This is the simpler of the two cases. However, in case (ii), if $v(0) > 0$, v will decrease to 0 and if $v(0) < 0$, then v increases to 0. what happens at $v = 0$? Mathematically, $\dot{v} > 0$, which would make v grow an become positive. But it would have to immediately decrease back to 0. In the physical world, we expect that the brick will stop and remain at $v = 0$ forever.

In the above example, the vector field becomes discontinuous at some point and represents a classic case of a Filippov system [38, 45, 46]. The solution x remains continuous but its derivative $\dot{x}$ will have a jump at the discontinuity. This results in a model defined by

$$\dot{x} = f(x) = \begin{cases} f_1(x) & when \quad h(x) < 0, \\ f_2(x) & when \quad h(x) < 0. \end{cases} \tag{3.4}$$

where the *event function* $h : \mathbb{R}^m \mapsto \mathbb{R}$ is known, and the known initial condition $x(t_0) = x_0$ such that $h(x_0) < 0$. The state space $\mathbb{R}^m$ is divided into two regions R_1 and R_2 by the discontinuity hypersurface Σ as shown in Fig. 3.2.

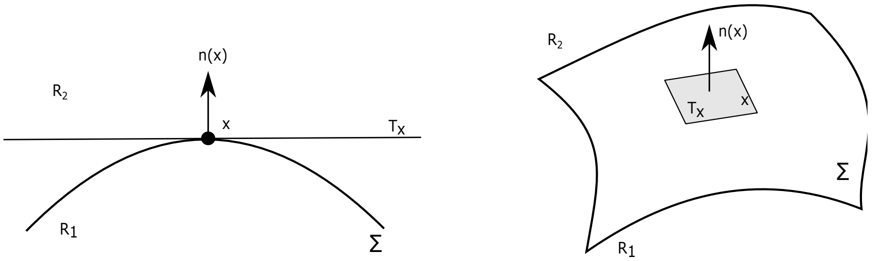

Figure 3.2: The surface, tangent plane and normal vector in 1D and 2D.

R_1, R_2 and Σ are defined by

$$R_1 = \{x \in \mathbb{R}^m | \; h(x) < 0\} \tag{3.5}$$

$$R_2 = \{x \in \mathbb{R}^m | \; h(x) > 0\} \tag{3.6}$$

$$\Sigma = \{x \in \mathbb{R}^m | \; h(x) = 0\} \tag{3.7}$$

such that $\mathbb{R}^m = R_1 \cup \Sigma \cup R_2$. It is assumed that the gradient of h at $x \in \Sigma$ is always non-zero, i.e., $h_x(x) \neq 0$ for all $x \in \Sigma$. This formalism also allows the possibility of $f_1(x) \neq f_2(x)$ for all $x \in \Sigma$.

The numerical method used to accurately simulate any system defined by Eq. 3.4 is required to predict the behavior of the system in the neighborhood of the hypersurface Σ. Broadly, the solution orbit can behave in three distinct manners in the neighborhood of Σ as shown in Fig. 3.3 below:

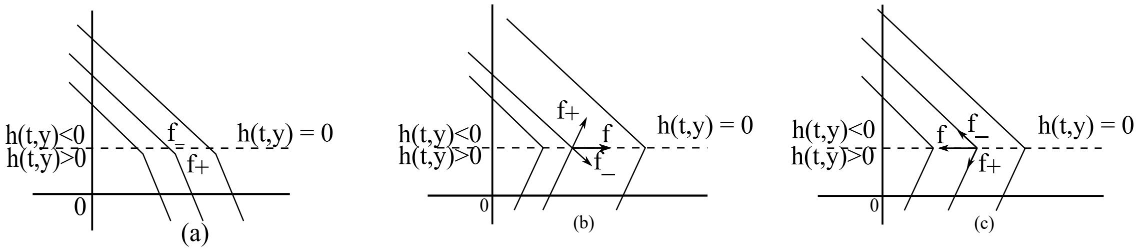

Figure 3.3: Discontinuity hypersurface and behavior of solution orbit in the neighborhood of the hypersurface.

The solution $x(t)$ can either reach the hypersurface and cross it transversally as shown in Fig. 3.3(a) or it can stay on the hypersurface as shown in Figs. 3.3(b) and (c). Once the solution starts *sliding* on the hypersurface, it can either stay on the hypersurface indefinitely or leave the surface after some time. Many numerical methods in the literature assume that the solution trajectories cross the hypersurface Σ as they reach it [43]. For this reason, it is important to first define the *transversality condition.* The transversality condition implies that any solution trajectory $x(t)$ that reaches the hypersurface Σ from above (or below) will cross the hypersurface without *sliding* or undergoing a spontaneous jump on it. Mathematically, for $x \in \Sigma$, there exists a $\delta > 0$ such that

$$h_x^t(x)f_1(x) \geq \delta > 0, \qquad h_x^t(x)f_2(x) \geq \delta > 0 \tag{3.8}$$

Having defined the transversality condition, a discussion of various numerical methods for the nonsmooth system can be undertaken.

3.2 Explicit Euler Method: Local Error Order Reduction

Consider the discontinuous differential system defined by Eq. 3.4 and assume transversality as defined by Eq. 3.8. Let x_k and x_{k+1} be the approximations of an exact solution respectively at given times t_k and t_{k+1} with the time step given by $\tau = t_{k+1} - t_k$. The condition $h(x_k)h(x_{k+1}) < 0$ indicates that an event has occurred in the time interval (t_k, t_{k+1}). Let $x(t; x_k, t_k)$ be the exact solution of the local system in the time duration given by $t \in (t_k, t_{k+1})$, $x(t_k) = x_k$ and let $\breve{x}(t) = x_k + (t - t_k)f_1(x_k)$ be the continuous extension of the Euler method. Let $\tilde{\xi} \in (t_k, t_{k+1})$ be a unique value for which $h(\breve{x}(\tilde{\xi})) = 0$. Also assume that a unique $\xi \in (t_k, t_{k+1})$ exists, for which $h(x(\xi; x_k, t_k)) = 0$.

The local truncation error is given by

$$e_{k+1} = x(t_{k+1}; x_k, t_k) - x_{k+1} = x(t_{k+1}; x_k, t_k) - x_k - \tau f_1(x_k) \tag{3.9}$$

Using Taylor's expansion for the local exact solution gives

$$x(t_{k+1}; x_k, t_k) = x(\xi; x_k, t_k) + (t_{k+1} - \xi)f_2(x(\xi; x_k, t_k)) + O((t_{k+1} - \xi)^2) \tag{3.10}$$

$$x(\xi; x_k, t_k) = x_k + (\xi - t_k)f_1(x_k) + O((\xi - t_k)^2 \tag{3.11}$$

From the above two equations,

$$
\begin{aligned}
e_{k+1} &= x(\xi; x_k, t_k) + (t_{k+1} - \xi) f_2(x(\xi; x_k, t_k)) - x_k - \tau f_1(x_k) \\
&\quad + O((t_{k+1} - \xi)^2) \\
&= (\xi - t_k) f_1(x_k) + (t_{k+1} - \xi) f_2(x(\xi; x_k, t_k)) - \tau f_1(x_k) \\
&\quad + O((\xi - t_k)^2) + O((\xi - t_{k+1})^2) \\
&= (t_{k+1} - \xi)[f_2(x(\xi; x_k, t_k)) - f_1(x_k)] + O(\tau^2)
\end{aligned}
\tag{3.12}
$$

Now rewriting,

$$
\begin{aligned}
f_1(x_k) &= f_1(x(\xi; x_k, t_k)) + Df_1(x(\xi; x_k, t_k))(x_k - x(\xi; x_k, t_k)) \\
&\quad + (||x_k - x_k(\xi; x_k, t_k)||^2) \\
&= f_1(x(\xi; x_k, t_k)) + O(\xi - t_k)
\end{aligned}
\tag{3.13}
$$

where Df_1 is the Jacobian matrix of f_1. The expression for local error becomes

$$
e_{k+1} = (t_{k+1} - \xi)[f_2(x(\xi; x_k, t_k)) - f_1(x(\xi; x_k, t_k))] + O(\tau^2) \tag{3.14}
$$

from which

$$
||e_{k+1}|| \leq \tau J + O(\tau^2) \tag{3.15}
$$

where

$$
J = ||f_2(x(\xi; x_k, t_k)) - f_1(x(\xi; x_k, t_k))|| \tag{3.16}
$$

is the jump in the vector field at the point of discontinuity.

Using the local truncation error e_{k+1} in terms of the jump of the vector field, two observations can be made:

(i) $x(\xi; x_k, t_k) = x_k + (\xi - t_k) f_1(x_k) + O((\xi - t_k)^2)$,

(ii) $\breve{x}(\tilde{\xi}) = x_k + (\tilde{\xi} - t_k) f_1(x_k)$,

Therefore,

$$x(\xi; x_k, t_k) = \breve{x}(\tilde{\xi}) + (\xi - \tilde{\xi}) f_x(x_k) + O((\xi - t_k)^2) \tag{3.17}$$

Thus,

$$\begin{aligned} e_{k+1} &= (t_{k+1} - \tilde{\xi})[f_2(\breve{x}(\tilde{\xi})) - f_1(\breve{x}(\tilde{\xi}))] + (\tilde{\xi} - \xi)[f_2(\breve{x}(\tilde{\xi})) - f_1(\breve{x}(\tilde{\xi}))] + O(\tau^2) \qquad (3.18) \\ &= (t_{k+1} - \tilde{\xi})[f_2(\breve{x}(\tilde{\xi})) - f_1(\breve{x}(\tilde{\xi}))] + O(\tau^2) \qquad (3.19) \end{aligned}$$

since $\tilde{\xi} - \xi = O(\tau^2)$ (to be shown later),

$$||e_{k+1}|| \leq \tau J_1 + O(\tau^2) \tag{3.20}$$

where $J_1 = ||f_2(\breve{x}(\tilde{\xi})) - f_1(\breve{x}(\tilde{\xi}))||$.

To verify $\xi - \tilde{\xi} = O(\tau^2)$, Consider that

$$h(\breve{x}(\tilde{\xi})) = h(x_k) + h_x^T(x_k)(\breve{x}(\tilde{\xi}) - x_k) + O(||\breve{x}(\tilde{\xi} - x_k||^2) \tag{3.21}$$

Now, since

$$h(x(\xi; x_k, t_k)) = 0 \tag{3.22}$$

and

$$x(\xi; x_k, t_k) = x_k + (\xi - t_k) f_1(x_k) + O((\xi - t_k)^2), \tag{3.23}$$

Therefore,

$$0 = h(x_k) + (\xi - t_k) h_x^T(x_k) f_1(x_k) + O((\tilde{\xi} - t_k)^2). \tag{3.24}$$

Comparing these expressions,

$$0 = (\xi - \tilde{\xi}) h_x^t(x_k) f_1(x_k) + O(\tau^2) \tag{3.25}$$

and therefore,

$$(\xi - \tilde{\xi}) = O(\tau^2) \tag{3.26}$$

because

$$h_x^T(x_k) f_1(x_k) \neq 0 \tag{3.27}$$

The explicit Euler method discussed here for the numerical solution of discontinuous differential equations under the assumption of transversality has one or more special step(s) with the local truncation error of first order instead of second order. Nonetheless, this reduction in local order does not impact the error accumulation negatively.

3.3 Runge–Kutta Time-Stepping Methods

This section reviews the basics for the use of Runge–Kutta methods when the discontinuities present in the governing equations of the dynamical system are located by monitoring the local truncation errors. Several authors have proposed this approach [47, 48].

Consider the discontinuous system given by

$$\begin{cases} x' = f(x) = f_1(x) \qquad \text{when } t < \xi \\ f_2(x) \qquad \text{when } t \geq \xi \end{cases} \tag{3.28}$$

Assume that the discontinuity time ξ is in $[t_k, t_{k+1}]$ for both the exact solution and the numerical method. Take an embedded pair of explicit s-stage Runge–Kutta methods of order p and $\hat{p}$. The usual case is when $\hat{p} = p - 1$ or $\hat{p} = p + 1$, given the Butcher array $A = a_{ij} \in \mathbb{R}^{s \times s}, c = (c_i) \in \mathbb{R}^s, b = (b_i) \in \mathbb{R}^s, \bar{b} = (\bar{b}_i) \in \mathbb{R}^s$. Suppose that $[t_k, t_{k+1}]$ is the interval where discontinuity occurs, that $x(t_k) - x_k = O(\tau^{p^*})$, where $p^* = \max\{p, \hat{p}\}$ and the transversality condition holds. Then, on a successive step, the solution is advanced with the higher-order method:

$$x_{k+1} = x_k + \tau \sum_{i=1}^{s} b_i f(X_{ki}), \tag{3.29}$$

$$\text{where} \qquad \mathrm{X_{ki}} = x_k + \tau \sum_{j=1}^{i-1} a_{ij} f(X_{kj}), \quad i = 1, ..., s \tag{3.30}$$

Assume that a nonempty subset I_1 of the index set $\{1, ..., s\}$ exists such that $f(X_{kj}) = f_1(X_{kj})$ when $j \in I_1$. This means X_{kj} with $j \in I_1$ is the approximation of the solution at a value of $t \in (t_k, \xi)$. Similarly, there is a nonempty subset $I_2 = \{1, ..., s\} - I_1$ such that $f(X_{kj}) = f_2(X_{kj})$ when $j \in I_2$ is the approximation of the solution at a value of $t \in (\xi, t_{k+1})$. An estimate of the local truncation error (LEE) may be computed as the difference of the solutions of orders p and $\hat{p}$:

$$LEE = \tau \sum_{i=1}^{s} (b_i - \bar{b}_i f(X_{ki}) \tag{3.31}$$

The error estimate LEE is compared to the accuracy level ϵ which is derived from a user prescribed accuracy parameter *tol* by a mixture of relative and absolute criterion:

$$\epsilon = \text{tol} \max\{1, \|x\|_\infty\} \tag{3.32}$$

If the error estimate is smaller than the prescribed level ϵ, that is, if $LEE < \epsilon$, then the numerical solution is advanced using the time step τ. Otherwise the step size is reduced according to the criterion :

$$\tau_{new} = C \left| \frac{\epsilon}{\|LEE\|} \right|^{1/p^*} \tau_{old} \tag{3.33}$$

where $0 < C < 1$ is some constant to ensure a cautious step size choice. A new estimate of LEE is computed and tested. For smooth systems, the quantity

$$\frac{LEE}{\tau} = \sum_{i=1}^{s} (b_i - \bar{b}_i) f(X_{ki}) \tag{3.34}$$

approaches 0 when $\tau \to 0$, while for discontinuous systems, this quantity approaches the jump of the vector field f at the discontinuity point. Thus the algorithm can only pass the accuracy test of $LEE < \epsilon$ when the step size τ is decreased to

$$\tau_{pass} = \frac{\epsilon}{J}, \qquad J = \lim_{\tau \to 0} \frac{LEE}{\tau} \tag{3.35}$$

In addition to the two methods described here, many other methods such as the work presented by Mannshardt [49], the Gear- østerby method [50], the event location method and the numerical method for Filippov systems [38] exist for studying nonsmooth systems. The choice of method for studying any system generally depends on the form of the governing equation of the system. For the current system, a fourth-order Runge–Kutta method was used with local error estimate tolerance of $1e^{-6}$.

3.4 Results of Numerical Simulations

The governing equations for the coupled PDE–LPG oscillator system were introduced in Ch. 2. The governing nonsmooth, nonautonomous differential equations require special treatment in the neighborhood of the discontinuity to accurately simulate the system. Since transversality is assumed, a numerical method dealing with sliding on the discontinuity hypersurface is not required. For the linear oscillator, a fourth-order Runge–Kutta method was used to simulate the system. Table 3.1 shows the system parameters used in the simulation.

Table 3.1: Parameters of PDE–LPG coupled system for linear oscillator model

Parameter	Symbol	Value	Unit
Magnetic field in tooth	B_t	1.2	T
Number of cables in slot	c	50	–
Width of stator sides	d	0.2	m
Spring stiffness	k	25	kN/m
Mass of translator	m	45	kg
Number of poles	n	6	–
Winding ratio	q	1	–
Load resistance	R_{load}	30	Ω
Pole width	w_p	0.05	m
Tooth width	w_t	0.01	m

Figure 3.4 shows the displacement, the velocity, the electromagnetic force and the power generated by the coupled system with linear spring stiffness. The displacement curve in the plot is a smooth sinusoidal curve while the velocity curve shows an abrupt jump. Since the PDE operating frequency is one-third of the undamped natural frequency of the system, the piston completes three cycles before the next detonation wave impinges on it. The maximum velocity achieved is at the instant of detonation wave impinging on the piston. The electromagnetic force and output power are a function of the piston velocity. Therefore, they also exhibit a peak value at peak velocity.

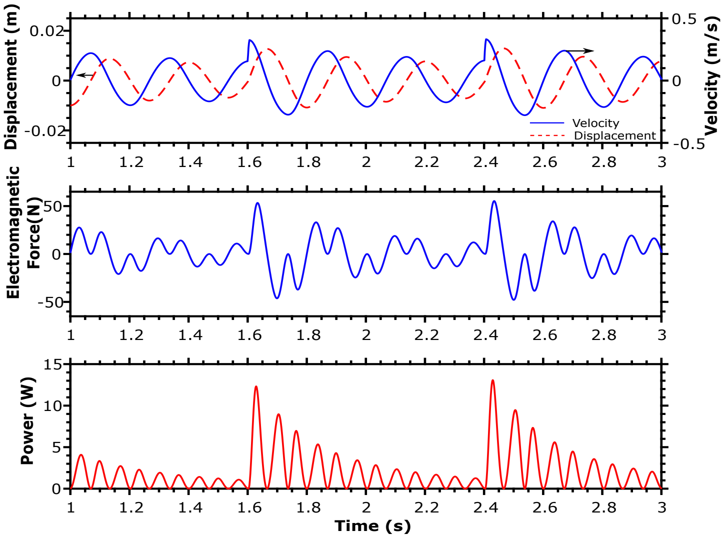

Figure 3.4: System performance of linear oscillator for PDE operating frequency of 1.25 Hz.

Figure 3.5 shows the results of the simulation for a system with linear spring stiffness operating at 1:1 resonance with PDE operating frequency. For a coupled PDE–LPG oscillator system with linear spring stiffness, a 1:1 resonance operation produced the maximum amount of power. However, the power generation drops off very rapidly away from the resonance frequency as seen in Fig. 3.7.

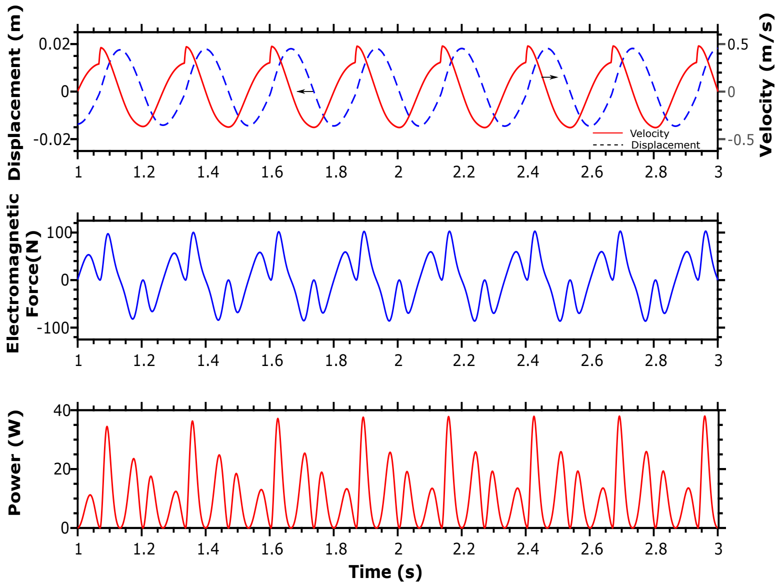

Figure 3.5: System performance of linear oscillator for PDE operating frequency of 3.75 Hz.

Figure 3.6 shows the results of the simulation for the PDE operating frequency of 11.25 Hz. At this operating frequency, the piston-translator assembly cannot complete cycles of oscillations before a new detonation wave impinging on the piston. This results in a sub-optimal performance due to the canceling of motion of the piston by successive detonation pulses.

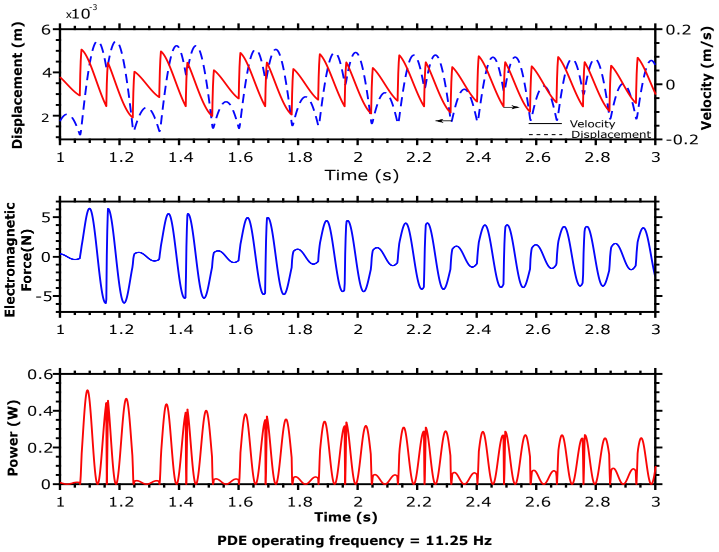

Figure 3.6: System performance of linear oscillator for PDE operating frequency of 11.25 Hz.

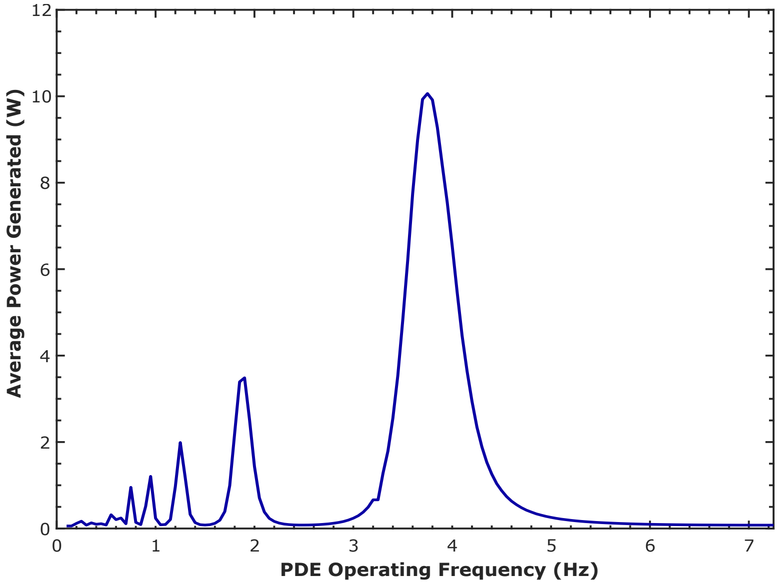

Figure 3.7: Average power generated by linear oscillator as a function of PDE operating frequency.

Phase portraits are plots of a system position versus velocity. Using the simulation data, phase portraits of the oscillator system with linear spring stiffness are shown in Fig. 3.8. The plot shows the phase portraits of the system operating at 1.25 Hz, 1.875 Hz, 3.75 Hz, and 11.25 Hz. Note the enlarged scale in Fig 3.8(d).

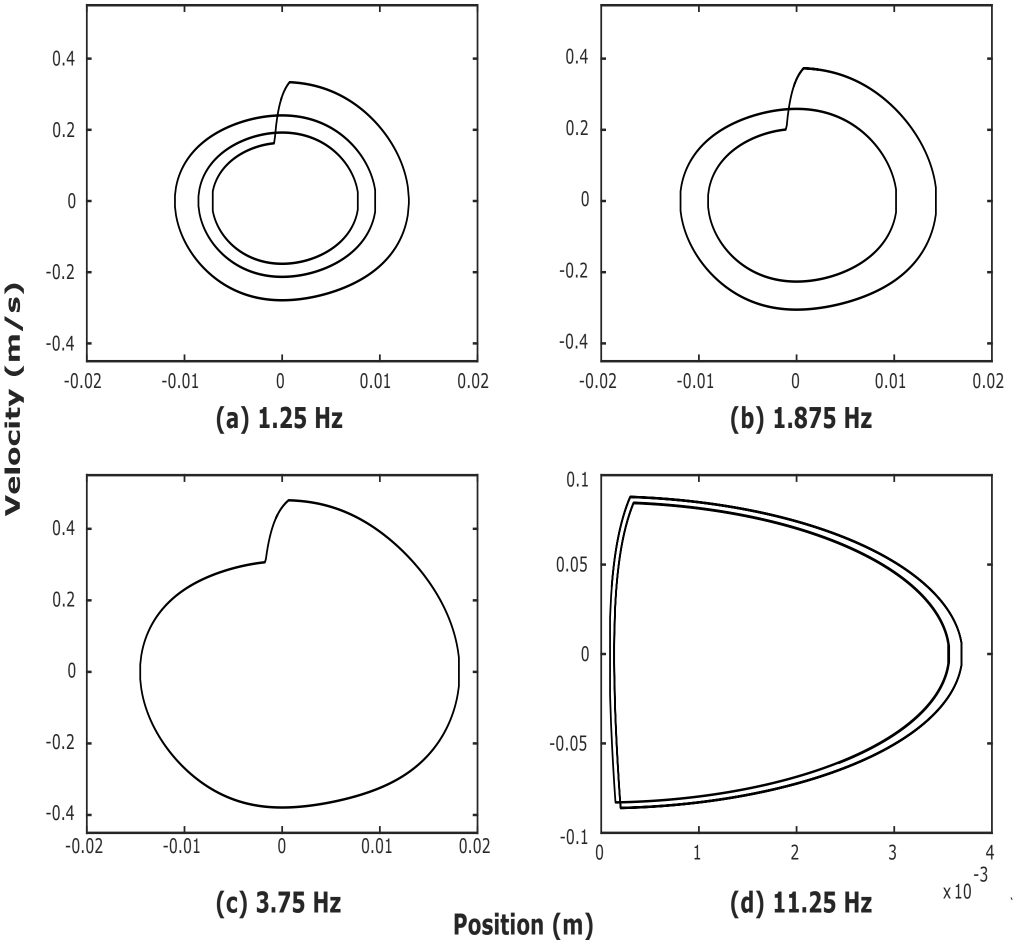

(a) 1.25 Hz

(b) 1.875 Hz

(c) 3.75 Hz

(d) 11.25 Hz

Figure 3.8: Limit cycles of linear oscillator operating at different PDE frequencies.

The parameters used for simulating the system performance for the coupled PDE–LPG system with geometric nonlinearity is shown in Table 3.2. The geometric nonlinearity gives rise to a cubic spring stiffness. Based on the geometry, a parameter β is defined as

$$\beta = \frac{l}{l_0} \tag{3.36}$$

The ratio of forcing frequency to the natural frequency of the system is also defined as

$$\Omega = \frac{\omega}{\omega_n} \tag{3.37}$$

Table 3.2: Parameters of PDE–LPG coupled system for nonlinear oscillator model

Parameter	Symbol	Value	Unit
Magnetic field in tooth	B_t	1.2	T
Number of cables in slot	c	50	–
Width of stator sides	d	0.2	m
Spring stiffness	k	250	kN/m
Mass of translator	m	32	kg
Number of poles	p	6	–
Winding ratio	q	1	–
Load resistance	R_l	30	Ω
Pole width	w_p	0.05	m
Tooth width	w_t	0.01	m

Figure 3.9 shows the phase portrait of the oscillator with softening nonlinear damping achieved using the geometric nonlinearity. The system was simulated for $\beta = 0.5$ and 1:1 resonance condition. The phase portrait shows that the oscillator starts in one of the two stable equilibrium positions, but due to the PDE thrust, jumps to the second equilibrium point and oscillates about this equilibrium.

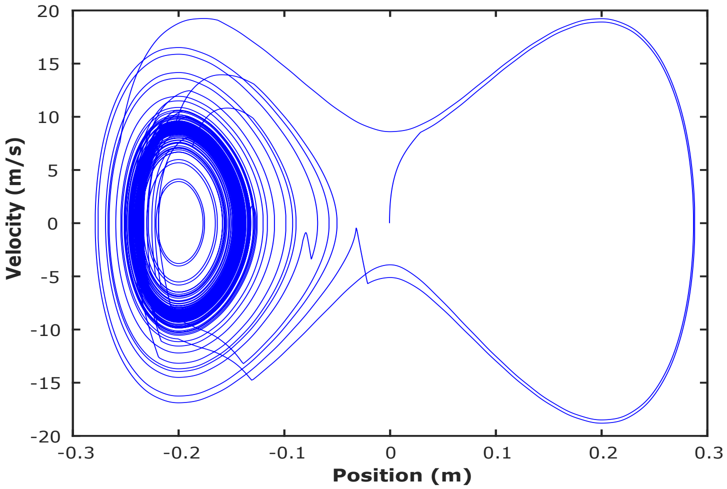

Figure 3.9: Phase portrait of mass-spring-damper system with softening nonlinear spring stiffness.

Figure 3.10(a) shows the power generated by the coupled system with linear spring stiffness. Since there is no geometric nonlinearity involved in this case, the three plots, in the clockwise direction, show the power extracted at $\Omega = 0.25$, 0.5, and 1. Parts (b) and (c) of Fig. 3.10 show the power generated by system with geometric nonlinearity and $\beta = 0.1$ and 0.5 respectively.

Comparing the power generated by the coupled system with linear spring stiffness and that by the system with geometric nonlinearity shows that a system with softening nonlinear spring generates more power for low values of β for all values of Ω. As the β value increases, any potential advantage of using a more complex geometry with nonlinear spring stiffness is lost. The maximum power extracted was observed in a system with $\beta = 0.1$ operating at 1:1 resonance.

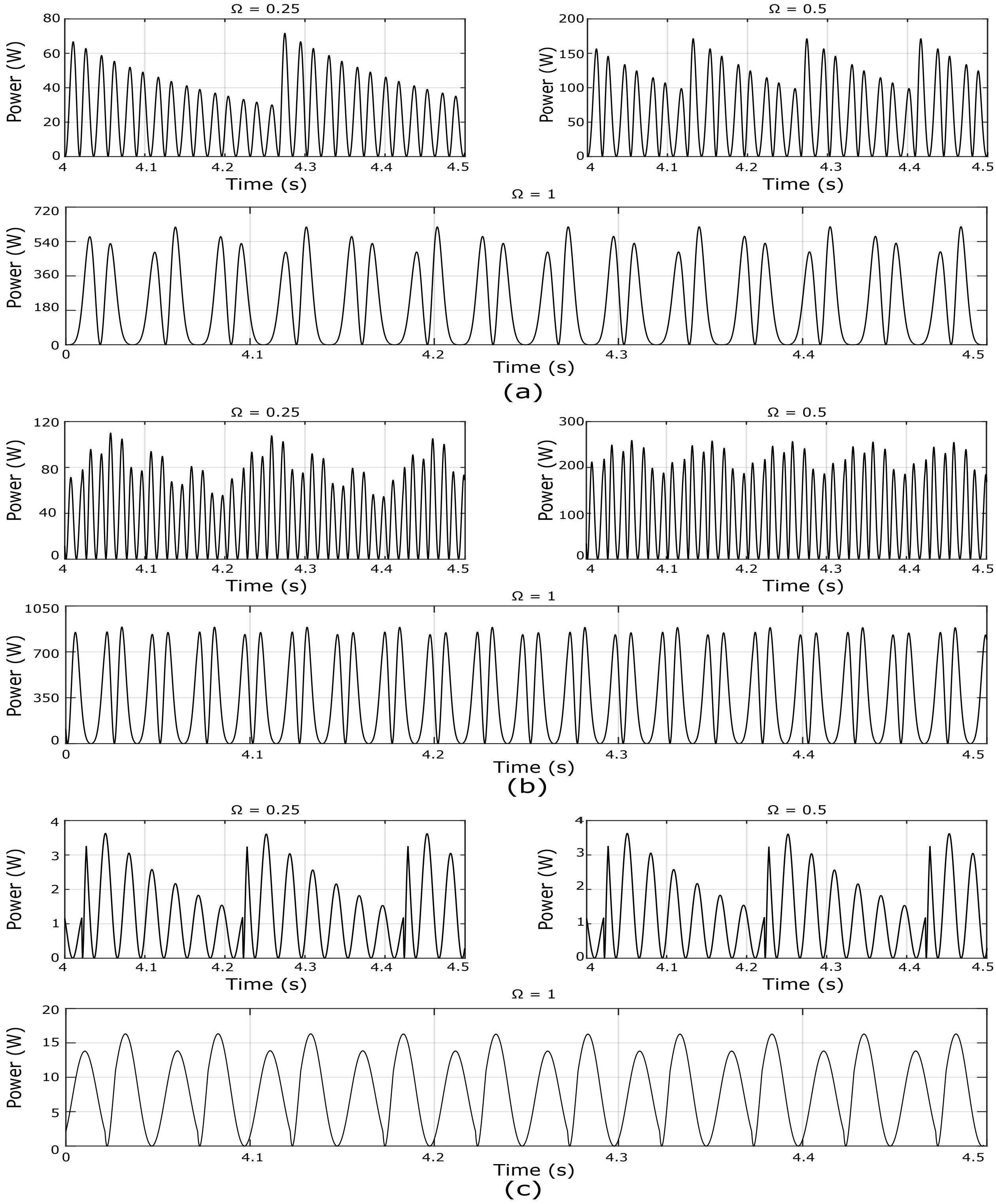

(a)

(b)

(c)

Figure 3.10: Comparison of linear oscillator performance with nonlinear oscillator for different values of β and Ω.

Understanding the conditions related to the stability of any dynamical system plays a critical role in studying the long-term behavior of the dynamical system. As long-term stability can have serious implications on the operation of any system, a proper understanding of stability is imperative. One of the commonly used methods to study the long term stability of a dynamical system is by using Lyapunov exponents. The following section introduces the concept of Lyapunov exponent and how it can be used to study the stability of a dynamical system. Later, the concept is applied to the coupled system with linear spring stiffness and to the system with geometric nonlinear stiffness.

3.5 Lyapunov Exponent and Stability of Dynamical Systems

Lyapunov exponents describe the exponential rate of divergence or convergence of nearby trajectories and are a key component of chaotic dynamics. Consider two trajectories defined by $x(t) = f(x_0)$ and $x(t)+\delta x(t) = f(x_0+\delta x_0)$ that start out very close to each other and separate or collapse exponentially with time. The sensitivity to initial conditions can be given by

$$||\delta x(t)|| \approx e^{\lambda t}||\delta x_0|| \tag{3.38}$$

where λ is the mean rate of separation of trajectories of the system and is called the *Lyapunov exponent.*

The mean growth rate of the distance between neighboring trajectories is given by the Lyapunov exponent and can be calculated as

$$\lambda \backsimeq \frac{1}{t} \ln \frac{||\delta x(t)||}{||\delta x(0)||} \tag{3.39}$$

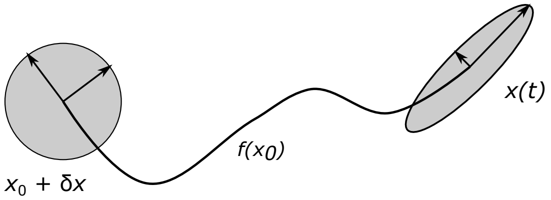

Figure 3.11: Evolution of a swarm of initial points in an infinitesimal spherical neighborhood over time.

The above equation can be used to determine the Lyapunov exponent as follows. First, take two nearby trajectories that are separated by δx_0 and track the distance between them until the separation $||\delta x(t_1)||$ gets significantly big. Next, record $t_1\lambda_1 = \ln(||\delta x(t_1)||/||\delta x_0||)$. The next step is to rescale $\delta x(t_1)$ by a factor of $\delta x_0/\delta x(t_1)$ and keep repeating for a large number($\sim$ 10,000) times. The leading Lyapunov exponent is then given by

$$\lambda = \lim_{t\to\infty} \frac{1}{t}\sum_i t_i\lambda_i, \qquad t = \sum_i t_i \tag{3.40}$$

For autonomous dynamical systems, the maximum Lyapunov exponent is calculated using the solution of variational equations of the systems. However, for many dynamical systems, the task of formulating and solving variational equations is a difficult task. As a result, many different algorithms have been formulated by many researchers to provide alternate procedures to calculate Lyapunov exponents. Geist et al. [51] and Tancredi et al. [52] provided a comparison of various methods for computing Lyapunov exponents. Wolf et al. [53] provided an algorithm to compute Lyapunov exponents from a time series. Since the simulations carried out to study the coupled system generate a time series data of position and velocity, Wolf's algorithm to determine the maximum Lyapunov exponent is the most suitable and can be easily implemented.

Figure 3.12 shows the maximum Lyapunov exponent of a linear oscillator, a nonlinear oscillator with $\beta = 0.1$, $\beta = 0.5$, and the Rossler chaotic attractor [54]. The maximum Lyapunov exponent for both the linear oscillator and nonlinear oscillator tend to a value of zero as the number of iterations increase.

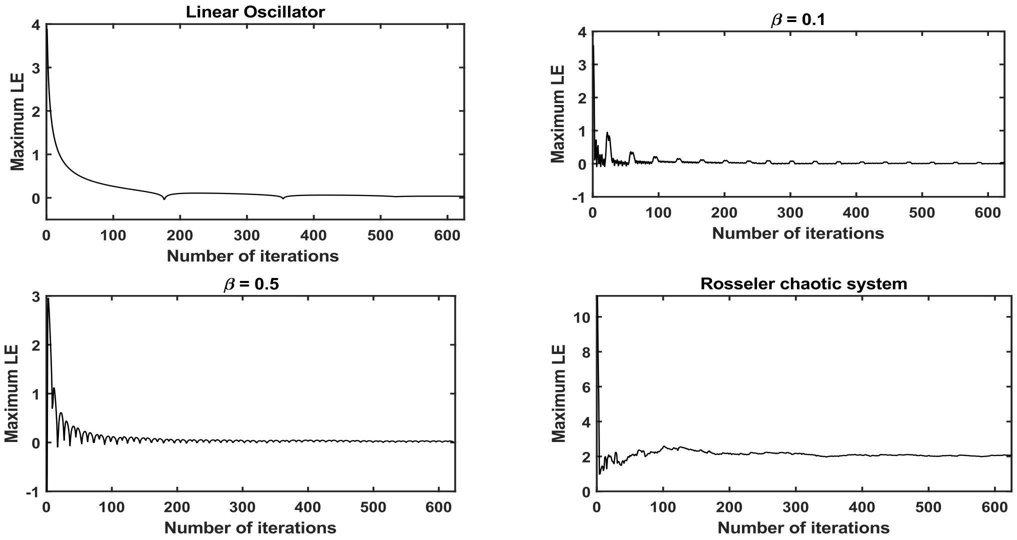

Figure 3.12: Maximum Lyapunov exponent of various configurations of mass-spring-damper system.

Since the governing equations defined in the previous chapters do not have a closed-form solution, study of the coupled system relies on numerical simulations. However, this also means that every set of parameter values will yield a different result and the simulation will have to be carried out for individual cases. This is a brute force method and somewhat tedious if a large number of simulations have to be carried out. The qualitative study of nonlinear systems and their bifurcation analysis provide a solution to this problem. Therefore, the next chapter introduces the concepts required to study the nonlinear systems qualitatively.

CHAPTER 4

Qualitative Theory of Dynamcial Systems

This chapter provides an overview of the basic theory of dynamical systems. A detailed description of the qualitative theory of dynamical systems was presented by Bernardo et al. [55]. The relevant parts of the qualitative theory are produced here. First, a description is provided for autonomous systems. Autonomous systems are further classified into smooth and nonsmooth systems. Nonautonomous systems can similarly be classified as smooth and nonsmooth systems. For autonomous systems, both the continuous time and discrete time representations of a dynamical system are also provided. The discussion presented in this chapter builds the foundation for studying the bifurcation of dynamical systems.

4.1 Smooth Autonomous Dynamical Systems

An autonomous ordinary differential equation is given by

$$\dot{x} \doteq \frac{dx}{dt} = f(x) \tag{4.1}$$

where $f : \mathbb{R}^d \rightarrow \mathbb{R}^d$ is assumed to be continuous. A continuously differentiable function $x : \mathbb{I} \rightarrow \mathbb{R}^d$, where $\mathbb{I} \subset \mathbb{R}$ is an interval, is said to solve Eq. 4.1. The combination of Eq. 4.1 with an initial condition $x(t_0) = x_0$ is called an *initial value problem*, and a solution x of Eq. 4.1 is said to solve this initial value problem if $x(t_0) = x_0$. Assuming global existence and uniqueness of solutions, the solutions form a mapping

$$(t, t_0, x_0) \mapsto x(t, t_0, x_0) \in \mathbb{R}^d \qquad \text{for all} \quad (t, t_0, x_0) \in \mathbb{R} \times \mathbb{R} \times \mathbb{R}^d \tag{4.2}$$

This mapping is called the *general solution* of the differential equation. The solution only depends on the *elapsed time* $t - t_0$ since starting and not separately on the actual time t and the starting time t_0. This can be restated as the solutions being *translation invariant in time.*

4.1.1 Smooth Dynamical Systems

Consider an n–dimensional state space (or phase space) $X \subset \mathbb{R}^n$ and an evolution operator ϕ that takes elements x_0 of the phase space and evolves them through a 'time' t to a state x_t

$$\phi^t : X \to X, \qquad\qquad x_t = \phi^t(x_0) \tag{4.3}$$

The time t takes values in an index set T, which is usually considered to be either discrete (the integers $\mathbb{Z}$) or continuous (the real numbers $\mathbb{R}$).

(*Definition*) A *state space* X, index set T and evolution operator ϕ^t are said to define a *dynamical system* if

$$\phi^0(x) = x, \qquad \text{for all } x \in X \tag{4.4}$$

and,

$$\phi^{t+s}(x) = \phi^s(\phi^t(x)) \qquad \text{for all } x \in X, \quad t, s \in T \tag{4.5}$$

The set of all points $\phi^t(x)$ for all $t \in T$ is called the *trajectory* or *orbit* through the point x. The *phase portrait* of the dynamical system is the partitioning of the state space into orbits. A dynamical system satisfying Eq. 4.4 and Eq. 4.5 is said to be *smooth of index* r, or C^r, if the first r derivatives of ϕ *with respect to* x exist and are continuous at every point $x \in \mathbb{R}$.

An *invariant set* of a dynamical system is a subset $\Lambda \subset X$ such that $x_0 \in \Lambda$ implies $\phi^t(x_0) \in \Lambda$ for all $t \in T$. A system of ODEs can exhibit the following kinds of invariant sets as shown in Fig. 4.1

Equilibria: The simplest form of an invariant set of an ODE is an *equilibrium solution* x^* which satisfies $f(x^*) = 0$. These are also sometimes called *stationary points* of the flow.

Limit cycles: The next most complex kind of invariant set is a *periodic orbit*, which is determined by an initial condition x_p and a period T. Here, T is defined as the smallest time $T > 0$ for which $\phi(x_p, T) = x_p$. Periodic orbits form closed curves in phase space. A periodic orbit that is isolated (does not have any other periodic orbits in its neighborhood) is called a *limit cycle*.

Invariant tori: Invariant tori are the nonlinear equivalent of two–frequency motion. Flow on a torus may be genuinely quasi-periodic in that it contains no periodic orbits, or it may be *phase locked* into containing a stable and an unstable periodic orbit, which wind a given number of times around the torus.

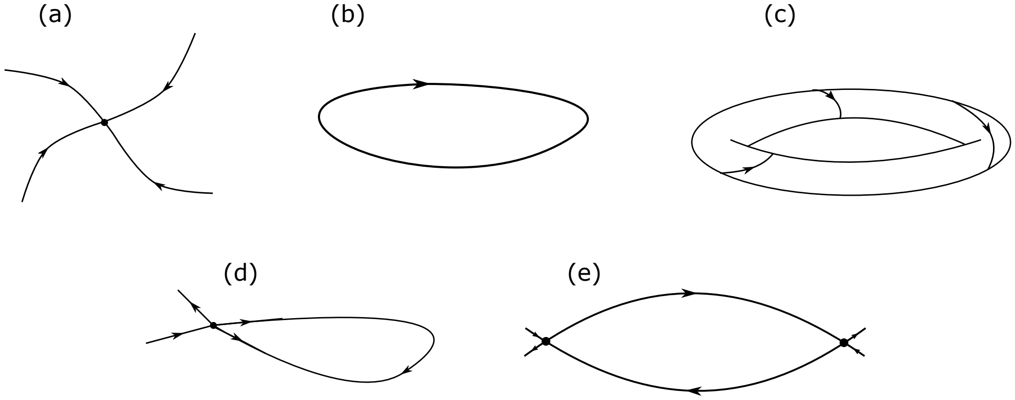

Figure 4.1: Phase portrait of invariant sets of smooth flows : (a) Equilibrium, (b) Limit cycle, (c) Invariant torus, (d) Homoclinic orbit, (e) Heteroclinic orbit.

Homoclinic and Heteroclinic orbits: Another important class of invariant sets are *connecting orbits*, which tend to other invariant sets as time asymptotes to $+\infty$ and to $-\infty$. Consider, for example, orbits that connect equilibria. A *homoclinic orbit* is a trajectory $x(t)$ that connects and equilibrium x^* to itself; $x(t) \to x^*$ as $t \to \pm\infty$. A *heteroclinic orbit* connects two different equiliria x_1^* and x_2^*; $x(t) \to x_1^*$ as $t \to -\infty$ and $x(t) \to x_2^*$ as $t \to +\infty$.

4.1.2 Iterated Maps

Given a *map* defined by the rule

$$x \mapsto f(x), \qquad x \in \mathcal{D} \subset \mathbb{R}^n \tag{4.6}$$

then $T = \mathbb{Z}$; that is, 'time' is integer-valued, and the operator ϕ is just f. Evolving through time $m > 0$ involves taking the mth iterate of the map;

$$\phi^m(x_0) = x_m = f(x_{m-1}) = f(f(x_{m-2})) = ... \doteq f^{(m)}(x_0) \tag{4.7}$$

where a superscript m means m-fold composition

$$f^{(m)}(x_0) = \overbrace{f \circ f \circ ... \circ f(x_0)}^{m\ times} \tag{4.8}$$

A mapping is said to be *invertible* for $x \in \mathcal{D} \subset \mathbb{R}^n$ if given any $x_1 \in \mathcal{D}$ such that $x_1 = f(x_0)$. In such a case, an inverse mapping f^{-1} can be defined by $x_0 = f^{-1}(x_1)$ for all points x_1 in $f(\mathcal{D})$.

The smoothness of the dynamical system in the case of maps is given by the smoothness of the function f. Smooth invertible maps, with smooth inverses are known as *diffeomorphisms.*

Similar to dynamical systems, maps have invariant sets as defined below and shown in Fig. 4.2

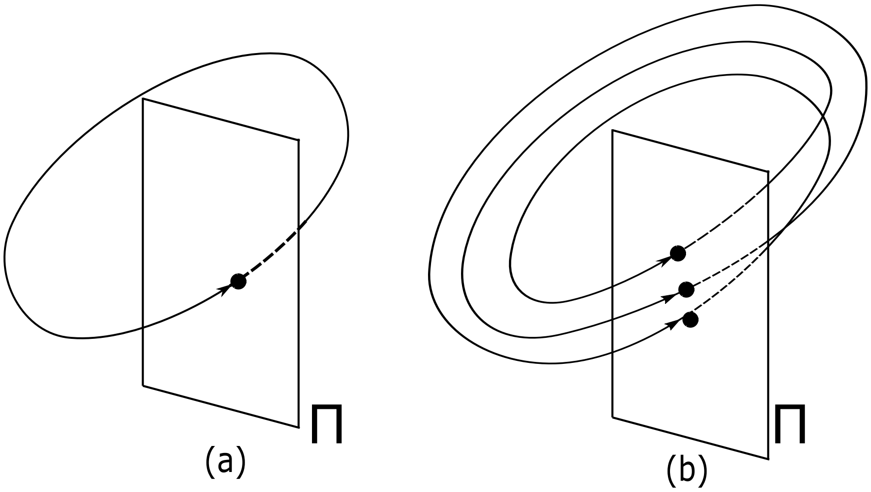

Figure 4.2: Poincare section through phase space mapping $\Pi \rightarrow \Pi$ (a) Fixed point and period–T limit cycle; (b) Period–m points and higher–period limit cycles.

Fixed points: The simplest kind of invariant set of a map is a *fixed point*, which is a point x^* such that $f(x^*) = x^*$. Fixed points of maps have a close connection to periodic orbits, through the induced (Poincaré) map.

Periodic points: Periodic points satisfy $f^m(x^*) = x^*$ for some (least value of) $m > 0$. Such a point is referred to as a *period–m orbit* of the map and its orbit as a period–m orbit.

There exists an important connection between ODEs (flows) and maps. Periodic solutions of ODEs provide a natural way to transform between flows and maps. Consider a limit cycle solution $x(t) = p(t)$ to an ODE of period $T > 0$; that is, $p(t + T) = p(t)$. To study the dynamics near such a cycle, we construct a *Poincaré* *section*, which is an $(n-1)$ dimensional surface Π that contains a point $x_p = p(t^*)$ on the limit cycle and is *transverse* to the flow at x_p. Introducing a notation that

$$\Pi = \{x \in \mathbb{R}^n : \pi(x) = 0\} \tag{4.9}$$

for some smooth scalar function π. Then the transversality condition is that the normal vector $\pi_x(x_p)$ to Π at x_p has a non–zero component in the direction of the $\phi_t(x_p, 0) = f(x_p)$. Here a subscript x or t means differentiation with respect to that variable. That is, we require

$$\pi_x(x_p) f(x_p) \neq 0 \tag{4.10}$$

where a subscript x or t means a partial differentiation with respect to that variable, so that $\pi_x(x_p)$ is the normal vector to Π at $x = x_p$.

Now, we can use the flow ϕ to define a map P from Π to Π, called the *Poincaré map*, which is defined for x sufficiently close to x_p via

$$P(x) = \phi(x, \tau(x)) \tag{4.11}$$

where $\tau(x)$ is defined implicitly as the time closed to T for which

$$\pi(\phi(x, \tau(x))) = 0 \tag{4.12}$$

We can define the Poincaré map as a *smooth projection* S of the time-T map $\phi(\cdot, T)$ for all $x \in \Pi$

$$P(x) = S(\phi(x, T), x) \qquad S(y, x) = \phi(y, \tau(x) - T) \tag{4.13}$$

Thus, x_p becomes a fixed point of the map P. The stability and bifurcations of the periodic solutions can be studied by the linearization P_x of the Poincaré map at x_p.

A benefit of studying Poincaré maps rather than flows is that they drop by one dimension of the sets we need to consider. This results in a significant simplification as only the discrete points on the Poincaré map need to be tracked instead of tracking the evolution of the system continuously. Thus, limit cycles of flows correspond to isolated fixed points of Poincaré maps; invariant tori correspond to closed curves of the map; and chaotic invariant sets decrease their fractal dimension by one.

4.2 Nonsmooth Autonomous Dynamical Systems

This section begins the systematic study of the dynamics of nonsmooth systems. Three different classes of piecewise-smooth systems: *maps, flows* and *hybrid systems* will be introduced. A complete theory for existence and uniqueness of solutions does not exist for these broad classes of system.

4.2.1 Piecewise-Smooth Dynamical Systems

A *piecewise-smooth flow* is given by a finite set of ODEs

$$\dot{x} = F_i(x, \mu), \qquad \text{for} \quad x \in S_i \tag{4.14}$$

where $\cup_i S_i = \mathcal{D} \subset \mathbb{R}^n$ and each S_i has a non-empty interior. The intersection $\Sigma_{ij} := (\overline{S}_i \cap \overline{S}_j)$ is either an $\mathbb{R}^{(n-1)}$-dimensional manifold included in the boundaries ∂S_j and ∂S_i, or is the empty set. Each vector field F_i is smooth in both the state x and the parameter μ, and defines a smooth flow $\Phi_i(x, t)$ within any open set $U \supset S_i$. In particular, each flow Φ_i is well defined on both sides of the boundary ∂S_j.

A non-empty border between the two regions Σ_{ij} will be called a *discontinuity set, discontinuity boundary*, or sometimes, a *switching manifold*. The definition of a piecewise-smooth flow does not uniquely specify a rule for the evolution of the dynamics within a discontinuity set. One possibility is to assign each Σ_{ij} as belonging to a single region $\overline{S}_i$ only. That is, F_i rather than F_j applies on Σ_{ij}. In fact, such notions make little difference except in the case where the flow becomes confined to the boundary.

The *degree of smoothness* at a point x_0 in a switching set Σ_{ij} of a piecewise-smooth ODE is the highest order r such that the Taylor series expansion of $\Phi_i(x_0,t)$ and $\Phi_j(x_0,t)$ with respect to t, evaluated at $t=0$, agree up to terms of $O(t^{r-1})$. That is, the first non-zero partial derivative with respect to t of the difference $[\Phi_i(x_0,t) - \Phi_j(x_0,t)]|_{t=0}$ is of the order r. Unlike order of singularity for piecewise-smooth maps, the degree of smoothness cannot be a non-integer.

4.2.2 Piecewise-Smooth Maps

A *piecewise-smooth map* is described by a finite set of smooth maps

$$x \mapsto F_i(x,\mu), \qquad \text{for} \quad x \in S_i \tag{4.15}$$

where $\cup_i S_i = \mathcal{D} \subset \mathbb{R}^n$ and each S_i has a non–empty interior. The intersection Σ_{ij} between the closure (set plus its boundary) of the sets S_i and S_j that is $\Sigma_{ij} := \overline{S}_i \cap \overline{S}_j$ is either an $\mathbb{R}^{(n-1)}$-dimensional manifold included in the boundaries ∂S_j and ∂S_i, or is the empty set. Each function F_i is smooth in both the state x and the parameter μ for any open subset U of S_i.

A set Σ_{ij} for a piecewise-smooth map is usually termed a *border* or *discontinuity boundary* that separates the regions of phase space where different smooth maps apply. The above definition allows for the possibility for one of the component maps F_i may itself be nonsmooth at the boundary Σ_{ij}. Cases that have $F_i \neq F_j$ along Σ_{ij}, so that the map has a jump in the state are known as dicontinuous piecewise-smooth

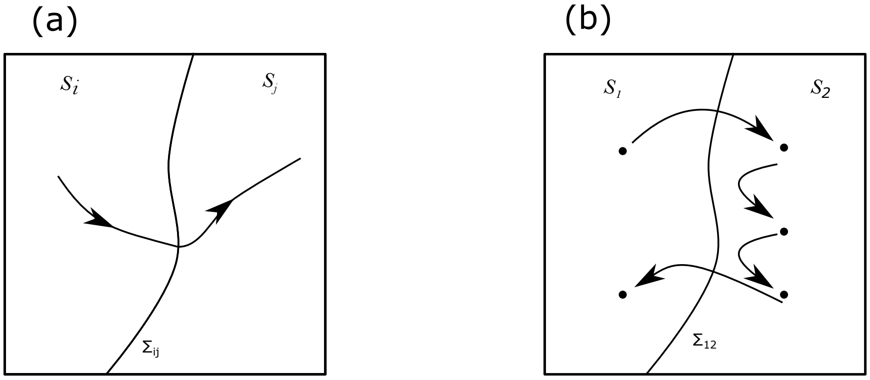

Figure 4.3: Schematic illustrating trajectories of: (a) Piecewise-smooth flow (b) Piecewise-smooth map.

maps and are also included. In this case, a number of choices can be made about the value of the map for points in Σ_{ij}; for example, taking the average of F_i and F_j; or allowing the map to be set valued at this point, taking all possible convex combinations $\{F_i + \lambda(F_j - F_i) : 0 \leq \lambda \leq 1\}$. In practice, such choices make little practical difference to the dynamics of the map, since they describe what happens to a set of points of zero measure.

The *order of singularity* of a point $\hat{x} \in \Sigma_{ij}$ of a continuous piecewise-smooth map is the order of the first non-zero term in the formal power-series expansion of $F_1(x) - F_2(x)$ about $x = \hat{x}$. The order of singularity for a piecewise-smooth map can be non-integer. Figure 4.3 shows the difference between the trajectories of a piecewise-smooth flow and a piecewise-smooth map.

4.3 Nonautonomous Dynamical Systems

Consider an initial value prolem in $\mathbb{R}^d$,

$$\dot{x} = f(t, x), \qquad x(t_0) = x_0 \tag{4.16}$$

In contrast to the autonomous case, the solutions may now depend separately on the actual time t and the starting time t_0 rather than only on the elapsed time $t - t_0$ since starting. Assuming global existence and uniqueness of solutions in forward time, the solutions form a continuous mapping $(t, t_0, x_0) \mapsto x(t, t_0, x_0) \in \mathbb{R}^d \quad$ for $t \geq t_0$ with $t, t_0 \in \mathbb{R}$ and $x_0 \in \mathbb{R}^d$ fulfilling the initial value and evolution properties

- $x(t, t_0, x_0) = x_0$ for all $t_0 \in \mathbb{R}$ and $x_0 \in \mathbb{R}^d$
- $x(t_2, t_0, x_0) = x(t_2, t_1, x(t_1, t_0, x_0))$ for all $t_0 \leq t_1 \leq t_2$ and $x_0 \in \mathbb{R}^d$

The evolution property is a consequence of the causality principle that the solutions are determined uniquely by their initial values for the given differential equation. Figure 4.4 shows the phase space of a periodically forced dynamical system.

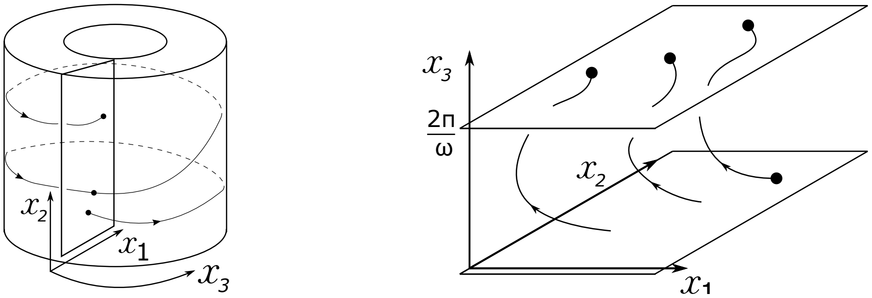

Figure 4.4: Schematic description of cylindrical phase space associated with periodically forced system.

The concepts introduced in this chapter form the foundation for studying dynamical systems and their bifurcations. The next chapter discusses the concept of bifurcation and how the concept differs for autonomous system and nonautonomous systems. Later, the equations required to study bifurcations are derived and the implementation of the algorithm for the derived equations in MATLAB is discussed.

CHAPTER 5

BIFURCATION ANALYSIS OF NONLINEAR DYNAMICAL SYSTEMS

Most dynamical systems can be described using ordinary differential equations. In general, these systems have nonlinear characteristics and include many parameters. Small changes in the values of these parameters can sometimes result in large qualitative changes in the system performance. Therefore, determining a way to analyze such systems is critical. As is well known, the solution to most nonlinear dynamical systems cannot be obtained analytically [56, 57]. This means we must conduct multiple numerical simulations using the different fixed sets of parameter values and initial conditions. However, each of these simulations can only provide information about one stable solution at a time, and they tend to take a long time to reach a solution. This approach is not very suitable for studying the dynamical system for a large range of parameter values.

The topological properties of the solutions of a dynamical system may change when a parameter of the system changes slightly. This process is known as *bifurcation*. Examples of bifurcation phenomena include a transition from a stable equilibrium state to an oscillating motion or from a regular oscillation to a chaotic state. Bifurcation analysis enables us to identify the range of a parameter over which a system behaves in a stable manner, the total behavior of the solution in general, and the transition mechanism of the dynamic responses. A set of parameter values that cause bifurcations is called a bifurcation set, and a graph of these sets is called a bifurcation diagram.

5.1 Basic Theory of Bifurcation Analysis

Consider the following autonomous system

$$\frac{dx}{dt} = f_a(x, \lambda) \tag{5.1}$$

and its forced system, that is, a nonautonomous system

$$\frac{dx}{dt} = f(t, x, \lambda) \tag{5.2}$$

where $t \in \mathbb{R}$ denotes time, $x \in \mathbb{R}^n$ is a vector consisting of state variables, and $\lambda \in \mathbb{R}^l$ denotes the system parameters. Assume that both f_a and f from above equations are sufficiently differentiable, i.e., C^∞-class functions. In addition, also assume that the function f is periodic in τ_p so that $f(t + \tau_p, x, \lambda) = f(t, x, \lambda)$, for all t. We shall also assume that a solution to Eq. 5.1 or 5.2 with the initial condition $x = x_0$ at $t = t_0$ is described by $x(t) = \varphi(t, x_0)$, for all t, or $x(t) = \varphi(t, \lambda; t_o, x_0)$.

5.1.1 Equilibrium Point and Variational Equation in Autonomous System

Autonomous systems were introduced in Chapter 4. Let us briefly review the case of autonomous systems following Eq. 5.1. By imposing the condition

$$f_a(x, \lambda) = 0 \tag{5.3}$$

one can compute the locations of equilibrium points in the system. Any point x^* satisfying Eq. 5.3 is known as an equilibrium point.

The Taylor expansion of f_a in Eq. 5.1 about the equilibrium point by setting $x = x^*+\xi$ can be described by

$$\frac{d(x^* + \xi)}{dt} = f_a(x^* + \xi) = f_a(x^*) + \left.\frac{\partial f_a(x)}{dx}\right|_{x=x^*} \xi + ..., \tag{5.4}$$

where ξ is a small perturbation. By subtracting this equation from Eq. 5.1, we obtain a *variational equation* with respect to ξ:

$$\frac{d\xi}{dt} = \left.\frac{\partial f_a(x)}{dx}\right|_{x=x^*} \xi = \frac{\partial f_a(x^*)}{dx}\xi \equiv J_c\xi \tag{5.5}$$

Suppose that the eigenvalues μ_i, i=1,2,....,n, are the roots of the characteristic equation for this $n \times n$ Jacobian matrix J_c, and they determine the stability of the equilibrium point. For simplicity, assume that all eigenvalues are real and distinct, and the correspoinding eigenvectors, v_i, for i=1,2,...,n, can be obtained. The general solution of the variational equation can be written as

$$\xi(t) = \sum_{i=1}^{n} c_i e^{\mu_i t} v_i \tag{5.6}$$

where c_i is a constant related to the inital values of the state variables. We know that this general solution is stable if and only if all the eigenvalues are negative. Thus, the eigenvalues of the Jacobian matrix, J_c present a stability index for the given equilibrium point in a continuous-time autonomous system in the neighborhood of the equilibrium point. Here, x^* is known as a hyperbolic equilibrium point, if the real parts of all eigenvalues are non-zero. A bifurcation occurs when an equilibrium point loses its hyperbolicity as a result of variation of the system parameters.

Typical bifurcations of the equilibrium point are

- *Hopf bifurcation*: A couple of complex conjugate eigenvalues of the characteristic equation become pure imaginary numbers. An oscillatory solution appears as a result of changing the value of a parameter.
- *Saddle-node bifurcation*: One of the eigenvalues is zero. A pair of equilibrium points appear when the value of a parameter is changed.

If a very small perturbation is added to an autonomous system, a periodic solution will appear around the equilibrium point, and it will inherit the stability of the equilibrium. Mathematically, adding a small perturbation to an autonomous system leads to the disappearance of all equilibrium points since $dx/dt \neq 0$ for all t.

5.1.2 Periodic Solutions and Fixed Points of a Nonautonomous System

The periodic solutions of a nonautonomous system such as one described by Eq. 5.2 can be qualitatively studied by using a Poincaré map.

5.1.2.1 Poincaré Mapping and Fixed Points

Assume that the solution to Eq. 5.2 starting from $x = x_0$ at $t = 0$ is given by

$$x(t) = \varphi(t, \lambda; t_0, x_0) \tag{5.7}$$

Thus, the solution is also periodic in τ_p because of the periodicity of f in Eq. 5.2, i.e., $\varphi(t + \tau_p, \lambda; t_0, x_0) = \varphi(t, \lambda; t_0, x_0)$. We can define the corresponding map:

$$\begin{aligned} P_\lambda : \mathbb{R}^n &\to \mathbb{R}^n \\ x_0 &\mapsto P_\lambda(x_0) = \varphi(t + \tau_p, \lambda; t_0, x_0) \end{aligned} \tag{5.8}$$

This map is a sampling of the orbit every τ_p. Therefore, we get

$$x_0, P_\lambda(x_0), P_\lambda^2(x_0), ..., P_\lambda^m(x_0), ... \tag{5.9}$$

We call this P_λ as the Poincaré mapping. Note that the system described using a differential equation in Eq. 5.2 has been converted into a difference equation given by

$$x^{(k+1)} = P_\lambda\Big(x^{(k)}\Big) \tag{5.10}$$

for k=0,1,2... If an initial state, $x_0 \in \mathbb{R}^n$, satisfies the following relationship

$$x_0 = P_\lambda(x_0) \tag{5.11}$$

then this point is called a *fixed point*, Also, if for some $m \neq 1$,

$$x_0 = P_\lambda^m(x_0) \tag{5.12}$$

and if all $P_\lambda^k(x_0)$, k= 0, 1,..., m-1, are different, x_0 is called an *m-periodic point*. This results in a one–to–one correspondence between the periodic solution of the nonautonomous differential equation and the fixed point of the Poincaré map P_λ. The case for an m-periodic point can also be studied by replacing P_λ by P_λ^m, or the mth iterate of P_λ. In general, only a limited number of continuous dynamical systems have an explicit form of P_λ. However, it is relatively easier to obtain the Poincaré mapping.

5.2 Jacobian Matrix of the System Using Poincaré Sections

A Poincaré map is created by using the intersection of a periodic orbit in the n-dimensional state space of the dynamical system with a n-1-dimensional subspace called the Poincaré section. While considering a system with discontinuous characteristics, the Poincaré sections are usually defined at the break points using the condition of discontinuity. On the other hand, for smooth nonautonomous systems, a Poincaré sections is defined using time since the periodicity of the solutions matches the frequency of the external, applied force. For this study, the Poincaré section of the nonsmooth, nonautonomous system is defined with time.

Consider the system defined earlier as described by nonautonomous differential equations

$$\boldsymbol{x} = (x_1, \ldots, x_n)^\top \in \boldsymbol{R}^n, \tag{5.13}$$

$$\frac{d\boldsymbol{x}}{dt} = \boldsymbol{f}_i(t, \boldsymbol{x}), \qquad i = 0, \ldots, m-1, \tag{5.14}$$

where $t \in \boldsymbol{S}^1$ is the time with $\boldsymbol{S}^1 = \{t \in \boldsymbol{R}\ mod\ \tau\},\ \tau \in \boldsymbol{R}$, which is $2\pi/\omega$ and is a parameter to determine the initial Poincaré section Π_0, $\boldsymbol{x} \in \boldsymbol{R}^n$ is the state of the system and $\boldsymbol{f}_i : \boldsymbol{R}^n \to \boldsymbol{R}^n$ is a C^∞ function. It is assumed that a periodic solution of the dynamical system exists, the solution orbit crosses Π_i in a transversal manner and $\boldsymbol{x}_0 = \boldsymbol{x}(0) \in \Pi_0$. The solution of Eq. 5.14 is given by

$$\boldsymbol{x}(t) = \boldsymbol{\varphi}(t, \boldsymbol{x}_0) \tag{5.15}$$

The solutions arising from each $\boldsymbol{f}_i$ are given by $\boldsymbol{\varphi}_i(t, \boldsymbol{x}_i, t_i)$. The initial time of the solution is given by t_i . The local sections Π_i are defined as

$$\Pi_i = \{t \in \boldsymbol{S}^1, \boldsymbol{x} \in \boldsymbol{R}^n | \alpha_i(t, \boldsymbol{x}, \kappa_i) = 0\} \tag{5.16}$$

where α_i is a differentiable function and κ_i is a parameter used to uniquely define the positions of the Poincaré sections Π_i. In addition, for a nonautonomous system,

$$\Pi_0 = \{t \in \boldsymbol{S}^1, \boldsymbol{x} \in \boldsymbol{R}^n | \alpha_0(t, \boldsymbol{x}, \tau) = t = 0\} \tag{5.17}$$

When a solution orbit dictated by $\boldsymbol{f}_i$ arrives at Π_{i+1}, the function that governs the solution is reset to $\boldsymbol{f}_{i+1}$ as shown in Fig. 5.1(a). If the solution orbit crossing through multiple Poincaré sections finally reaches the initial Π_0 section again, then the sub maps can be defined as

$$\begin{aligned}
H_0 \quad &: \quad \Pi_0 \rightarrow \Pi_1 \\
& \quad\quad \boldsymbol{x}_0 \mapsto \boldsymbol{x}_1 = \boldsymbol{\varphi}_0(t_1, \boldsymbol{x}_0, t_0 = 0) \\
H_1 \quad &: \quad \Pi_1 \rightarrow \Pi_2 \\
& \quad\quad \boldsymbol{x}_1 \mapsto \boldsymbol{x}_2 = \boldsymbol{\varphi}_1(t_2, \boldsymbol{x}_1, t_1) \\
& \quad\quad \vdots \\
H_{m-1} \quad &: \quad \Pi_{m-1} \rightarrow \Pi_0 \\
& \quad\quad \boldsymbol{x}_{m-1} \mapsto \boldsymbol{x}_m = \boldsymbol{\varphi}_{m-1}(t_m, \boldsymbol{x}_{m-1}, t_{m-1})
\end{aligned} \tag{5.18}$$

The above set of equations describe the $m-1$ maps corresponding to Eq. 5.14. All H_i 's are the submaps from a given Poincaré section Π_i to the next Poincaré section Π_{i+1}. Similarly, all $\boldsymbol{x}_i \mapsto \boldsymbol{x}_{i+1}$ are maps from a given Poincaré section Π_i to the next Poincaré section Π_{i+1}. All the solution orbits $\boldsymbol{\varphi}_i(t_{i+1}, \boldsymbol{x}_i, t_i)$ represent a solution starting from $(\boldsymbol{x}_i, t_i)$ and ending at time t_{i+1}. From Eq. 5.18, the composite Poincaré map H can be defined as

$$H(\boldsymbol{x}(k), \tau, \kappa, ..., \kappa_{m-1}) = H_{m-1} \circ ... \circ H_1 \circ H_0 \tag{5.19}$$

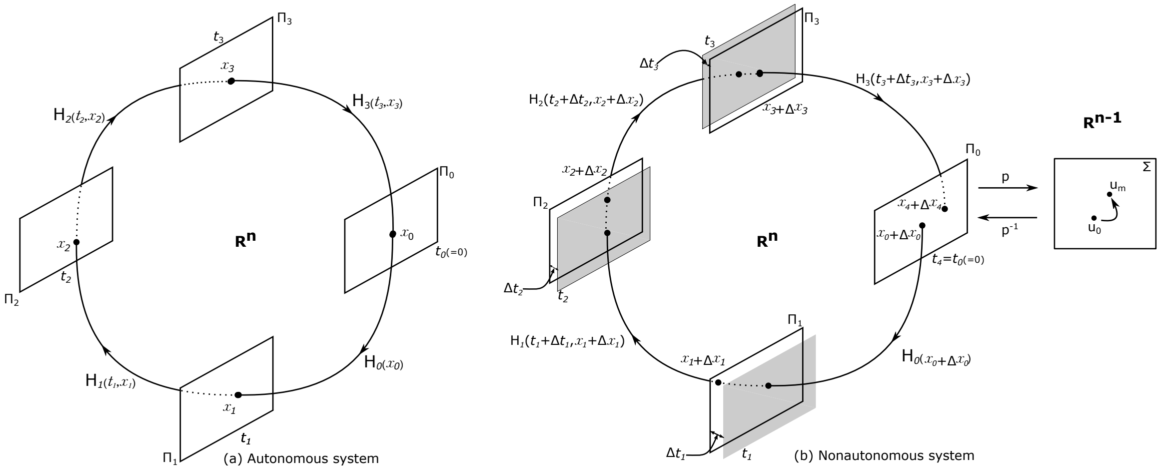

(a) Autonomous system

(b) Nonautonomous system

Figure 5.1: Schematic describing how $\Delta \boldsymbol{x}_0$ influences the collision time for non–autonomous systems with breaks.

When the orbit starting from $\boldsymbol{x}_0 \in \Pi_0$ returns to the initial point $\boldsymbol{x}_0$, the solution results in a periodic orbit and the corresponding fixed point of the Poincaré map H is written as follows

$$\boldsymbol{x}_0 = H(\boldsymbol{x}_0, \tau, \kappa, ..., \kappa_{m-1}) \tag{5.20}$$

The derivative with the initial value of the Poincaré map is given by

$$\frac{\partial H}{\partial \boldsymbol{x}_0} = \prod_{i=0}^{m-1} \frac{\partial H_{m-1-i}}{\partial \boldsymbol{x}_{m-1-i}} \Bigg|_{t_{m-1-i}}^{t_{m-i}} \tag{5.21}$$

However, for nonsmooth, nonautonomous systems, the Jacobian calculated by Eq. 5.21 is known to give incorrect numerical results [58]. To investigate the cause for this error, Miino et al. studied the relation of the map H with the time t, and of the time t with initial value $\boldsymbol{x}_0$ for a nonsmooth, nonautonomous system. For an autonomous system with nonsmooth characteristics, $\partial H/\partial \boldsymbol{x}_0 = (\partial H_1/\partial \boldsymbol{x}_1)\cdot(\partial H_0/\partial \boldsymbol{x}_0)$ is satisfied because it is assumed that the map H_1 is dependent on the initial value $\boldsymbol{x}_1$ only. Therefore, the map is defined as $H_1(\boldsymbol{x}_1) = \boldsymbol{x}_2$.

For nonautonomous systems, the initial time t_1 also influences the map H_1 as shown in Eq. 5.18 and the map is defined as $H_1(t_1, \boldsymbol{x}_1) = \boldsymbol{x}_2$. In Fig. 5.1(b), $\Delta\boldsymbol{x}_0$ is an infinitesimal difference of $\boldsymbol{x}_0$, which causes infinitesimal differences $\Delta\boldsymbol{x}_1$ and Δt_1 in $\boldsymbol{x}_1$ and t_1 on Π_1 and so on. Hence, it is observed from Fig. 5.1(b) that an infinitesimal difference of $\boldsymbol{x}_0$ affects $\boldsymbol{x}_3$ via affecting t_1, $\boldsymbol{x}_1$, t_2 and $\boldsymbol{x}_2$ and so on. To solve this problem, Miino et al. [58] proposed a solution to regard the time t as a state variable and define the system by

$$\boldsymbol{y} = (x_0, \ldots, x_{n-1}, t)^\top \in \boldsymbol{R}^n \times \boldsymbol{S}^1, \tag{5.22}$$

$$\frac{d\boldsymbol{y}}{dt} = \begin{pmatrix} \boldsymbol{f}_i(t, \boldsymbol{x}) \\ 1 \end{pmatrix} = \boldsymbol{g}_i(\boldsymbol{y}), \quad i = 0, \ldots, m-1, \tag{5.23}$$

For the new system, each submap H' is defined as

$$\begin{aligned}
H'_0 \quad &: \quad \Pi'_0 \to \Pi'_1 \\
&\quad\ \boldsymbol{y}_0 \mapsto \boldsymbol{y}_1 = \boldsymbol{\Phi}_0(t_1, \boldsymbol{y}_0) \\
H'_1 \quad &: \quad \Pi'_1 \to \Pi'_2 \\
&\quad\ \boldsymbol{y}_1 \mapsto \boldsymbol{y}_2 = \boldsymbol{\Phi}_1(t_2, \boldsymbol{y}_1) \\
&\quad\ \ \vdots \\
H'_{m-1} \quad &: \quad \Pi'_{m-1} \to \Pi'_0 \\
&\quad\ \boldsymbol{y}_{m-1} \mapsto \boldsymbol{y}_m = \boldsymbol{\Phi}_{m-1}(t_m, \boldsymbol{y}_{m-1})
\end{aligned} \tag{5.24}$$

Define a coordinate system $u \in \Sigma \subset \boldsymbol{R}^{n-1}$ by using a projection p and embedding map p^{-1} as shown in Fig. 5.1(b) and described by:

$$p : \Pi_0 \to \Sigma \qquad p^{-1} : \Sigma \to \Pi_0 \tag{5.25}$$

The Poincaré map on the local coordinate is a mapping defined by

$$\begin{aligned} H_l : \quad & \Sigma \to \Sigma \\ & \boldsymbol{u} \mapsto p \circ H \circ p^{-1}(u) \end{aligned} \tag{5.26}$$

Therefore,

$$p^{-1}(\boldsymbol{u}) = \boldsymbol{y} = (x_0, ..., x_{n-1}, 0)^\top \tag{5.27}$$

$$p(\boldsymbol{y}) = \boldsymbol{u} = (x_0, ..., x_{n-1})^\top \tag{5.28}$$

$$\frac{\partial p^{-1}}{\partial \boldsymbol{u}} = \begin{pmatrix} 1 & 0 & \dots & 0 \\ 0 & 1 & \dots & 0 \\ \vdots & & \ddots & \vdots \\ 0 & 0 & \dots & 1 \\ 0 & 0 & \dots & 0 \end{pmatrix} \tag{5.29}$$

$$\frac{\partial p}{\partial \boldsymbol{y}} = \begin{pmatrix} 1 & 0 & \dots & 0 & 0 \\ 0 & 1 & \dots & 0 & 0 \\ \vdots & & \ddots & & \vdots \\ 0 & 0 & \dots & 1 & 0 \end{pmatrix}$$

From Eq. 5.24, the Poincaré map H can be described as

$$H(\boldsymbol{x}(k), \tau, \kappa, ..., \kappa_{m-1}) = p \circ H'_{m-1} \circ ... \circ H'_1 \circ H'_0 \circ p^{-1} \tag{5.30}$$

Since each submap H'_i depends on the state $\boldsymbol{y}_0$ only as the state $\boldsymbol{y}_0$ includes the time t, the Poincaré map can be used to calculate the correct Jacobian matrix at the initial map point $\boldsymbol{x}_0$ and is given by

$$\frac{\partial H(\boldsymbol{x}_0)}{\partial \boldsymbol{x}_0} = \frac{\partial p}{\partial \boldsymbol{y}} \left(\prod_{i=0}^{m-1} \frac{\partial H'_{m-1-i}}{\partial \boldsymbol{y}_{m-1-i}} \right) \frac{\partial p^{-1}}{\partial \boldsymbol{u}_0} \tag{5.31}$$

For the PDE–LPG coupled system with PDE thrust given by Eq. 2.6

$$\frac{\partial H(\boldsymbol{x}_0)}{\partial \boldsymbol{x}_0} = \frac{\partial p}{\partial \boldsymbol{y}} . \frac{\partial H'_2}{\partial \boldsymbol{y}_2} . \frac{\partial H'_1}{\partial \boldsymbol{y}_1} . \frac{\partial H'_0}{\partial \boldsymbol{y}_0} . \frac{\partial p^{-1}}{\partial \boldsymbol{u}_0} \tag{5.32}$$

To find the derivatives in Eq. 5.32, it is required to take into account the derivative of the boundary colliding time [59]. For example, if the solution orbit reaches boundary at time ϵ, then the derivative can be found as

$$\frac{\partial H'_0}{\partial y_0} = \frac{\partial y(\epsilon)}{\partial y_0} + \frac{\partial y}{\partial t} \frac{\partial \epsilon}{\partial y_0} = \frac{\partial y(\epsilon)}{\partial y_0} + g(y(\epsilon)) \frac{\partial \epsilon}{\partial y_0} \tag{5.33}$$

The term $\partial \epsilon / \partial y_0$ vanishes if the map H'_0 relies on time. Using the procedure shown in [59, 60] and Eq. 5.33, the Jacobian using Eq. 5.32 can be calculated.

For the system parameters defined earlier and PDE operating frequency of 3.75 Hz,

$$\frac{\partial p}{\partial \boldsymbol{y}} = \begin{pmatrix} 1 & 0 & 0 \\ 0 & 1 & 0 \end{pmatrix}$$

$$\frac{\partial H_2'}{\partial \boldsymbol{y}_2} = \begin{pmatrix} 0.2502 & 0.0064 & 0 \\ 14.6587 & 0.3736 & 0 \\ 0 & 0 & 1 \end{pmatrix}$$

$$\frac{\partial H_1'}{\partial \boldsymbol{y}_1} = \begin{pmatrix} 0.8948 & 0.0078 & 0 \\ -42.42 & 0.6426 & 0 \\ 0 & 0 & 1 \end{pmatrix} \tag{5.34}$$

$$\frac{\partial H_0'}{\partial \boldsymbol{y}_0} = \begin{pmatrix} 1 & 0.0002 & 0 \\ 0.1893 & 0.9997 & 0 \\ 0 & 0 & 1 \end{pmatrix}$$

$$\frac{\partial p^{-1}}{\partial \boldsymbol{u}_0} = \begin{pmatrix} 1 & 0 \\ 0 & 1 \\ 0 & 0 \end{pmatrix}$$

Therefore,

$$\frac{\partial H(\boldsymbol{x}_0)}{\partial \boldsymbol{x}_0} = \begin{pmatrix} -0.04618 & 0.0060 \\ -2.705 & 0.3526 \end{pmatrix} \tag{5.35}$$

Let λ be the eigenvalues of the Jacobian matrix as calculated using Eq. 5.32. For a nonsingular Jacobian matrix of a dynamical system, all the eigenvalues will be non–zero and Lyapunov exponents can be calculated using methods such as QR decomposition. Lyapunov exponents can then be used to determine the stability of the system. In case of a singular system, methods such as QR decomposition cannot be used since the matrix will be non–invertible and the decomposition will not be unique. However, a dynamical system with a singular Jacobian matrix represents a system with non-hyperbolic equilibrium. Such systems are not structurally stable and small perturbations can result in local bifurcations of the non-hyperbolic equilibrium. Such equilibria are sometimes referred to as being critical. Their stability cannot be determined directly from the signs of the eigenvalues of the Jacobian matrix and depends on the nonlinear term present in the differential equation describing the system. The eigenvalues of the Jacobian matrix given by Eq. 5.35 are

$$\lambda_{3.75Hz} = \begin{pmatrix} 0 \\ 0.3064 \end{pmatrix} \tag{5.36}$$

For the coupled PDE-LPG nonsmooth, nonautonomous system, it was observed that for all PDE operating frequencies, one eigenvalue is always zero as shown in Fig. 5.2. This results in a singular Jacobian matrix as calculated using a composite Poincaré map.

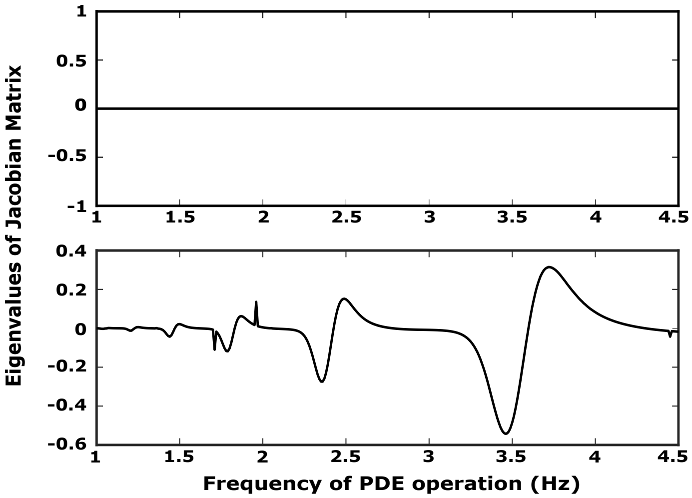

Figure 5.2: Eigenvalues of the Jacobian matrix at different PDE operating frequencies.

5.2.1 Stability of a Fixed Point in Difference Equation

Let us consider a stability index for difference equations. Equation 5.8 forms a discrete dynamical system given by the difference equation

$$z^{(k+1)} = W\left(z^{(k)}\right), \quad k = 0, 1, 2, ... \tag{5.37}$$

If ζ^* is a fixed point for the discrete dynamical system,

$$\zeta^* - W(\zeta^*) = 0 \tag{5.38}$$

As a similar discussion from the previous section, let $\eta^{(k)} \in \mathbb{R}^n$ be a small perturbation away from the fixed point ζ^* satisfying Eq. 5.38. For a small ϵ, we can assume that $\|\eta^{(k)}\| < \epsilon$, where $\|\cdot\|$ is the Euclidean norm. If the variation around the fixed point is defined as $z^{(k)} = \zeta^* + \eta^{(k)}$, the difference equation of Eq. 5.37 is

$$z^{(k+1)} = \zeta^* + \eta^{(k+1)} = W\left(\zeta^* + \eta^{(k)}\right) \tag{5.39}$$

A Taylor expansion gives

$$\zeta^* + \eta^{(k+1)} = W(\zeta^*) + \left.\frac{\partial W}{\partial z}\right|_{z=\zeta^*} \eta^{(k)} + ... \tag{5.40}$$

The following linear difference equation is obtained by neglecting the high–order terms and subtracting Eq. 5.40 from Eq. 5.38

$$\eta^{(k+1)} = \left.\frac{\partial W}{\partial z}\right|_{z=\zeta^*} \eta^{(k)} = \frac{\partial W(\zeta^*)}{\partial z}\eta^{(k)} \equiv J_d \; \eta^{(k)} \tag{5.41}$$

where J_d is an $n \times n$ Jacobian matrix and its elements are derivatives of the solution with respect to the state variables. The eigenvalue problem for a difference equation is formulated as

$$J_d v_i = \mu_i v_i \tag{5.42}$$

for i=1, 2,..., n. In general, this equation has n–tuple non–zero vectors v_i, i= 1, 2, ..., n. μ_i and the corresponding v_i are known as a *multiplier* and *eigenvector* of the difference equation given by Eq. 5.41, respectively. The multipliers are computed from the following characteristic equation

$$det(J_d - \mu_i I) = 0 \tag{5.43}$$

The solution at time k to the linear difference equation given Eq. 5.41 can be expressed as a linear combination of constants, multipliers, and eigenvectors as

$$\begin{aligned} \eta^{(k)} &= \sum_{i=1}^{n} c_i \mu_i^k v_i \\ &= c_1 \mu_1^k v_1 + c_2 \mu_2^k v_2 + ... + c_n \mu_n^k v_n \end{aligned} \tag{5.44}$$

To prevent an explosion in the magnitude of the vector $\eta^{(k)}$, all absolute values of μ_i should be less than unity.

Let us go back to the Poincaré mapping P_λ. It generates a sequence given by

$$x^{(1)} = P_\lambda(x_0),\ x^{(2)} = P_\lambda(x^{(1)}),\ ..., x^{(k+1)} = P_\lambda(x^{(k)}), ... \tag{5.45}$$

From the linearity of variational equation defined earlier, the characteristic equation can be written as

$$\det\left(\frac{\partial P_\lambda(x^*)}{\partial x} - \mu_i I\right) = 0 \tag{5.46}$$

where x^* is a fixed point. If all the absolute values of the multipliers are different from unity, x^* is known as a hyperbolic fixed point of P_λ. For a two–dimensional discrete system, Table 5.1 shows the topological classification of hyperbolic fixed points.

Table 5.1: Topological classification based on characteristic multipliers [7].

Name	Topological property	Condition
sink	completely stable	$\|\mu_1\| < 1,\ \|\mu_2\| < 1$
source	completely unstable	$\|\mu_1\| > 1,\ \|\mu_2 > 1$
saddle	direct–type unstable	$0 < \mu_1 < 1 < \mu_2$
saddle	inverse–type unstable	$\mu_1 < -1 < \mu_2 < 0$

5.2.1.1 Bifurcation of Periodic Solution

There are three main kinds of local bifurcations of periodic solutions. Figure 5.3 shows the location of multipliers on the complex plane and their relation to the type of bifurcation.

- *Tangent bifurcation* (or saddle–node bifurcation or fold bifurcation of periodic solution): This type of bifurcation causes a pair of a node and a saddle to emerge

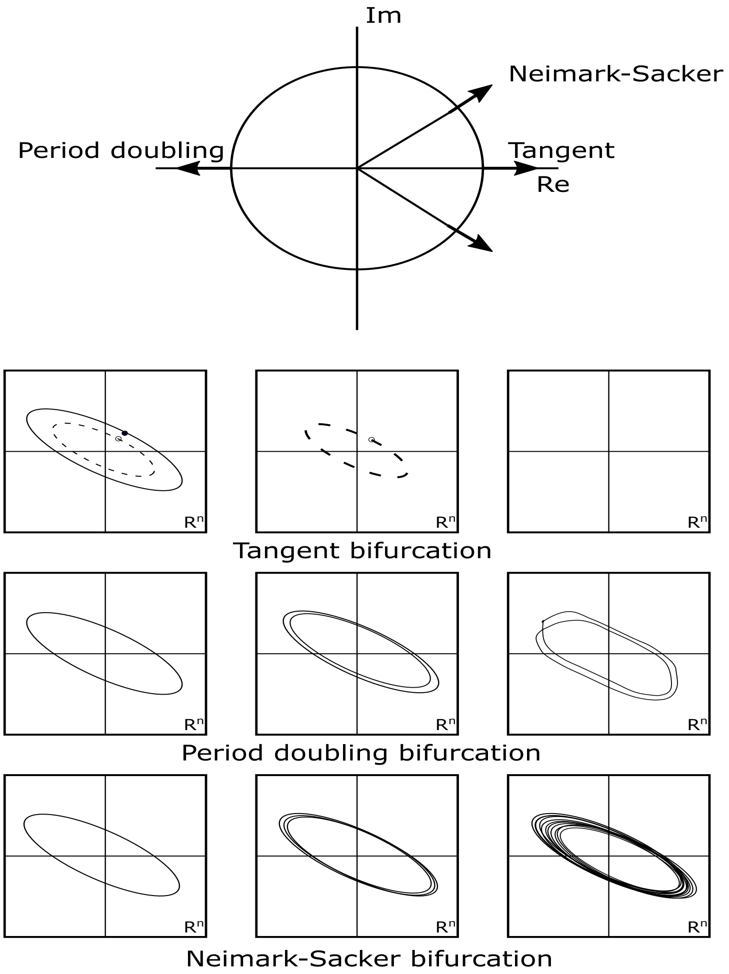

Figure 5.3: Location of multipliers on the complex plane and types of bifurcations of a periodic solution.

or disappear. At a particular parameter value $\lambda = \lambda^*$, one of the multipliers of the characteristic equations satisfies the condition μ_i=1.

- *Period–doubling bifurcation* (or flip bifurcation): This type of bifurcation occurs when a real multiplier passes through a point (-1,0) in the complex plane, i.e., $\mu_i = -1$. If an inverse–type saddle takes this value of the multiplier, its stability changes. As a side effect, two–periodic points are generated around the fixed point. In general, the period doubles and none of the fixed points disappear.

- *Neimark–Sacker bifurcation* (or Hopf bifurcation): Similar to Hopf bifurcation of an equilibrium point, the fixed point becomes unstable, and an invariant closed curve, which corresponds to quasi–periodic solution of the original periodic nonautonomous system, may appear in the Poincaré map. This type of bifurcation occurs when a pair of multipliers pass transversely through points of unit circle except for 0 and π.

5.3 Method of Numerical Computation

Newton's method is used to accomplish the task of obtaining bifurcation sets and to compute accurate locations of equilibrium point or fixed point. For an arbitrary nonlinear function $T(q)$, which satisfies $T(q^*) = 0$ with sufficient accuracy, the Taylor expansion of the kth approximation of $q^{(k)}$ is

$$T(q) = T\big(q^{(k)}\big) + DT\big(q^{(k)}\big)\big(q^{(k+1)} - q^{(k)}\big) + ... \tag{5.47}$$

where $q = (q_0, q_1, ..., q_n)^\top$, $T = (T_1, T_2, ..., T_n)^\top$, and $(\cdot)^\top$ represents the transpose operation. $DT\big(q^{(k)}\big) = (\partial T_i/\partial q_j)$ is the Jacobian matrix. A correction vector $h = q^{(k+1)} - q^{(k)}$ can be obtained by solving the following linear non–homogeneous equation

$$DT\big(q^{(k)}\big)h = -T\big(q^{(k)}\big) \tag{5.48}$$

5.3.1 Tracking the Fixed Point

We perform Newton's method on Eq. 5.11

$$F(x_0) := x_0 - P_\lambda(x_0) = 0 \tag{5.49}$$

where x_0 corresponds to a fixed point. The initial value in Eq. 5.2 is described as $x_0 = (x_{01}, x_{02}, ...x_{0n})^\top$. Also, assume that $x_0^{(k)}$ is the first guess of the fixed point. Then, the algorithm to obtain a $(k+1)$th order approximation is as follows

$$\begin{aligned} x_0^{(k+1)} &= x_0^{(k)} + h \\ DF\big(x_0^{(k)}\big)h &= -F\big(x_0^{(k)}\big) \end{aligned} \tag{5.50}$$

where $DF\big(x_0^{(k)}\big)$ is an $n \times n$ sized Jacobian matrix with respect to the initial value x_0 given by

$$DF\big(x_0^{(k)}\big) = I - \frac{\partial P_\lambda}{\partial x}\big(x_0^{(k)}\big) \tag{5.51}$$

where I is an $n \times n$ identity matrix and $\partial P_\lambda / \partial x$ is the following matrix

$$\frac{\partial P_\lambda}{\partial x}\big(x_0^{(k)}\big) = \begin{pmatrix} \frac{\partial \varphi_1}{\partial x_{01}}\big(\tau_p, x_0^{(k)}\big) & \frac{\partial \varphi_1}{\partial x_{02}}\big(\tau_p, x_0^{(k)}\big) & \cdots & \frac{\partial \varphi_1}{\partial x_{0n}}\big(\tau_p, x_0^{(k)}\big) \\ \frac{\partial \varphi_2}{\partial x_{01}}\big(\tau_p, x_0^{(k)}\big) & \ddots & & \vdots \\ \vdots & & \ddots & \frac{\partial \varphi_{n-1}}{\partial x_{0n}}\big(\tau_p, x_0^{(k)}\big) \\ \frac{\partial \varphi_n}{\partial x_{01}}\big(\tau_p, x_0^{(k)}\big) & \cdots & \cdots & \frac{\partial \varphi_n}{\partial x_{0n}}\big(\tau_p, x_0^{(k)}\big) \end{pmatrix} \tag{5.52}$$

The second equation of Eq. 5.50 must be solved for h by using a suitable method like the Gauss elimination. $F\big(x_0^{(k)}\big)$ is easily obtained from Eq. 5.49, but obtaining the elements of the Jacobian matrix given by Eq. 5.52 requires more work.

Rewriting Eq. 5.2

$$\frac{dx}{dt} = f(t, x, \lambda) \tag{5.53}$$

where $x = (x_1, x_2, ..., x_n)^\top$, $f(t, x) = f_1(t, x, \lambda), f_2(t, x, \lambda), ..., f_n(t, x, \lambda))^\top$, and $\varphi = (\varphi_1, \varphi_2, ..., \varphi_n)^\top$. The solution of Eq. 5.53 starting from x_0 at $t = t_0$ was defined earlier as

$$x(t) = \varphi(t, \lambda; t_0, x_0) \equiv \varphi(t, x_0) \tag{5.54}$$

Substituting the solution of this equation into Eq. 5.53, we get

$$\frac{d\varphi(t, x_0)}{dt} = f(t, \varphi(t, x_0)) \tag{5.55}$$

Differentiating this equation by x_0 yields

$$\frac{\partial}{\partial x_0}\left(\frac{d\varphi(t, x_0)}{dt}\right) = \frac{\partial}{\partial x_0}(f(t, \varphi(t, x_0))) \tag{5.56}$$

The order of differentiation on the left–hand side is commutative, and the following equation is obtained from the right–hand side

$$\frac{d}{dt}\left(\frac{\partial\varphi(t, x_0)}{\partial x_0}\right) = \frac{\partial f(t, \varphi(t, x_0), \lambda)}{\partial x}\frac{\partial\varphi(t, x_0)}{\partial x_0} \tag{5.57}$$

The above equation is of the form

$$\frac{dX}{dt} = \frac{\partial f}{\partial x}X \tag{5.58}$$

where $X = \partial\varphi/\partial x_0$ is the matrix solution of a variable coefficient linear differential equation. Equation 5.57 is known as a *variational equation* for Eq. 5.53. Also,

$$\frac{\partial\varphi(0, x_0)}{\partial x_0} = I \tag{5.59}$$

Therefore, by setting Eq. 5.59 as the initial value, we can obtain all elements in Eq. 5.52 by numerically integrating Eq. 5.57 ftom $t = 0$ to $\tau + p$. This numerical integration can be performed by using Runge–Kutta method. Once this is completed, Newton's method is ready to perform. The fixed point x_0 can be accurately located by iteration.

5.3.2 Tracking Bifurcation Sets

Let us compute a bifurcation curve on a two–parameter plane. The algorithm adds one more equation to Eq. 5.49, that is, the characteristic equation. Consider the following simultaneous equation

$$F_B := \begin{bmatrix} x_0 - P_\lambda(x_0) \\ \det(DP_\lambda(x_0^*) - \mu^* I \end{bmatrix} = 0 \tag{5.60}$$

where $DP_\lambda(x_0^*)$ denotes the derivative of the Poincaré map, P_λ, with respect to the initial value, x_0 i.e., $DP_\lambda(x_0^*) = \partial P_\lambda(x_0)/\partial x_0|_{x_0=x_0^*}$.

Define $F_B \in \mathbb{R}^{n+1}$ as

$$F_B(x_0, \lambda) = [g_1(x_0, \lambda), g_2(x_0, \lambda), ..., g_n(x_0, \lambda), \chi(x_0, \lambda, \mu^*)^\top \tag{5.61}$$

where $\chi(x_0, \lambda, \mu^*)$ is the characteristic equation. Newton's method can be used to solve Eq. 5.60.

Rewriting Eq. 5.50 as

$$\begin{aligned} u^{(k+1)} &= u^{(k)} + h \\ DF_B\big(u^{(k)}\big)h &= -F_B\big(u^{(k)}\big) \end{aligned} \tag{5.62}$$

where $u = (x_{01}, x_{02}, ..., x_{0n}, \lambda)^\top$.

The Jacobian matrix is given by

$$
\begin{aligned}
DF_B\big(u^{(k)}\big) &= \begin{pmatrix}
\frac{\partial g_1}{\partial x_{01}} & \frac{\partial g_1}{\partial x_{02}} & \cdots & \frac{\partial g_1}{\partial x_{0n}} & \frac{\partial g_1}{\partial \lambda} \\
\frac{\partial g_2}{\partial x_{01}} & \ddots & & \vdots & \vdots \\
\vdots & & \ddots & \frac{\partial g_{n-1}}{\partial x_{0n}} & \frac{\partial g_{n-1}}{\partial \lambda} \\
\frac{\partial g_n}{\partial x_{01}} & \cdots & \cdots & \frac{\partial g_n}{\partial x_{0n}} & \frac{\partial g_n}{\partial \lambda} \\
\frac{\partial \chi}{\partial x_{01}} & \cdots & \cdots & \frac{\partial \chi}{\partial x_{0n}} & \frac{\partial \chi}{\partial \lambda}
\end{pmatrix} \\
&= \begin{pmatrix}
1-\frac{\partial \varphi_1}{\partial x_{01}} & -\frac{\partial \varphi_1}{\partial x_{02}} & \cdots & -\frac{\partial \varphi_1}{\partial x_{0n}} & -\frac{\partial \varphi_1}{\partial \lambda} \\
-\frac{\partial \varphi_2}{\partial x_{01}} & \ddots & & \vdots & \vdots \\
\vdots & & \ddots & -\frac{\partial \varphi_{n-1}}{\partial x_{0n}} & -\frac{\partial \varphi_{n-1}}{\partial \lambda} \\
-\frac{\partial \varphi_n}{\partial x_{01}} & \cdots & \cdots & 1-\frac{\partial \varphi_n}{\partial x_{0n}} & -\frac{\partial \varphi_n}{\partial \lambda} \\
\frac{\partial \chi}{\partial x_{01}} & \cdots & \cdots & \frac{\partial \chi}{\partial x_{0n}} & \frac{\partial \chi}{\partial \lambda}
\end{pmatrix}
\end{aligned}
\tag{5.63}
$$

Calculating derivatives such as $\partial\varphi/\partial x_0$ is routine but obtaining remaining derivatives such as $\partial\varphi_i/\partial\lambda$ and derivatives of the characteristic equation $\chi(x_0, \lambda, \mu^*)$ with respect to the initial value x_0 and the parameter λ requires the following additional steps. First, consider the derivative with respect to a parameter, $\partial\varphi_i/\partial\lambda$. Assume the solution of Eq. 5.53 including a parameter λ as

$$x(t) = \varphi(t, \lambda; t_0, x_0) \tag{5.64}$$

Differentiating both sides of this equation with respect to λ results in

$$\frac{\partial x}{\partial \lambda} = \frac{\partial \varphi}{\partial \lambda} \tag{5.65}$$

Substituting this into Eq. 5.53, we get a linear differential equation given by

$$\frac{d}{dt}\left(\frac{\partial \varphi}{\partial \lambda}\right) = \frac{\partial f}{\partial x}\frac{\partial \varphi}{\partial \lambda} + \frac{\partial f}{\partial \lambda} \tag{5.66}$$

This is the variational equation with respect to the parameter λ. Similar to the computation of the variational equation Eq. 5.57, the solution can be obtained using a suitable numerical integration method. Next, consider the derivatives of the characteristic equation. The characteristic equation $\chi(x_0, \lambda, \mu^*)$ is the determinant of the following $n \times n$ matrix

$$S(x_0) := \frac{\partial P_\lambda}{\partial x_0} - \mu^* I = \begin{pmatrix} \frac{\partial \varphi_1}{\partial x_{01}} - \mu^* & \frac{\partial \varphi_1}{\partial x_{02}} & \cdots & \frac{\partial \varphi_1}{\partial x_{0n}} \\ \frac{\partial \varphi_2}{\partial x_{01}} & \ddots & & \vdots \\ \vdots & & \ddots & \frac{\partial \varphi_{n-1}}{\partial x_{0n}} \\ \frac{\partial \varphi_n}{\partial x_{01}} & \cdots & \cdots & \frac{\partial \varphi_n}{\partial x_{0n}} - \mu^* \end{pmatrix} \tag{5.67}$$

In Eq. 5.63, the derivatives of the characteristic equation with respect to the initial value x_0 can be obtained by using the equation given by

$$\frac{\partial \chi(x_0, \lambda, \mu^*)}{\partial x_0} = \sum_{i=1}^{n} \det(S_i) \tag{5.68}$$

where S_i are matrices that are differentiated from each element of the ith column of S with regard to x_0.

For example, if the Eq. 5.53 has a state vector $x = (x_1, x_2, x_3)^\top \in \mathbb{R}^3$, the derivative of the characteristic equation with respect to the element x_{01} in the initial value $x_0 = (x_{01}, x_{02}, x_{03})^\top$ is given by

$$
\begin{aligned}
\frac{\partial \chi(x_0, \lambda, \mu^*)}{\partial x_{01}} = \sum_{i=1}^{3} \det(S_i) = &\begin{vmatrix} \frac{\partial}{\partial x_{01}}\left(\frac{\partial \varphi_1}{\partial x_{01}} - \mu^*\right) & \frac{\partial}{\partial x_{01}}\frac{\partial \varphi_1}{\partial x_{02}} & \frac{\partial}{\partial x_{01}}\frac{\partial \varphi_1}{\partial x_{03}} \\ \frac{\partial \varphi_2}{\partial x_{01}} & \frac{\partial \varphi_2}{\partial x_{02}} - \mu^* & \frac{\partial \varphi_2}{\partial x_{03}} \\ \frac{\partial \varphi_3}{\partial x_{01}} & \frac{\partial \varphi_3}{\partial x_{02}} & \frac{\partial \varphi_3}{\partial x_{03}} - \mu^* \end{vmatrix} \\
&+ \begin{vmatrix} \frac{\partial \varphi_1}{\partial x_{01}} - \mu^* & \frac{\partial \varphi_1}{\partial x_{02}} & \frac{\partial \varphi_1}{\partial x_{03}} \\ \frac{\partial}{\partial x_{01}}\frac{\partial \varphi_2}{\partial x_{01}} & \frac{\partial}{\partial x_{01}}\left(\frac{\partial \varphi_2}{\partial x_{02}} - \mu^*\right) & \frac{\partial}{\partial x_{01}}\frac{\partial \varphi_2}{\partial x_{03}} \\ \frac{\partial \varphi_3}{\partial x_{01}} & \frac{\partial \varphi_3}{\partial x_{02}} & \frac{\partial \varphi_3}{\partial x_{03}} - \mu^* \end{vmatrix} \\
&+ \begin{vmatrix} \frac{\partial \varphi_1}{\partial x_{01}} - \mu^* & \frac{\partial \varphi_1}{\partial x_{02}} & \frac{\partial \varphi_1}{\partial x_{03}} \\ \frac{\partial \varphi_2}{\partial x_{01}} & \frac{\partial \varphi_2}{\partial x_{02}} - \mu^* & \frac{\partial \varphi_2}{\partial x_{03}} \\ \frac{\partial}{\partial x_{01}}\frac{\partial \varphi_3}{\partial x_{01}} & \frac{\partial}{\partial x_{01}}\frac{\partial \varphi_3}{\partial x_{02}} & \frac{\partial}{\partial x_{01}}\left(\frac{\partial \varphi_3}{\partial x_{03}} - \mu^*\right) \end{vmatrix}
\end{aligned}
\tag{5.69}
$$

The derivatives of the characteristic equation related to the parameter λ are the same as those in Eq. 5.68. Consequently, to calculate each element of the Jacobian matrix of Eq. 5.63, it is necessary to obtain the second derivatives of the Poincaré map P_λ for x_0 given by

$$\frac{\partial}{\partial x_{0j}}\left(\frac{\partial P_\lambda}{\partial x_0}\right) = \frac{\partial}{\partial x_{0j}}\left(\frac{\partial \varphi}{\partial x_0}\right) \tag{5.70}$$

for j=1, 2, ..., n, where x_{oj} denotes an element in the initial value x_0. Differentiating Eq. 5.57 with respect to x_0 one more time

$$\frac{d}{dt}\left\{\frac{\partial}{\partial x_0}\left(\frac{\partial \varphi}{\partial x_0}\right)\right\} = \frac{\partial f}{\partial x_0}\frac{\partial}{\partial x_{0j}}\left(\frac{\partial \varphi}{\partial x_0}\right) + \underline{\frac{\partial}{\partial x_{0j}}\left(\frac{\partial f}{\partial x_0}\right)}\left(\frac{\partial \varphi}{\partial x_0}\right)^2 \tag{5.71}$$

for $j = 1, 2, \ldots, n$. This equation is also linear. The numerical solution of Eq. 5.57 can be substituted for $\partial\varphi/\partial x_0$. The underlined part is a tensor. Although it looks complicated, it can be computed by using numerical integration.This equation is known as the second variational equation. All the elements of the Jacobian matrix given by Eq. 5.63 can now be computed.

5.3.2.1 Mathematical foundation

A nonsmooth dynamical system assumes the existence of a state space X of dimension n, the vector-valued funtion $\mathbf{f_I} : X \mapsto X$ known as the *vector field*, parameterized by an *index vector* $\mathbf{I}$. A smooth event function $h_\mathbf{I} : X \mapsto \mathbb{R}$ and a smooth *state jump function* $\mathbf{g_I} : X \mapsto X$ are associated with with index vector $\mathbf{I}$. A solution to the corresponding dynamical system is given by $\left\{\mathbf{x}_j : (t_{j-1}, t_j] \to X\right\}_{j=1}^{m}$ of m smooth curves and an associated sequence $\left\{\mathbf{I}_j\right\}_{j=1}^{m}$, such that

$$\mathbf{I}(t) = \mathbf{I}_j, t \in (t_{j-1}, t_j] \tag{5.72}$$

and

(i) The corresponding tangent vector at $\mathbf{x}_j(t)$ equals $\mathbf{f_I}(\mathbf{x}_j(t))$ is given by

$$\frac{d}{dt}\mathbf{x}_j(t) = \mathbf{f}_{\mathbf{I}j}(\mathbf{x}_j(t)) \tag{5.73}$$

(ii) The j-th segment ends at an intersection with the *event surface*

$$\left\{\mathbf{x} | h_{\mathbf{I}_j}(\mathbf{x}) = 0, h_{\mathbf{I}_{j,\mathbf{x}}}(\mathbf{x}) \cdot \mathbf{f}_{\mathbf{I}_j}(\mathbf{x}) \leq 0\right\} \tag{5.74}$$

i.e.,

$$h_{\mathbf{I}_j}(\mathbf{x}_j(t_j)) = 0 \tag{5.75}$$

(iii) The *connectivity* between the j-th and j+1 -th segments is given by a jump function $\mathbf{g}_{\mathbf{I}j}$, given by

$$\mathbf{g}_{\mathbf{I}j}(\mathbf{x}(t_j)) = \lim_{t \to t_j+} \mathbf{x}_{j+1}(t) \tag{5.76}$$

The auxiliary boundary condition corresponds to the connectivity condition

$$\lim_{t \to t_0+} \mathbf{x}_1(t) - \mathbf{g}_{\mathbf{I}m}(\mathbf{x}_m(t_m)) = 0 \tag{5.77}$$

5.3.3 Collocation Methods for Solving Boundary-Value-Problems (BVP's)

Collocation methods provide an accurate and adaptive procedure to compute the solutions of differential equations with boundary value problems. The method involves seeking an approximation of the form of piecewise polynomials of predetermined order that satisfy the given differential equation at a discrete set of points in the definition interval. This set of points is known as *collocation points.* The method is considered as robust and has become a favored methods for solving difficult problems in differential equations. consider a differential equation

$$\frac{d\mathrm{x}}{dt} = \mathbf{f}(\mathbf{x}) \tag{5.78}$$

for some vector field $\mathbf{f}$ and the solution $\mathbf{x}$(t) on the interval [0,T] for some T > 0. In order to discretize the solution $\mathbf{x}$(t), the time t is partitioned as

$$0 = t_0 < t_{1/m} < ... < t_1 < t_{1+1/m} < ... < t_2 < ... < t_N = T \tag{5.79}$$

for integers N and m. Let

$$\Delta_j = t_j - t_{j-1} \tag{5.80}$$

for all $j = 1, ..., N$.

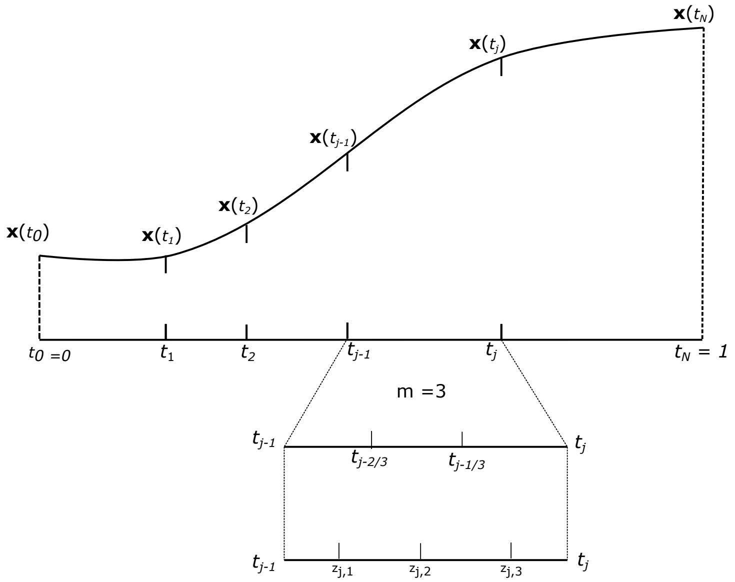

Figure 5.4: Mesh intervals, extended mesh intervals and the collocation points for a solution trajectory.

For each interval given by $[t_{j-1}, t_j]$, Lagrange polynomials are defined as

$$l_{j,i}(t) = \prod_{k=0,k\neq i}^{m} \frac{t - t_{j-k/m}}{t_{j-i/m} - t_{j-k/m}} \tag{5.81}$$

for $i = 0, ..., m$ and $j = 1, ..., N$. The piecewise polynomial function $\mathbf{p}$(t)

$$\mathbf{p}(t) = \sum_{i=0}^{m} l_{j,i}(t)\mathbf{x}(t_{j-i/m}) \tag{5.82}$$

for $t \in [t_{j-1}, t_j]$, interpolates the function $\mathbf{x}(t)$ at the points $\mathbf{x}(t_{j-i/m})$ for $j = 1, ..., N, i = 0, ..., m$. Now, consider the m-th order Legendre polynomial on the interval [0,1] and its roots given by $z_i, i = 1, ..., m$. For each interval $[t_{j-1}, tj]$, define $z_{i,j}$ as

$$z_{i,j} = t_{j-1} + z_i\Delta_j \tag{5.83}$$

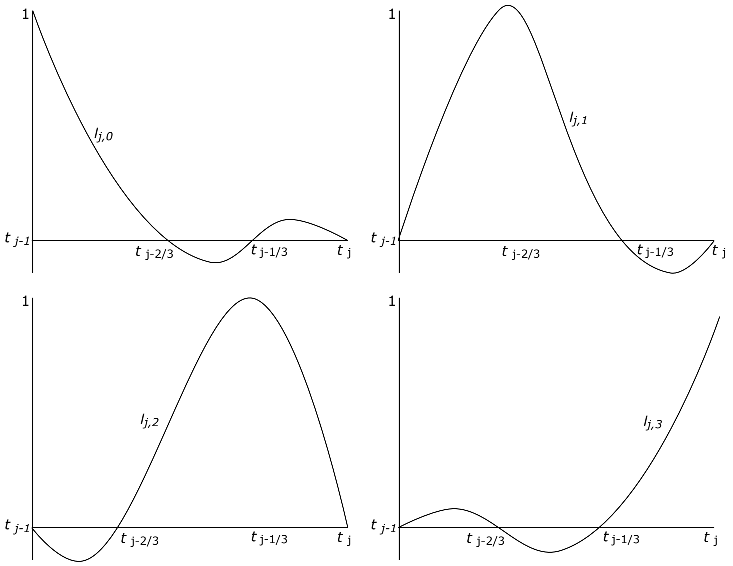

Figure 5.5: Lagrange basis polynomials corresponding to the mesh points.

Then, an approximation to the solution for the orifinal differential equation is obtained by seeking the $n(N+1)$ discrete values of the components of the unknown function $\mathbf{x}(t)$ at $t_{j-i/m}$ for $j = 1, ..., N, i = 1, ..., m$ and t_N so that the piecewise polynomial function $\mathbf{p}(t)$ satisfies the system of nmN equations

$$\mathbf{p}'(z_{j,i}) - \mathbf{f}(\mathbf{p}(z_{j,i}) = 0 \tag{5.84}$$

for $j = 1, ..., N$ and $i = 1, ..., m$ and associated n boundary conditions.

Let $\mathbf{x}_0$ denote an initial guess for the vector consisting of concatenation of the unknown discretization values $\mathbf{x}(t_{j-i/m})$. An improved estimate for the solution vector $\mathbf{x}$ can be obtained using a correction factor $\Delta\mathbf{x}$, where

$$\mathbf{J}(\mathbf{x}_0).\Delta\mathbf{x} = -\mathbf{F}(\mathbf{x}_0) \tag{5.85}$$

corresponding to a new iteration for Newton-Raphson method. Here, $\mathbf{F}(\mathbf{x}_0)$ is the vector of residuals of the set of equations and $\mathbf{J}(\mathbf{x}_0)$ is the Jacobian matrix of the equations with respect to $\mathbf{x}$ evaluated at the point $\mathbf{x}_0$. The inversion of the linear equation for Δx is obtained using *Gauss elimination*. The process is repeated until the residual is within the required tolerance limits.

5.3.4 Implementation of the Algorithm

The discussion from the previous section and derivation of variational equations is an important step in the study of nonsmooth dynamical systems. However, the implementation of the derived equation using computer algorithms is a challenge itself. Although multiple algorithms and software are available for analyzing and tracking the fixed points and bifurcation sets for smooth and autonomous dynamical systems, there are no computational tools available to simulate nonsmooth nonautonomous systems and track the bifurcation sets directly. Toolboxes such as MATCONT [61], SLIDECONT [62], BunKi, etc. can be used to perform bifurcation analysis to study dynamical systems. However, these toolboxes cannot be used to simulate systems with state-space jumps. More recently, the toolbox developed by Thota [63] has added functionality to previously existing toolboxes. However, due to extensive documentation and use of many standard MATLAB functions, the implementation of the variational equations derived for the system was found to be most suitable using COCO's *hspo* toolbox [64].

The mathematical methodology known as *parameter continuation* is the central theme of all the toolboxes available for studying dynamical systems. The theoretical concept is based on the observation that the solutions to parameterized mathematical equations often belong to solution families, in turn parameterized by problem parameters. There are exceptions to this general idea, but that is a current field of research in applied mathematics and is outside the scope of this work. Parameter continuation, therefore, is a complementary tool as it enables the study of dynamical systems and to explore the character and persistence of solutions across parameter domains, even in the absence of closed-form mathematical analysis.

The following section describes a dynamical system with multiple segments as needed for encoding the governing equations of the system in COCO [64].

5.3.5 Multisegment Boundary Value Problem and Its Encoding

Consider a general multisegment boundary-value problem that applies to the continuation of periodic orbits in hybrid dynamical systems. A sequence of M smooth curves is defined and associated to a sequence of triplets $\{(\mathfrak{m}_j, \mathfrak{e}_j, \mathfrak{r}_j)\}_{j=1}^{M}$, referred to as the *orbit signature*, so that

$$\frac{dy^{(j)}}{dt} = f\left(y^{(j)}, p; \mathfrak{m}_j\right) \tag{5.86}$$

and

$$h\left(y^{(j)}(T_j), p; \mathfrak{e}_j\right) = 0 \tag{5.87}$$

for j = 0, ..., M,

$$g\left(y^{(j)}(T_j), p; \mathfrak{r}_j\right) = y^{(j+1)}(0) \tag{5.88}$$

for j = 0, ..., M-1, and

$$g\left(y^{(j)}(T_M), p; \mathfrak{r}_M\right) = y^{(1)}(0) \tag{5.89}$$

for families of smooth functions $f(\cdot, \cdot, \mathfrak{m}_j) : \mathbb{R}^{n_j} \times \mathbb{R}^q \to \mathbb{R}^{n_j}$ and $h(\cdot, \cdot, \mathfrak{e}_j) : \mathbb{R}^{n_j} \times \mathbb{R}^q \to \mathbb{R}$ for $j = 1, ..., M$, $g(\cdot, \cdot, \mathfrak{m}_j) : \mathbb{R}^{n_j} \times \mathbb{R}^q \to \mathbb{R}^{n_{j+1}}$ for $j = 1, .., M-1$ and $g(\cdot, \cdot, \mathfrak{m}_M) : \mathbb{R}^{n_M} \times \mathbb{R}^q \to \mathbb{R}^{n_1}$ parameterized by

(i) the sequence of *mode identifiers* $\{\mathfrak{m}_j\}_{j=1}^{M}$,

(ii) the sequence of *event identifiers* $\{\mathfrak{e}_j\}_{j=1}^{M}$, and

(iii) the sequence of *reset identifiers* $\{\mathfrak{r}_j\}_{j=1}^{M}$, Using the formulation given above, in the case of a multisegment trajectory, each segment can be treated independently from other segment while formulating the piecewise polynomial approximation and the associated differential equations. The connectivity between consecutive segments is formulated as a boundary-value problem through the boundary conditions for each individual segment. Therefore, the operations such as Gauss elimination can be applied to each individual segment independently of other segments and the Jacobian of the individual segment trajectories can be obtained. The details for encoding the hybrid dynamical system using COCO can be found in [64].

5.4 Results and Discussion

The governing equations for the mass-spring-damper system were encoded in the COCO toolbox using the variational equation derived earlier. The Jacobians for the system, event function, and jump function with respect to the state variable and with respect to the system parameters are derived using the variational equations. These Jacobians are required to encode the system dynamics in COCO in order to simulate the system numerically.

Figures 5.6 - 5.13 show the response of the the hybrid system with nonlinear spring stiffness under parameter variation. To solve the continuation problem, the COCO toolbox requires encoding of all parameters involved in the governing equations. Initially, all the parameters are considered as *inactive*. The user is then required to pick a parameter that will be made *active* and varied in order to solve the continuation problem. All parameters were normalized according to the discussion provided in the introduction of governing equations. The figures 5.6 - 5.13 plot the response of the system in $x_1 - \Omega$ plane, where $x1$ is the peak displacement and Ω is the normalized frequency. The simulation is run for ten iterations initially and the transient dynamics are allowed to dissipate. Then, the simulation is continued. Since the process of bifurcation is used to study the persistence of equilibrium points, fixed points, and periodic cycles, a solid line represents the continuation of same qualitative behavior of the system until a new bifurcation point is detected. For example, in Fig. 5.9, the period response of the system continues between $\Omega = 0.8$ and 1.3. At this point, a bifurcation is detected and the qualitative behavior of the system changes. The new behavior continues until the next bifurcation point is detected. In general, a new branch may be detected at any bifurcation point and the continuation problem will be required to run for all the branches. For Figs. 5.6 - 5.9, the peak pressure from the detonation engine was varied. This is a possibility if the detonation engine misfires and a proper CJ detonation is not achieved. For this case, a bifurcation from periodic behavior transitioning to a Neimark-Sacker bifurcation when the peak pressure was CJ pressure. For lower pressures, the periodic behavior continued and no branches or transition to a new qualitative behavior was observed.

Figures 5.10 - 5.13 show the system response as the external load resistance is varied. As the external load resistance is the an important factor in calculating the electromagnetic damping in the system, it plays an important role in studying the system dynamics. Noticeably, in addition to Neimark-Sacker bifurcations, period doubling bifurcations were also observed.

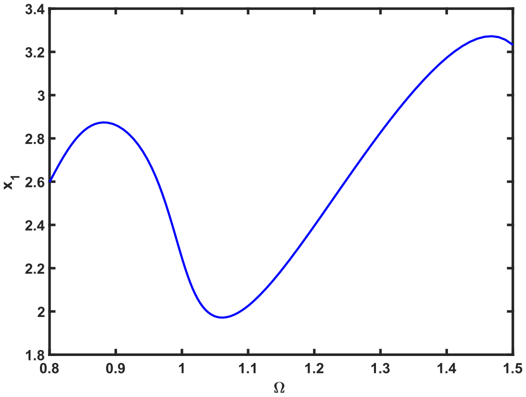

Figure 5.6: Response for
25% CJ pressure

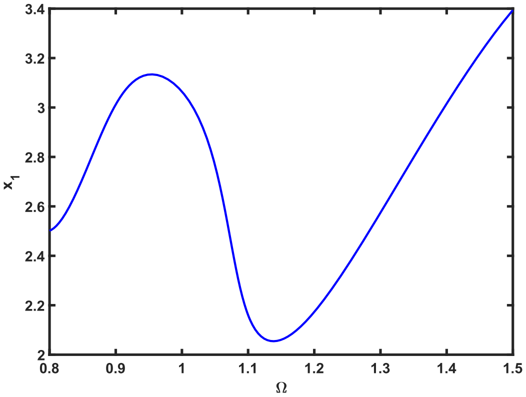

Figure 5.7: Response for
50% CJ pressure

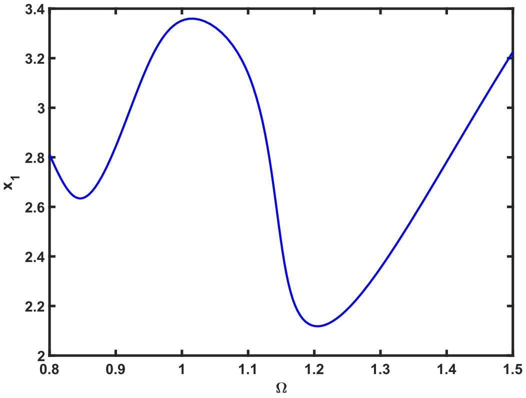

Figure 5.8: Response for
75% CJ pressure

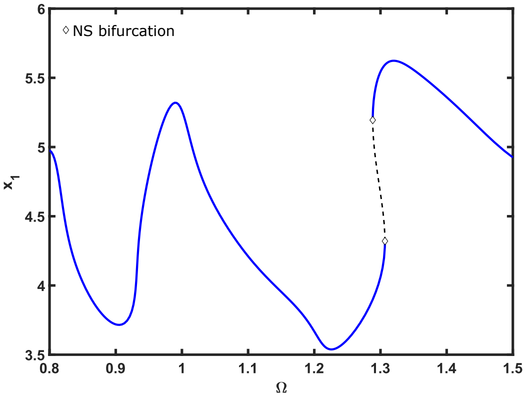

Figure 5.9: Response for
100% CJ pressure

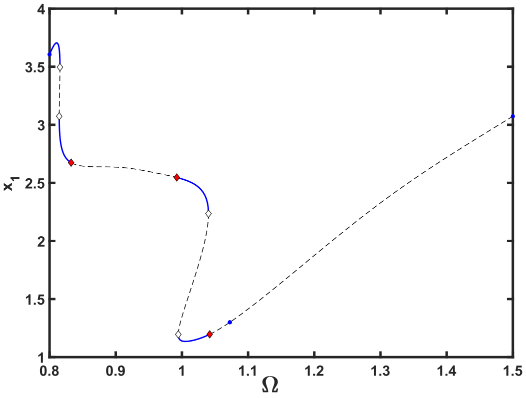

Figure 5.10: External resistance = 15 Ohms

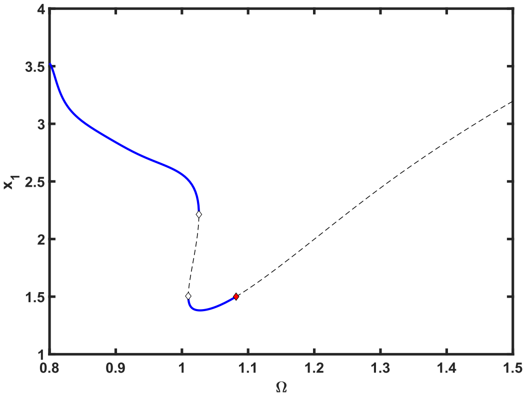

Figure 5.11: External resistance = 25 Ohms

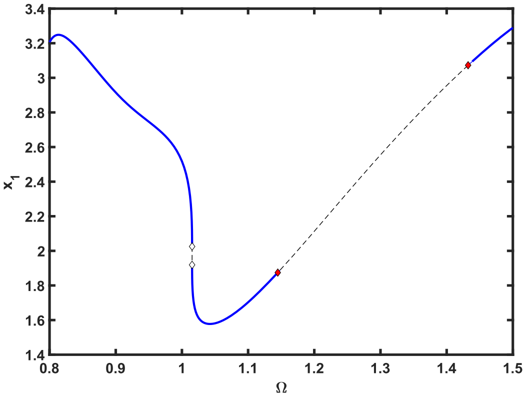

Figure 5.12: External resistance = 35 Ohms

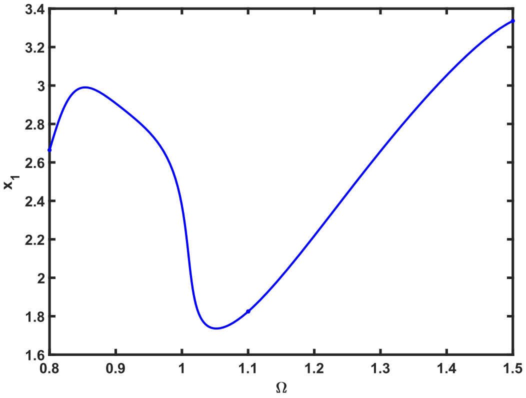

Figure 5.13: External resistance = 45 Ohms

CHAPTER 6

CONCLUSIONS AND FUTURE WORK

6.1 Conclusion

The present research investigated the application of a pulse detonation engine to drive a linear generator to produce electrical power. The previous studies by Braun et al. [13] did not account for the electromagnetic damping due to the linear generator architecture and used Friedlander equation to model the thrust generated by the pulse detonation engine.

The Friedlander model [12] represents the pressure rise and the subsequent decay of pressure in blast waves. Therefore, it is not an ideal model for the thrust generate by a pulse detonation engine. The Endo-Fujiwara model [4] was created for the analytical estimation of thrust by an ideal pulse detonation engine. The thrust generated is given by a piecewise smooth function with a constant pressure zone, followed by a decay. Therefore, the current research adopted the Endo-Fujiwara model for an ideal pulse detonation engine thrust.

In order to expand the model used by Braun, the electromagnetic damping introduced by the linear generator was also modeled into the governing equation for the mass-spring-damper system. As various topologies for linear generators exist in literature and real world applications, a comparative study of select topologies was performed. When the magnetic field generated by the four-sided topology and tubular topology is compared, neither type presents any distinct advantage over the other. However, the ease of construction for a four-sided geometry was observed in the literature. An attempt was made to use commercial simulation software to model the mass-spring-damper system and conduct high fidelity transient simulations using pulse detonation engine thrust model. However, the available functionalities of the commerical software did not allow a piecewise forcing function. Therefore, a double-sided linear generator model was chosen to continue the research as an analytical model for the damping generated by a double-sided topology was available and studies could be carried out using numerical simulation.

Since the governing equations for the mass-spring-damper system are nonsmooth and nonautonomous, a special treatment is required in the neighborhood of the discontinuity. Various available numerical methods were studied and a time-stepping method was used to simulate the system. The study was carried out for various system parameter values and it was observed that performance of the system falls off rapidly away from the tuned resonance frequency. To find a solution to this issue, mass-spring-damper systems with nonlinear spring stiffness were also studied. A nonlinear hardening spring provided a bigger bandwidth but the power generated by the system was very low and thus, a system with nonlinear hardening spring was not pursued further. For a model with nonlinear softening spring, the power output for the system was found to be appreciably higher under certain parameter values. In the case when higher power output is the aim, a mass-spring-damper with nonlinear softening spring presents an attractive option. In reality, a nonlinear softening spring system can be achieved using a snap-through arrangement as discussed in the text.

The introduction of nonlinear spring stiffness adds a dimension to the study of such systems. Due to the presence of nonlinear stiffness, the system can become unstable under certain conditions. Therefore, a thorough understanding of the system dynamics is essential. Two methods were used to study the stability of the system analytically. A composite Poincaré map and its Jacobian was derived to analyze the stability. It was observed that in the absence of energy storing elements in the linear resonator model, one of the eigenvalues of the Jacobian is always zero and the system is critically stable. This was also confirmed using the maximum Lyapunov exponent concept. For the system with nonlinear spring stiffness, the time-series output from the numerical simulations were used to calculate the maximum Lyapunov exponent. In this case also, the system was found to be stable for all parameter values tested.

As most nonlinear equations do not have a closed-form solution, any study of systems governed by such equations relies heavily on numerical analysis. However, this can be tedious in case a large number of cases need to be studied. Bifurcation analysis becomes an extremely useful tool to study the dynamics of a system under the variation of parameters. It allows a qualitative study of the system behavior as the parameters governing the system change. This enables a study of a large number of cases without the need to run simulations for individual cases. A bifurcation analysis can help to choose the domain of system parameters for favorable operations.

In order to study the dynamics of the system using bifurcation tools, Jacobians of the governing equations of the system with respect to the state variables and system parameters were derived. The implementation of continuation algorithm was carried out using the COCO toolbox and the Jacobians. It was observed that only period doubling and Neimark-Sacker bifurcation show up in the bifurcation analysis. No branch points or tangent bifurcations were observed.

6.2 Future Work

A major limitation on the current research was the lack of computational tools to simulate a full mass-spring-damper model with a nonsmooth forcing function. Due to this limitation, a double-sided linear generator topology was selected based on the availability of an analytical model. As deriving detailed analytical models for other topologies would be more suitable for electrical engineering domain, a possible path forward would be to use system modeling and identification techniques in conjunction with available commercial simulation tools to derive an analytical model for the four-sided and tubular topologies. These analytical models can then be used in the mass-spring-damper model and the power generation characteristics and stability of such systems can be studied.

Another interesting path forward would be to conduct the bifurcation analysis with three parameters. The current method only permits the bifurcation analysis with two parameters. However, this path might be more suitable for applied mathematics research.

APPENDIX A

Linear Generator Topologies and Design Details

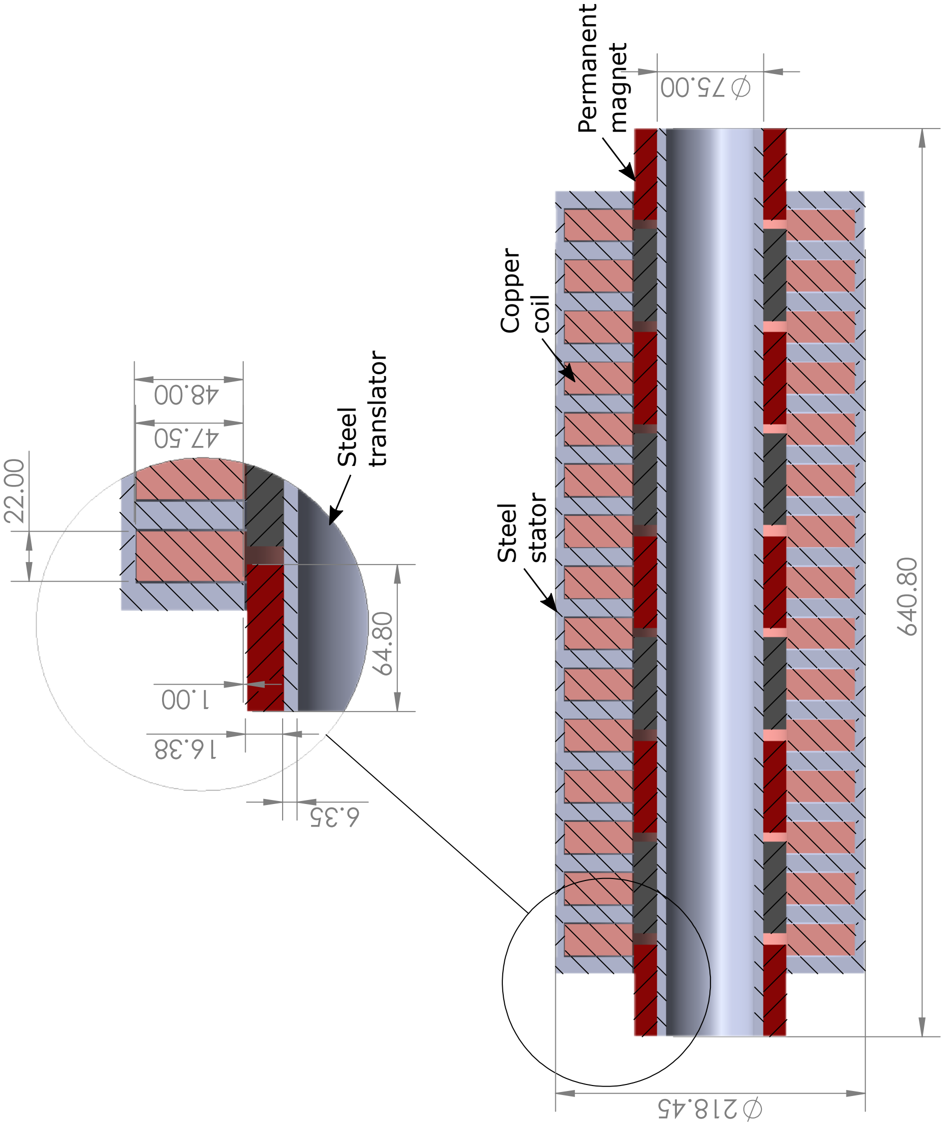
Permanent magnet
Copper coil
Steel stator
Steel translator
∅75.00
640.80
∅218.45
48.00
47.50
22.00
64.80
1.00
16.38
6.35

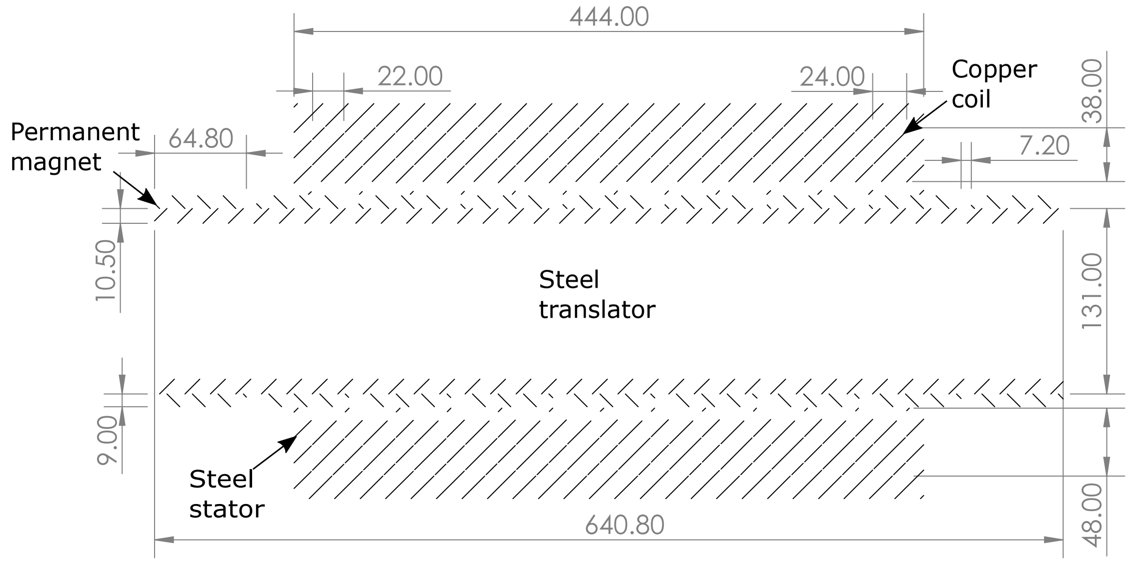

Figure A.2: Four-sided linear power construction details

APPENDIX B

Variational Equations for the Coupled System

The variational equations for bifurcation analysis of nonlinear systems given by Tsumoto et al. [65] are reproduced below.

B.1 The First Variational Equation

$$\frac{d}{dt}\begin{pmatrix}\dfrac{\partial\varphi_1}{\partial x_0}\\ \dfrac{\partial\varphi_2}{\partial x_0}\end{pmatrix} = \begin{pmatrix}\dfrac{\partial f_1}{\partial x} & \dfrac{\partial f_1}{\partial y}\\ \dfrac{\partial f_2}{\partial x} & \dfrac{\partial f_2}{\partial y}\end{pmatrix}\begin{pmatrix}\dfrac{\partial\varphi_1}{\partial x_0}\\ \dfrac{\partial\varphi_2}{\partial x_0}\end{pmatrix}, \qquad \begin{pmatrix}\dfrac{\partial\varphi_1}{\partial x_0}\\ \dfrac{\partial\varphi_2}{\partial x_0}\end{pmatrix}_{t=0} = \begin{pmatrix}1\\ 0\end{pmatrix} \tag{B.1}$$

$$\frac{d}{dt}\begin{pmatrix}\dfrac{\partial\varphi_1}{\partial y_0}\\ \dfrac{\partial\varphi_2}{\partial y_0}\end{pmatrix} = \begin{pmatrix}\dfrac{\partial f_1}{\partial x} & \dfrac{\partial f_1}{\partial y}\\ \dfrac{\partial f_2}{\partial x} & \dfrac{\partial f_2}{\partial y}\end{pmatrix}\begin{pmatrix}\dfrac{\partial\varphi_1}{\partial y_0}\\ \dfrac{\partial\varphi_2}{\partial y_0}\end{pmatrix}, \qquad \begin{pmatrix}\dfrac{\partial\varphi_1}{\partial y_0}\\ \dfrac{\partial\varphi_2}{\partial y_0}\end{pmatrix}_{t=0} = \begin{pmatrix}0\\ 1\end{pmatrix} \tag{B.2}$$

$$\frac{d}{dt}\begin{pmatrix}\dfrac{\partial\varphi_1}{\partial \lambda}\\ \dfrac{\partial\varphi_2}{\partial \lambda}\end{pmatrix} = \begin{pmatrix}\dfrac{\partial f_1}{\partial x} & \dfrac{\partial f_1}{\partial y}\\ \dfrac{\partial f_2}{\partial x} & \dfrac{\partial f_2}{\partial y}\end{pmatrix}\begin{pmatrix}\dfrac{\partial\varphi_1}{\partial \lambda}\\ \dfrac{\partial\varphi_2}{\partial \lambda}\end{pmatrix} + \begin{pmatrix}\dfrac{\partial f_1}{\partial \lambda}\\ \dfrac{\partial f_2}{\partial \lambda}\end{pmatrix}, \qquad \begin{pmatrix}\dfrac{\partial\varphi_1}{\partial \lambda}\\ \dfrac{\partial\varphi_2}{\partial \lambda}\end{pmatrix}_{t=0} = \begin{pmatrix}0\\ 0\end{pmatrix} \tag{B.3}$$

B.2 The Second Variational Equation

$$\frac{d}{dt}\begin{pmatrix}\dfrac{\partial^2\varphi_1}{\partial x_0^2}\\ \dfrac{\partial^2\varphi_2}{\partial x_0^2}\end{pmatrix} = Df\begin{pmatrix}\dfrac{\partial^2\varphi_1}{\partial x_0^2}\\ \dfrac{\partial^2\varphi_2}{\partial x_0^2}\end{pmatrix} + \left(\frac{\partial}{\partial x_o}Df\right)\begin{pmatrix}\dfrac{\partial\varphi_1}{\partial x_0}\\ \dfrac{\partial\varphi_2}{\partial x_0}\end{pmatrix} \tag{B.4}$$

$$\frac{d}{dt}\begin{pmatrix}\dfrac{\partial^2\varphi_1}{\partial y_0^2}\\ \dfrac{\partial^2\varphi_2}{\partial y_0^2}\end{pmatrix} = Df\begin{pmatrix}\dfrac{\partial^2\varphi_1}{\partial y_0^2}\\ \dfrac{\partial^2\varphi_2}{\partial y_0^2}\end{pmatrix} + \left(\frac{\partial}{\partial y_o}Df\right)\begin{pmatrix}\dfrac{\partial\varphi_1}{\partial y_0}\\ \dfrac{\partial\varphi_2}{\partial y_0}\end{pmatrix} \tag{B.5}$$

$$\frac{d}{dt}\begin{pmatrix}\dfrac{\partial^2\varphi_1}{\partial x_0\partial y_0}\\ \dfrac{\partial^2\varphi_2}{\partial x_0\partial y_0}\end{pmatrix} = Df\begin{pmatrix}\dfrac{\partial^2\varphi_1}{\partial x_0\partial y_0}\\ \dfrac{\partial^2\varphi_2}{\partial x_0\partial y_0}\end{pmatrix} + \left(\frac{\partial}{\partial x_o}Df\right)\begin{pmatrix}\dfrac{\partial\varphi_1}{\partial y_0}\\ \dfrac{\partial\varphi_2}{\partial y_0}\end{pmatrix} \tag{B.6}$$

$$\frac{d}{dt}\begin{pmatrix} \dfrac{\partial^2\varphi_1}{\partial x_0\partial\lambda} \\ \dfrac{\partial^2\varphi_2}{\partial x_0\partial\lambda} \end{pmatrix} = Df\begin{pmatrix} \dfrac{\partial^2\varphi_1}{\partial x_0\partial\lambda} \\ \dfrac{\partial^2\varphi_2}{\partial x_0\partial\lambda} \end{pmatrix} + \left(\frac{\partial}{\partial x_o}Df\right)\begin{pmatrix} \dfrac{\partial\varphi_1}{\partial\lambda} \\ \dfrac{\partial\varphi_2}{\partial\lambda} \end{pmatrix} + \left(\frac{\partial}{\partial x_0}D_\lambda f\right) \tag{B.7}$$

$$\frac{d}{dt}\begin{pmatrix} \dfrac{\partial^2\varphi_1}{\partial y_0\partial\lambda} \\ \dfrac{\partial^2\varphi_2}{\partial y_0\partial\lambda} \end{pmatrix} = Df\begin{pmatrix} \dfrac{\partial^2\varphi_1}{\partial y_0\partial\lambda} \\ \dfrac{\partial^2\varphi_2}{\partial y_0\partial\lambda} \end{pmatrix} + \left(\frac{\partial}{\partial y_o}Df\right)\begin{pmatrix} \dfrac{\partial\varphi_1}{\partial\lambda} \\ \dfrac{\partial\varphi_2}{\partial\lambda} \end{pmatrix} + \left(\frac{\partial}{\partial y_0}D_\lambda f\right) \tag{B.8}$$

where Df and $D\lambda$ are the derivatives with respect to the state variable (x, y) and the parameter λ respectively.

$$\left(\frac{\partial}{\partial x_0}Df\right) = \begin{pmatrix} \dfrac{\partial^2 f_1}{\partial x^2}\dfrac{\partial\varphi_1}{\partial x_0} + \dfrac{\partial^2 f_1}{\partial y\partial x}\dfrac{\partial\varphi_2}{\partial x_0} & \dfrac{\partial^2 f_1}{\partial x\partial y}\dfrac{\partial\varphi_1}{\partial x_0} + \dfrac{\partial^2 f_1}{\partial y^2}\dfrac{\partial\varphi_2}{\partial x_0} \\ \dfrac{\partial^2 f_2}{\partial x^2}\dfrac{\partial\varphi_1}{\partial x_0} + \frac{\partial^2 f_2}{\partial y\partial x}\dfrac{\partial\varphi_2}{\partial x_0} & \dfrac{\partial^2 f_2}{\partial x\partial y}\frac{\partial\varphi_1}{\partial x_0} + \dfrac{\partial^2 f_2}{\partial y^2}\dfrac{\partial\varphi_2}{\partial x_0} \end{pmatrix} \tag{B.9}$$

$$\left(\frac{\partial}{\partial y_0}Df\right) = \begin{pmatrix} \dfrac{\partial^2 f_1}{\partial x^2}\dfrac{\partial\varphi_1}{\partial y_0} + \dfrac{\partial^2 f_1}{\partial y\partial x}\dfrac{\partial\varphi_2}{\partial y_0} & \dfrac{\partial^2 f_1}{\partial x\partial y}\dfrac{\partial\varphi_1}{\partial y_0} + \dfrac{\partial^2 f_1}{\partial y^2}\dfrac{\partial\varphi_2}{\partial y_0} \\ \dfrac{\partial^2 f_2}{\partial x^2}\dfrac{\partial\varphi_1}{\partial y_0} + \dfrac{\partial^2 f_2}{\partial y\partial x}\dfrac{\partial\varphi_2}{\partial y_0} & \dfrac{\partial^2 f_2}{\partial x\partial y}\dfrac{\partial\varphi_1}{\partial y_0} + \dfrac{\partial^2 f_2}{\partial y^2}\dfrac{\partial\varphi_2}{\partial y_0} \end{pmatrix} \tag{B.10}$$

$$\left(\frac{\partial}{\partial x_0}D_\lambda f\right) = \begin{pmatrix} \dfrac{\partial^2 f_1}{\partial x\partial\lambda}\dfrac{\partial\varphi_1}{\partial x_0} + \dfrac{\partial^2 f_1}{\partial y\partial\lambda}\dfrac{\partial\varphi_2}{\partial x_0} \\ \dfrac{\partial^2 f_2}{\partial x\partial\lambda}\dfrac{\partial\varphi_1}{\partial x_0} + \dfrac{\partial^2 f_2}{\partial y\partial\lambda}\dfrac{\partial\varphi_2}{\partial x_0} \end{pmatrix} \tag{B.11}$$

$$\left(\frac{\partial}{\partial y_0}D_\lambda f\right) = \begin{pmatrix} \dfrac{\partial^2 f_1}{\partial x\partial\lambda}\dfrac{\partial\varphi_1}{\partial y_0} + \dfrac{\partial^2 f_1}{\partial y\partial\lambda}\dfrac{\partial\varphi_2}{\partial y_0} \\ \dfrac{\partial^2 f_2}{\partial x\partial\lambda}\dfrac{\partial\varphi_1}{\partial y_0} + \dfrac{\partial^2 f_2}{\partial y\partial\lambda}\dfrac{\partial\varphi_2}{\partial y_0} \end{pmatrix} \tag{B.12}$$

$$c_1 = \frac{F_{external}}{m}$$

$$c_2 = \frac{\left(\frac{2\pi\ B_t\ w_t\ d\ n\ q\ c}{w_p}\right)^2}{m\ R_{load}\ \mu}$$

$$c_3 = \frac{2\pi}{w_p}$$

$$\omega_n = \sqrt{\frac{k}{m}}$$

state variable	Machine variable	ODE	Initial value
v	x_1	$\dot{x}_1 = x_2$	v_0
u	x_2	$\dot{x}_2 = c_1 - c_2 sin^2(c_3x_1)x_2 - \omega_n^2 x_1$	u_0
z	x_3	$\dot{x}_3 = 1$	z_0
$\frac{\partial v}{\partial v_0}$	x_4	$\dot{x}_4 = x_5$	1
$\frac{\partial u}{\partial v_0}$	x_5	$\dot{x}_5 = -[\omega_n^2 + 2c_2c_3cos(c_3x_1)sin(c_3x_1)x_2]x_4 - c_2sin^2(c_3x_1)x_5$	0
$\frac{\partial z}{\partial v_0}$	x_6	$\dot{x}_6 = 0$	0
$\frac{\partial v}{\partial u_0}$	x_7	$\dot{x}_7 = x_8$	0
$\frac{\partial u}{\partial u_0}$	x_8	$\dot{x}_8 = -[\omega_n^2 + 2c_2c_3cos(c_3x_1)sin(c_3x_1)x_2]x_7 - c_2sin^2(c_3x_1)x_8$	1
$\frac{\partial z}{\partial u_0}$	x_9	$\dot{x}_9 = 0$	0
$\frac{\partial v}{\partial z_0}$	x_{10}	$\dot{x}_{10} = x_{11}$	0
$\frac{\partial u}{\partial z_0}$	x_{11}	$\dot{x}_{11} = -[\omega_n^2 + 2c_2c_3cos(c_3x_1)sin(c_3x_1)x_2]x_{10} - c_2sin^2(c_3x_1)x_{11}$	0
$\frac{\partial z}{\partial z_0}$	x_{12}	$\dot{x}_{12} = 0$	1

state variable	Machine variable	ODE	Initial value
v	x_{13}	$\dot{x}_{13} = x_{14}$	v_1
u	x_{14}	$\dot{x}_{14} = c_1 - c_2 sin^2(c_3 x_{13}) x_{14} - \omega_n^2 x_{13}$	u_1
z	x_{15}	$\dot{x}_{15} = 1$	z_1
$\frac{\partial v}{\partial v_1}$	x_{16}	$\dot{x}_{16} = x_{17}$	1
$\frac{\partial u}{\partial v_1}$	x_{17}	$\dot{x}_{17} = -[\omega_n^2 + 2c_2c_3cos(c_3x_{13})sin(c_3x_{13})x_{14}]x_{16} - c_2sin^2(c_3x_{13})x_{17}$	0
$\frac{\partial z}{\partial v_1}$	x_{18}	$\dot{x}_{18} = 0$	0
$\frac{\partial v}{\partial u_1}$	x_{19}	$\dot{x}_{19} = x_{20}$	0
$\frac{\partial u}{\partial u_1}$	x_{20}	$\dot{x}_{20} = -[\omega_n^2 + 2c_2c_3cos(c_3x_{13})sin(c_3x_{13})x_{14}]x_{19} - c_2sin^2(c_3x_{13})x_{20}$	1
$\frac{\partial z}{\partial u_1}$	x_{21}	$\dot{x}_{21} = 0$	0
$\frac{\partial v}{\partial z_1}$	x_{22}	$\dot{x}_{22} = x_{23}$	0
$\frac{\partial u}{\partial z_1}$	x_{23}	$\dot{x}_{23} = -[\omega_n^2 + 2c_2c_3cos(c_3x_{13})sin(c_3x_{13})x_{14}]x_{22} - c_2sin^2(c_3x_{13})x_{23}$	0
$\frac{\partial z}{\partial z_1}$	x_{24}	$\dot{x}_{24} = 0$	1

state variable	Machine variable	ODE	Initial value
v	x_{25}	$\dot{x}_{25} = x_{26}$	v_2
u	x_{26}	$\dot{x}_{26} = -c_2 sin^2(c_3 x_{25}) x_{26} - \omega_n^2 x_{25}$	u_2
z	x_{27}	$\dot{x}_{27} = 1$	z_2
$\frac{\partial v}{\partial v_2}$	x_{28}	$\dot{x}_{28} = x_{29}$	1
$\frac{\partial u}{\partial v_2}$	x_{29}	$\dot{x}_{29} = -[\omega_n^2 + 2c_2 c_3 cos(c_3 x_{25}) sin(c_3 x_{25}) x_{26}] x_{28} - c_2 sin^2(c_3 x_{25}) x_{29}$	0
$\frac{\partial z}{\partial v_2}$	x_{30}	$\dot{x}_{30} = 0$	0
$\frac{\partial v}{\partial u_2}$	x_{31}	$\dot{x}_{31} = x_{32}$	0
$\frac{\partial u}{\partial u_2}$	x_{32}	$\dot{x}_{32} = -[\omega_n^2 + 2c_2 c_3 cos(c_3 x_{25}) sin(c_3 x_{25}) x_{26}] x_{31} - c_2 sin^2(c_3 x_{25}) x_{32}$	1
$\frac{\partial z}{\partial u_2}$	x_{33}	$\dot{x}_{33} = 0$	0
$\frac{\partial v}{\partial z_2}$	x_{34}	$\dot{x}_{34} = x_{35}$	0
$\frac{\partial u}{\partial z_2}$	x_{35}	$\dot{x}_{35} = -[\omega_n^2 + 2c_2 c_3 cos(c_3 x_{25}) sin(c_3 x_{25}) x_{26}] x_{34} - c_2 sin^2(c_3 x_{25}) x_{35}$	0
$\frac{\partial z}{\partial z_2}$	x_{36}	$\dot{x}_{36} = 0$	1

APPENDIX C

Sample Simulink Models for Calculating Jacobian of Composite Poincaré Map

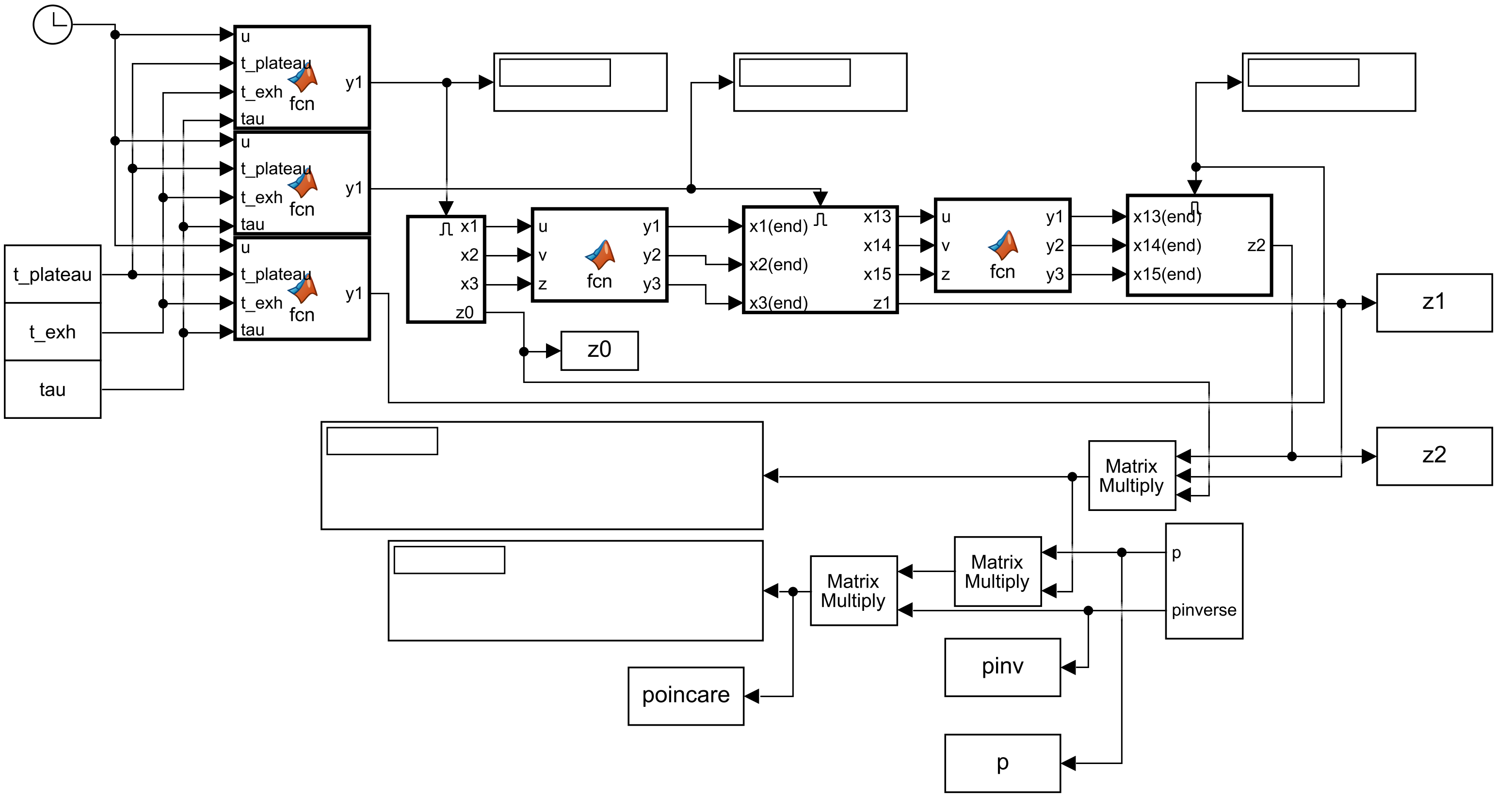

Figure C.1: Top level simulink model for calculating Jacobian of composite Poincare map of linear oscillator.

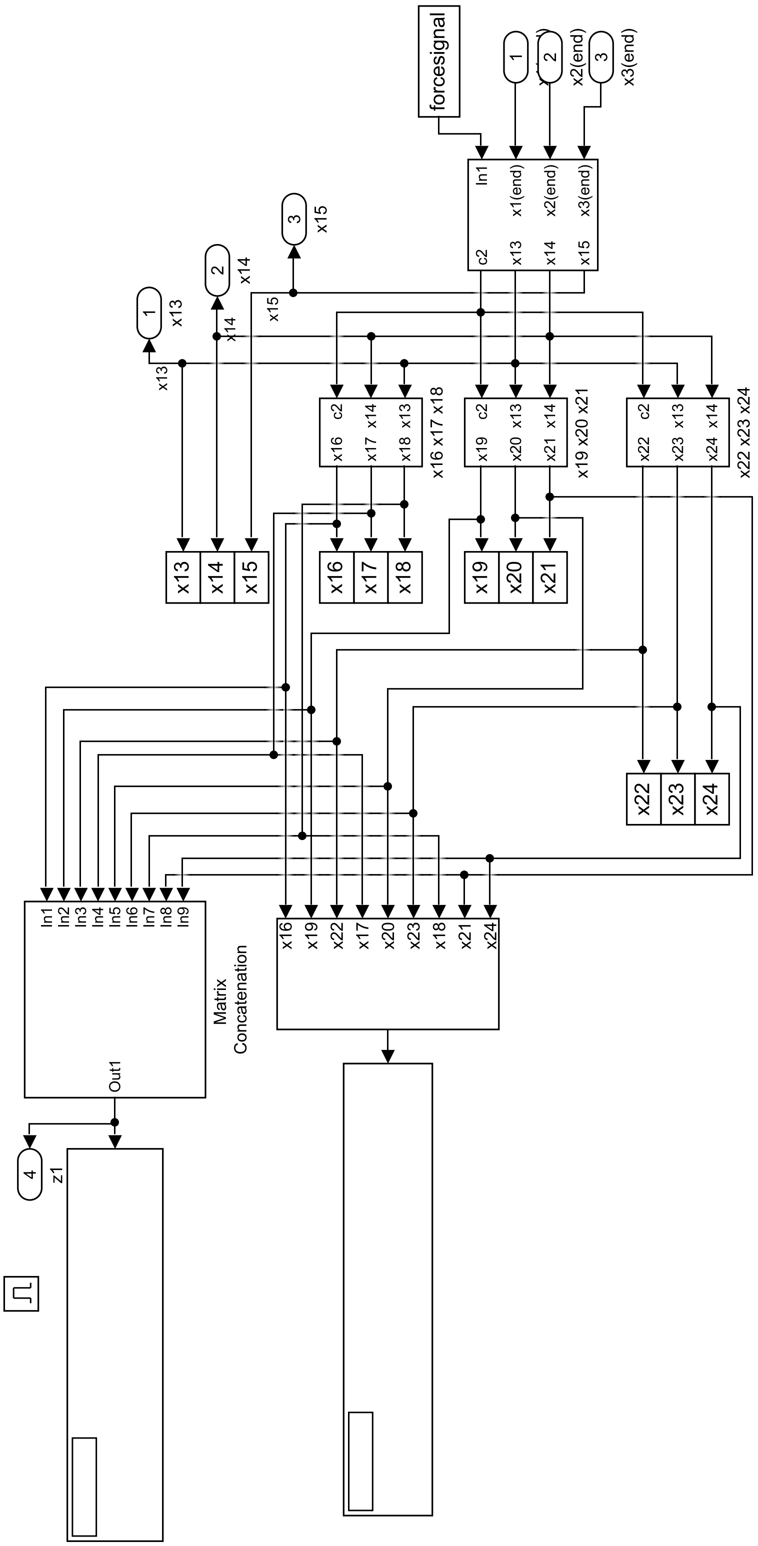

Figure C.2: Sample Simulink model for calculating variational equations x16 to x24.

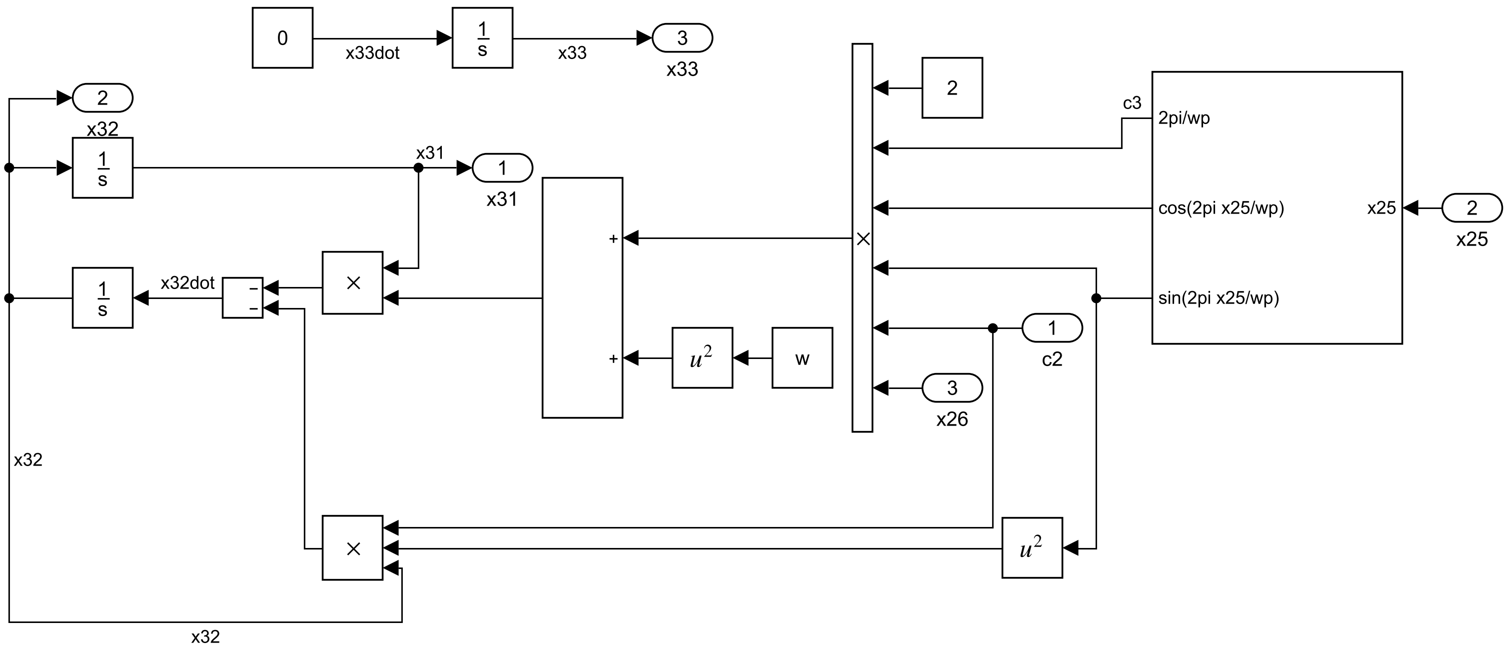

Figure C.3: Sample Simulink model for calculating derivatives with respect to its initial conditions.

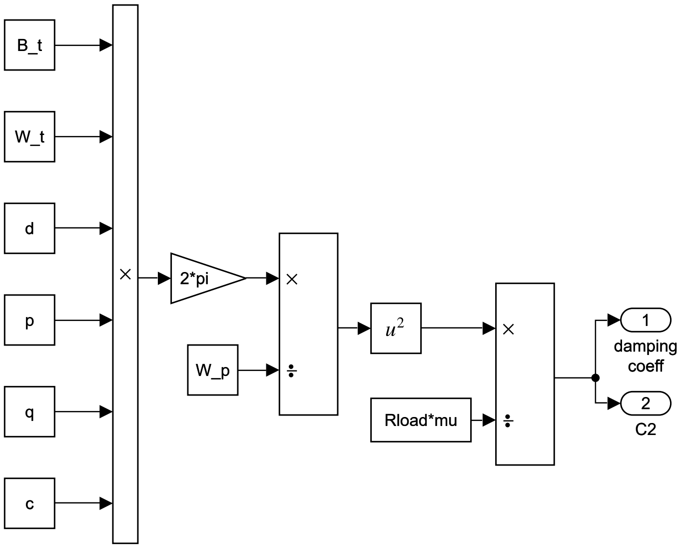

Figure C.4: Sample Simulink model for calculating a constant in a variational equation.

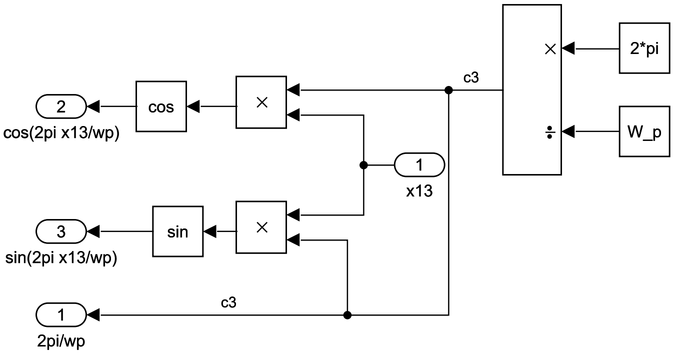

Figure C.5: Sample Simulink model for calculating one term in a variational equation.

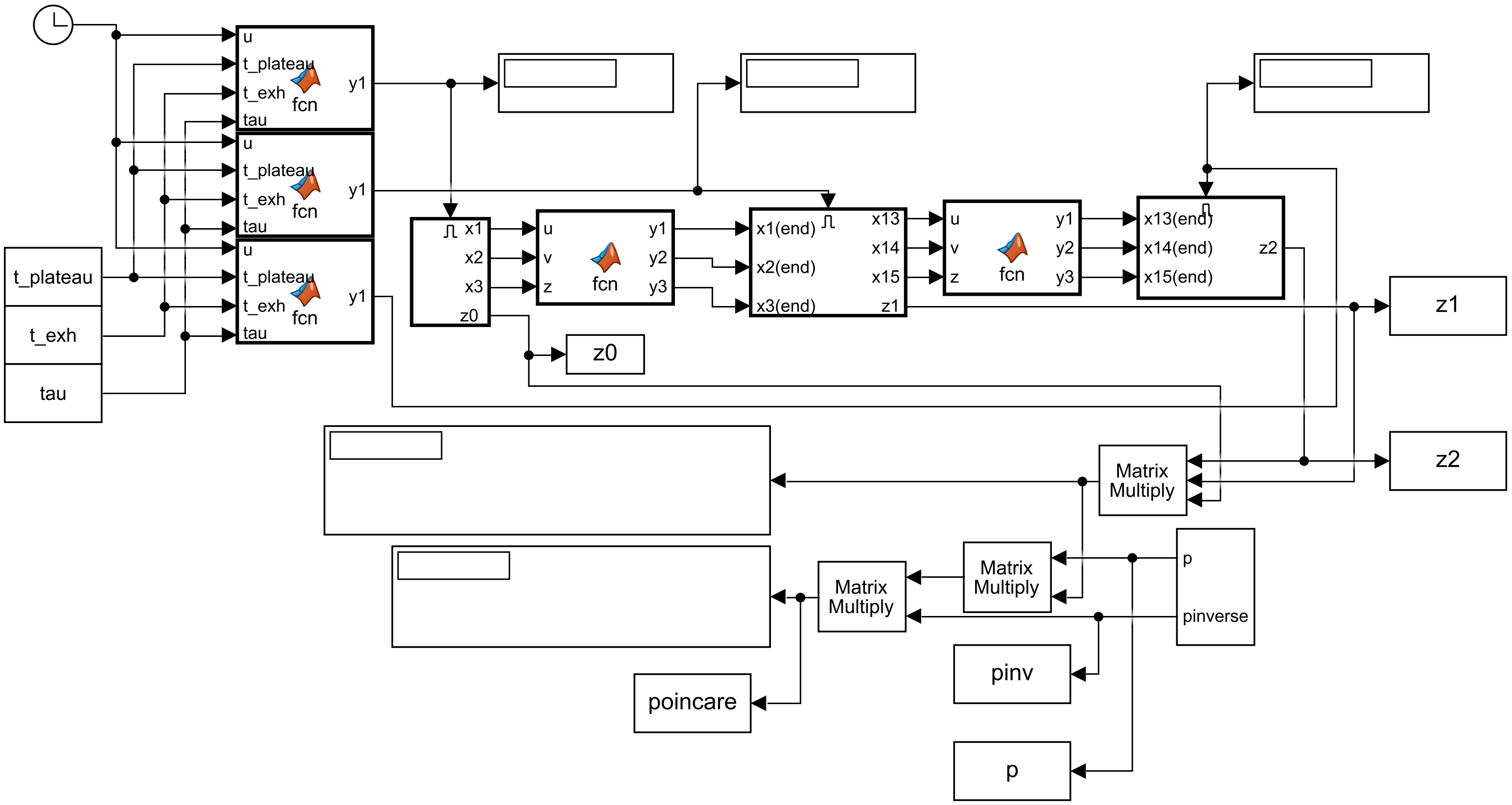

Figure C.6: Top level simulink model for calculating Jacobian of composite Poincare map of linear oscillator.

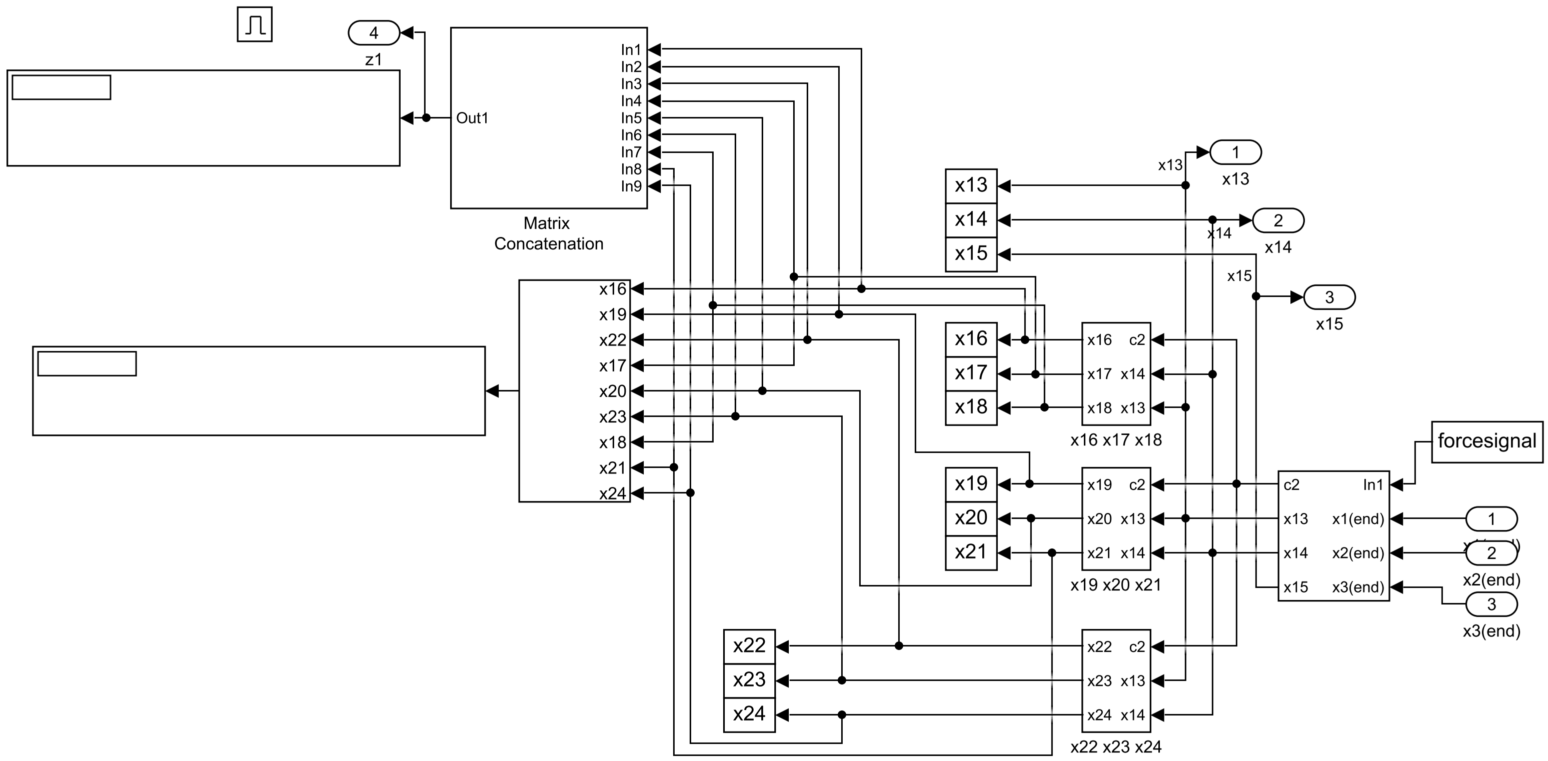

Figure C.7: Sample Simulink model for calculating variational equations x16 to x24.

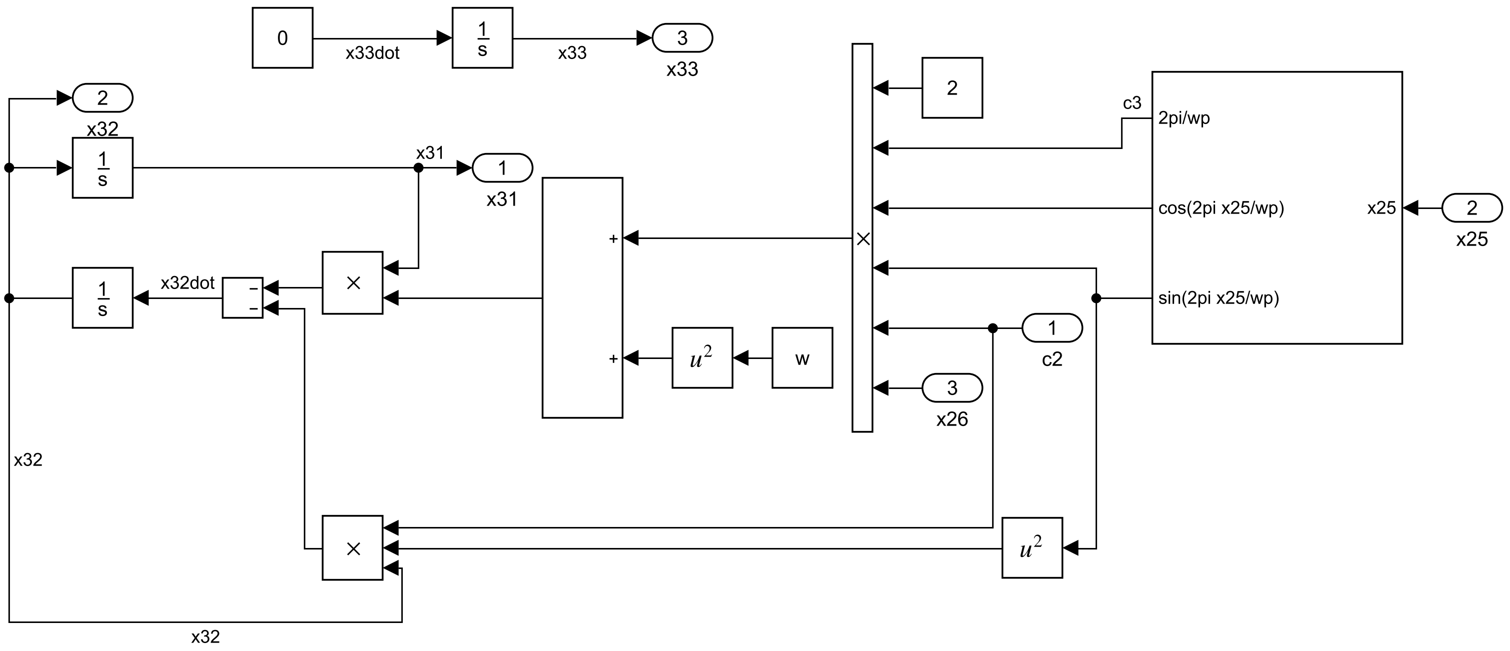

Figure C.8: Sample Simulink model for calculating derivatives with respect to its initial conditions.

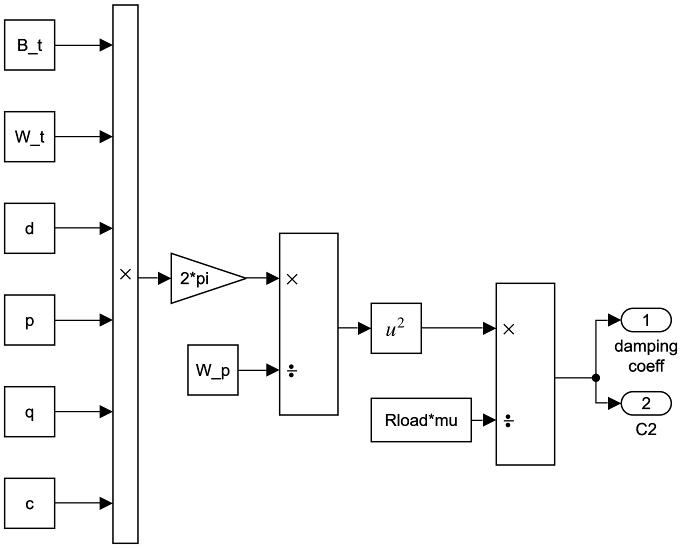

Figure C.9: Sample Simulink model for calculating a constant in a variational equation.

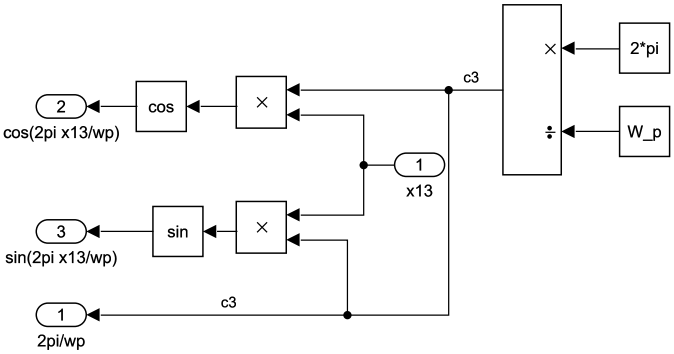

Figure C.10: Sample Simulink model for calculating one term in a variational equation.

REFERENCES

[1] Mizener, A.R., 2018, “Performance Modeling and Experiental Investigations of Rotating Detonation Engines,” Ph.D. thesis, The University of Texas at Arlington, TX, USA.

[2] Joshi, D.D., 2014, “Unsteady Thrust Measurement Techniques for Pulse Detonation Engines,” Ph.D. thesis, The University of Texas at Arlington, USA.

[3] Panicker, P.K., 2008, “The Development and Testing of Pulsed Detonation Engine Ground Demonstrators,” Ph.D. thesis, The University of Texas at Arlington, TX, USA.

[4] Endo, T. and Fujiwara, T., 2003, “Analytical Estimation of Performance Parameters of an Ideal Pulse Detonation Engine,” *Trans. Japan. Soc. Aero. Space Sci.*, **45**(150), pp. 249–254.

[5] Arnold Magnetic Technologies, *Neodymium-Iron-Boron Magnet Grades*, rev. 181031.

[6] Glassman, I., Yetter, R.A., and Glumac, N.G., 2014, *Combustion*, Academic, 4th edition.

[7] Kuznetsov, Y.A., Rinaldi, S., and Gragnani, A., 2003, “One-Parameter Bifurcations in Planar Filippov Systems,” *Int. J. Bifurc. Chaos Appl. Sci. Eng.*, **13**(08), pp. 2157–2188.

[8] Bussing, T.R.A., 2000, “Pulse Detonation Electrical Power Generation Apparatus with Water Injection,” U.S. Patent No. 6,062,018.

[9] Schick, L.A. and Dean, A., 2006, “Hybrid Fuell Cell-Pulse Detonation Power System,” U.S. Patent No. 7,150,143.

[10] Lu, F.K. and Wilson, D.R., 2008, "Scalable Power Generation Using a Pulse Detonation Engine," U.S. Patent No. 7,340,903.

[11] Braun, E.M., Lu, F.K., Sagov, M., Wilson, D.R., and Grubyi, P., 2010, "Proof-of-Principle Detonation Driven, Linear Electric Generator Facility," in: *8th Annual International Energy Conversion Engineering Conference, AIAA 2010-6767.*

[12] Friedlander, F.G. and Taylor, G.I., 1946, "The Diffraction of Sound Pulses I: Diffraction by a Semi-Infinite Plane," *Proc. R. Soc. Lond. A.*, **186**.

[13] Braun, E.M., 2012, "New Detonation Concepts for Propulsion and Power Generation," Ph.D. thesis, The University of Texas at Arlington, TX, USA.

[14] Peace, J.T., 2019, "Gasdynamic Phenomena and Propulsive Performance of Pulde Detonation Engines," Ph.D. thesis, The University of Texas at Arlington, TX, USA.

[15] Berthelot, M. and Vieille, P., 1883, "Sur la vitesse de propagation des phénoménes explosifs dans les Gaz," *Comptes Rendus de l'Académie des Sciences*, **93**, pp. 559–601.

[16] Mallard, E. and Le Chátelier, H., 1883, "Recherches expérimentales et théoriques sur le combustion des mélanges gazeux explosifs," *Annales des Mines*, **4**, pp. 274–295.

[17] Chapman, D.L., 1899, "On The Rate of Explosion in Gases," *The London, Edinburgh, and Dublin Philosophical Magazine and Journal of Science*, **47**(284), pp. 90–104.

[18] Jouguet, E., 1899, " Sur la propagation des réactions chimiques dans les gaz," *J. des Mathémathiques Pures Appliquées*, **1**, pp. 347–425.

[19] Zel'dovich, Y.B., 1940, "K teori rasprostranenia detonazi v gasoobrasnikh systemakh," *Zhurnal Experimental'noi i Teoreticheskoi Fiziki*, **10**, pp. 543–568.

[20] Neumann, J.V., 1942, "Theory of Detonation Waves. Progress Report to National Defense Research Committee Div. B, OSRD-549," .

[21] Doring, W., 1943, "Uber den Detonationsvorgang in Gasen," *Annalen der Physik*, **435**(67), pp. 421–436.

[22] Taylor, G., 1958, "Gas Dynamics of Combustion and Detonation," *Princeton Series in High Speed Aerodynamics and Jet Propulsion*, **3**.

[23] Joshi, D.D. and Lu, F.K., 2016, "Unsteady Thrust Measurement for Pulse Detonation Engines," *J. Propul. Power*, **32**(1), pp. 225–236.

[24] Gordon, S. and McBride, B., 1996, *Computer Program for Calculation of Complex Chemical Equilibrium Compositions and Applications*, NASA Reference Publication 1311.

[25] Kimoulakis, N.M., Kladas, A.G., and Tegopoulos, J.A., 2008, "Power Generation Optimization From Sea Waves by Using a Permanent Magnet Linear Generator Drive," *IEEE Trans. Magn.*, **44**(6), pp. 1530–1533.

[26] Trapanese, M., Cipriani, G., Corpora, M., and Di Dio, V., 2017, "A General Comparison Between Various Types of Linear Generators for Wave Energy Conversion," pp. 1–5.

[27] Thorburn, K., 2006, "Electric Energy Conversion Systems: Wave Energy and Hydropower," Ph.D. thesis, Uppsala Universitet, Sweden.

[28] Leijon, M., Bernhoff, H., Ågren, O., Isberg, J., Sundberg, J., Berg, M., Karlsson, K.E., and Wolfbrandt, A., 2005, "Multiphysics Simulation of Wave Energy to Electric Energy Conversion by Permanent Magnet Linear Generator," *IEEE T. Energy Conver.*, **20**(1), pp. 219–224.

[29] Zheng, Z.Q., Huang, P., Gao, D.X., and Chang, Z.Y., 2015, "Analysis of Electromagnetic Force of the Linear Generator in Point Absorber Wave Energy Converters," *J Mar. Sci. Tech.-Taiw.*, **23**(4), pp. 475–480.

[30] Brogliato, B., 2016, *Nonsmooth Mechanics*, Springer, 3rd edition.

[31] Kunze, M., 2000, *Non-Smooth Dynamical Systems*, Springer, 1st edition.

[32] Leine, R.I., van Campen, D.H., and van de Vrande, B.L., 2000, "Bifurcations in Nonlinear Discontinuous Systems," *Nonlinear Dynamics*, **23**(2), pp. 105–164.

[33] Andronov, A.A., Vitt, A.A., and Khaikin, S.E., 2013, *Theory of Oscillators: Adiwes International Series in Physics*, volume 4, Elsevier.

[34] Di Bernardo, M., Feigin, M., Hogan, S., and Homer, M., 1999, "Local Analysis of C-bifurcations in n-dimensional Piecewise-smooth Dynamical Systems," *Chaos Soliton Fract.*, **11**(10), pp. 1881–1908.

[35] Feigin, M., 1994, "Forced Oscillations in Systems with Discontinuous Nonlinearities," *Nauka, Moscow.*

[36] Peterka, F., 1974, "Laws of Impact Motion of Mechanical Systems with One Degree of Freedom. I Theoretical Analysis of n-multiple 1/n-Impact Motions," *Acta Technica CSAV*, **19**(4), pp. 462–473.

[37] Babitsky, V.I., 2013, *Theory of Vibro-Impact Systems and Applications*, Springer.

[38] Filippov, A.F., 2013, *Differential Equations with Discontinuous Righthand Sides*, volume 18, Springer.

[39] Acary, V. and Brogliato, B., 2008, *Numerical Methods for Nonsmooth Dynamical Systems*, volume 35, Springer, 1st edition.

[40] Dieci, L. and Lopez, L., 2012, "A Survey of Numerical Methods for IVPs of ODEs with Discontinuous Right-Hand Side," *J. Comput. Appl. Math.*, **236**(16), pp. 3967–3991.

[41] Piiroinen, P.T. and Kuznetsov, Y.A., 2008, "An Event-driven Method to Simulate Filippov Systems with Accurate Computing of Sliding Motions," *ACM Trans. Math. Softw.*, **34**(3), pp. 1–24.

[42] Teixeira, M.A. and Silva, P.R.d.S., 2012, "Regularization and Singular Perturbation Techniques for Non-Smooth Systems," *Physica D: Nonlinear Phenomena*, **241**(22), pp. 1948–1955.

[43] Leine, R., 2000, "Bifurcations in Discontinuous Mechanical Systems of Filippov-Type," Ph.D. thesis, Technische Universiteit Eindhoven, Netherlands.

[44] Stewart, D.E., 2000, "Rigid-Body Dynamics with Friction and Impact," *SIAM Review*, **42**(1), pp. 3–39.

[45] Dieci, L. and Lopez, L., 2009, "Sliding Motion in Filippov Differential Systems:Theoretical Results and a Computational Approach," *SIAM J. Numer. Anal.*, **47**(3), pp. 2023–2051.

[46] Biak, M., Hanus, T., and Janovska, D., 2013, "Some Applications of Filippov Dynamical Systems," *J. Comput. Appl. Math.*, **254**, pp. 132 – 143.

[47] Enright, W., Jackson, K., Norsett, S., and Thomsen, P., 1988, "Effective Solution of Discontinuous IVPs using a Runge-Kutta Formula Pair with Interpolants," *Appl. Math. Comput.*, **27**(4), pp. 313 – 335.

[48] Calvo, M., Montijano, J., and Rández, L., 2003, "On the Solution of Discontinuous IVPs by Adaptive Runge–Kutta Codes," *Numerical Algorithms*, **33**(1), pp. 163–182.

[49] Mannshardt, R., 1978, "One-Step Methods of Any Order for Ordinary Differential Equations with Discontinuous Right-Hand Sides," *Numerische Mathematik*, **31**(2), pp. 131–152.

[50] Gear, C.W. and Osterby, O., 1984, "Solving Ordinary Differential Equations with Discontinuities," *ACM Trans. Math. Softw.*, **10**(1), pp. 23–44.

[51] Geist, K., Parlitz, U., and Lauterborn, W., 1990, "Comparison of Different Methods for Computing Lyapunov Exponents," *Prog. Theor. Phys.*, **83**(5), pp. 875–893.

[52] Tancredi, G., Snchez, A., Roig, F., and Brasil, P., 2001, "A Comparison Between Methods to Compute Lyapunov Exponents," *AJ*, **121**(2).

[53] Wolf, A., Swift, J.B., Swinney, H.L., and Vastano, J.A., 1985, "Determining Lyapunov Exponents from a Time Series," *Physica D: Nonlinear Phenomena*, **16**(3), pp. 285 – 317.

[54] Rossler, O., 1976, "An Equation for Continuous Chaos," *Physics Letters A*, **57**(5), pp. 397 – 398.

[55] Mario, B., Budd, C., A.R., C., and Kowalczyk, P., *Piecewise-Smooth Dynamical Systems: Theory and Applications*, Springer, 1st edition.

[56] Llibre, J., Novaes, D.D., and Teixeira, M.A., 2015, "On the Birth of Limit Cycles for Non-Smooth Dynamical Systems," *Brazilian Sci. Math.*, **139**(3), pp. 229–244.

[57] Llibre, J., Mereu, A.C., and Novaes, D.D., 2015, "Averaging Theory for Discontinuous Piecewise Differential Systems," *J. Differ. Equ.*, **258**(11), pp. 4007–4032.

[58] Miino, Y., Ito, D., and Ueta, T., 2015, "A Computation Method for Nonautonomous Systems with Discontinuous Characteristics," *Chaos, Solitons and Fractals*, **77**, pp. 277–285.

[59] Kousaka, T., Ueta, T., and Kawakami, H., 1999, "Bifurcation of Switched Nonlinear Dynamical Systems," *IEEE Trans. Circuits Syst. II. Analog Digit. Signal Process.*, **46**(7), pp. 878–885.

[60] Kousaka, T., Ueta, T., Ma, Y., and Kawakami, H., 2005, "Bifurcation Analysis of a Piecewise Smooth System with Non-Linear Characteristics," *Int. J. Circ. Theor. App.*, **33**(4), pp. 263–279.

[61] Dhooge, A., Govaerts, W., and Kuznetsov, Y.A., 2003, "MATCONT: A MATLAB Package for Numerical Bifurcation Analysis of ODEs," *ACM Trans. Math. Softw.*, **29**(2), pp. 141–164.

[62] Dercole, F. and Kuznetsov, Y.A., 2005, "SlideCont: An Auto97 Driver for Bifurcation Analysis of Filippov Systems," *ACM Trans. Math. Softw.*, **31**(1).

[63] Thota, P. and Dankowicz, H., 2008, "TC-HAT (T): A novel toolbox for the continuation of periodic trajectories in hybrid dynamical systems," *SIAM Journal on Applied Dynamical Systems*, **7**(4), pp. 1283–1322.

[64] Dankowicz, H. and Schilder, F., 2013, *Recipes for Continuation*, Society for Industrial and Applied Mathematics, Philadelphia, PA, 1st edition.

[65] Tsumoto, K., Ueta, T., Yoshinaga, T., and Kawakami, H., 2012, "Bifurcation Analyses of Nonlinear Dynamical Systems: From Theory to Numerical Computations," *Nolta IEICE*, **3**(4), pp. 458–476.

[66] Zhu, D., Tudor, M.J., and Beeby, S.P., 2009, "Strategies for Increasing The Operating Frequency Range of Vibration Energy Harvesters : A Review," *Meas. Sci. Technol.*, **21**(2).

[67] Zhou, S., Cao, J., Inman, D.J., Lin, J., and Li, D., 2016, "Harmonic Balance Analysis of Nonlinear Tristable Energy Harvesters for Performance Enhancement," *J. Sound Vib.*, **373**, pp. 223–235.

[68] Zhao, Y., Feng, J., and Tse, C.K., 2009, "Stability Analysis of Periodic Orbits of Systems by Mapping Approach," *IEEE Trans. Circs. Sys. II Exp. Brfs.*, **56**(11), pp. 845–849.

[69] Yue, Y., Xie, J., and Gao, X., 2012, "Determining Lyapunov Spectrum and Lyapunov Dimension Based on the Poincaré Map in a Vibro-Impact System," *Nonlinear Dyn.*, **69**(3), pp. 743–753.

[70] Yang, J.H., Sanjuán, M.A.F., and Liu, H.G., 2016, "Vibrational Subharmonic and Superharmonic Resonances," *Commun. Nonlinear Sci.*, **30**(1), pp. 362–372.

[71] Waters, R., Danielsson, O., and Leijon, M., 2007, "Measuring Air Gap Width of Permanent Magnet Linear Generators Using Search Coil Sensor," *J. Appl. Phys.*, **101**(2).

[72] Verhulst, F., 1996, *Nonlinear Differential Equations and Dynamical Systems*, Springer, 2nd edition.

[73] Van Blarigan, P., 1998, "Advanced Hydrogen Fueled Internal Combustion Engines," *Energy & Fuels*, **12**(1), pp. 72–77.

[74] Tone, Y., Asahara, H., Ito, D., Ueta, T., Aihara, K., and Kousaka, T., 2016, "Calculation of Local Bifurcation Points in Piecewise Nonlinear Discrete-Time Dynamical Systems," *Electr. Commun. Jpn.*, **99**, pp. 729–736.

[75] Tamura, A., Ueta, T., and Tsuji, S., 2009, "Bifurcation Analysis of Izhikevich Neuron Model," *Dyn. Contin. Discret. Impuls. Syst. Ser. A Math. Anal.*, **16**(6), pp. 849–862.

[76] Sun, C., Cao, D., and Duan, J., 2007, "Uniform Attractors for Nonautonomous Wave Equations with Nonlinear Damping," *SIAM J. Appl. Dyn. Syst.*, **6**(2), pp. 293–318.

[77] Strogatz, S.H., 2015, *Nonlinear Dynamics And Chaos*, CRC Press, 2nd edition.

[78] Shutte, J., 2011, "Optimisation of a Transverse Flux Linear Oscillating Generator by Transient 3D Finite Element Analysis," Ph.D. thesis, Stelenbisch University, Stellenbosch, South Africa.

[79] Shangjiang, G. and Jianhong, W., 2013, *Bifurcation Theory of Functional Differential Equations*, Springer, 1st edition.

[80] Scapolan, M., Ghandchi, M., and Bonisoli, E., 2016, "Energy Harvesting Using Parametric Resonant System Due to Time-Varying Damping," *Mech. Syst. Signal Pr.*, **79**, pp. 149–165.

[81] Sanders, J.A., Verhulst, F., and Murdock, J., 2007, *Averaging Methods in Nonlinear Dynamical Systems*, Springer, 2nd edition.

[82] Rajasekar, S. and Sanjuan, M.A.F., 2016, *Nonlinear Resonances*, Springer, 1st edition.

[83] Parthasarathy, R., 2012, "Linear PM Generator for Wave Energy Generation," Master's thesis, Louisiana State University and Agricultural and Mechanical College, USA.

[84] Novaes, D.D., 2015, "Regularization and Minimal Sets for Non-Smooth Dynamical Systems," Ph.D. thesis, Universidade Estadual De Campinas, Brazil.

[85] Nayfeh, A.H. and Mook, D.T., 1979, *Nonlinear Oscillations*, Wiley, 1st edition.

[86] Mikalsen, R. and Roskilly, A.P., 2010, "The Control of a Free-Piston Engine Generator. Part 1: Fundamental Analyses," *Appl. Energy*, **87**(4), pp. 1273–1280.

[87] Mikalsen, R. and Roskilly, A., 2010, "The Control of a Free-Piston Engine Generator. Part 2: Engine Dynamics and Piston Motion Control," *Appl. Energy*, **87**(4), pp. 1281–1287.

[88] Mann, B.P. and Owens, B.A., 2010, "Investigations of a Nonlinear Energy Harvester with a Bistable Potential Well," *J. Sound Vib.*, **329**(9), pp. 1215–1226.

[89] Lovelock, D. and Rund, H., 1989, *Tensors, Differential Forms, and Variational Principles*, Dover.

[90] Leijon, M., Danielsson, O., Eriksson, M., Thorburn, K., Bernhoff, H., Isberg, J., Sundberg, J., Ivanova, I., Sjöstedt, E., Ågren, O., Karlsson, K.E., and Wolfbrandt, A., 2006, "An Electrical Approach to Wave Energy Conversion," *Renew. Energ.*, **31**(9), pp. 1309–1319.

[91] Kunze, M., 2000, "On Lyapunov Exponents for Non-Smooth Dynamical Systems with an Application to a Pendulum with Dry Friction," *J. Dyn. Differ. Equ.*, **12**(1), pp. 31–116.

[92] Kousaka, T., Ueta, T., Ma, Y., and Kawakami, H., 2006, "Control of Chaos in a Piecewise Smooth Nonlinear System," *Chaos Solit. Fract.*, **27**(4), pp. 1019–1025.

[93] Kloeden, P.E. and Rasmussen, M., *Nonautonomous Dynamical Systems*, American Mathematical Society, 1st edition.

[94] Kloeden, P.E., 2006, "Nonautonomous Attractors of Switching Systems," *Dynam. Syst.*, **21**(2), pp. 209–230.

[95] Kawakami, H., 1984, "Bifurcation of Periodic Responses in Forced Dynamic Nonlinear Circuits: Computation of Bifurcation Values of the System Parameters," *IEEE T. Circuits-I*, **31**(3), pp. 248–260.

[96] Karami, M.A. and Inman, D.J., 2011, "Equivalent Damping and Frequency Change for Linear and Nonlinear Hybrid Vibrational Energy Harvesting Systems," *J. Sound Vib.*, **330**(23), pp. 5583–5597.

[97] Joshi, D.D. and Lu, F.K., 2017, "Flow Rate Measurement Method for Gaseous Fuel Injection for Pulse Detonation Engines," *J. Propul. Power*, **33**(1), pp. 144–152.

[98] Joseph, D.M., 2010, "A Double-Sided Tubular Linear Synchronous Generator for Wave-Energy Conversion," Ph.D. thesis, University of the Witwatersrand, Johannesburg, South Africa.

[99] Awrejcewicz, J. and Lamarque, C.H., 2003, *Bifurcation and Chaos in Nonsmooth Nechanical Systems*, World Scientific, 1st edition.

[100] Iggidr, A. and Sallet, G., 2003, "On the Stability of Nonautonomous Systems," *Automatica*, **39**, pp. 167–171.

[101] Hosseinloo, A.H. and Turitsyn, K., 2015, "Fundamental Limits to Nonlinear Energy Harvesting," *Phys. Rev. Appl*, **4**, pp. 1–8.

[102] Harne, R.L., Zhang, C., Li, B., and Wang, K.W., 2016, "An Analytical Approach for Predicting the Energy Capture and Conversion by Impulsively-Excited Bistable Vibration Energy Harvesters," *J. Sound Vib.*, **373**, pp. 205–222.

[103] Green, P.L., 2012, "Nonlinear Energy Harvesting," Ph.D. thesis, University of Sheffield, England.

[104] Gouveia, M.R.A., Llibre, J., and Novaes, D.D., 2015, "On Limit Cycles Bifurcating From the Infinity in Discontinuous Piecewise Linear Differential Systems," **271**, pp. 365–374.

[105] Finogenko, I.A., 2016, "Method of Limit Differential Equations for Nonautonomous Discontinuous Systems," *Doklady Mathematics*, **93**(1), pp. 16–19.

[106] Ekström, R., Ekergård, B., and Leijon, M., 2015, "Electrical Damping of Linear Generators for Wave Energy Converters - A Review," *Renew. Sustain. Energy Rev*, **42**, pp. 116–128.

[107] Dosiek, L. and Pillay, P., 2007, "Cogging Torque Reduction in Permanent Magnet Machines," *IEEE Trans. Ind. Appl.*, **43**(6), pp. 1565–1571.

[108] Desalvo, J.A., 2010, "A Cross Section of Oscillator Dynamics," Master's thesis, University of Colorado, Boulder, USA.

[109] Colvin, M.C., 2010, "Energy Sinks with Nonlinear Stiffness and Nonlinear Damping," Master's thesis, University of Maryland, College Park.

[110] Coll, B., Gasull, A., and Prohens, R., 2012, "Periodic Orbits for Perturbed Non-Autonomous Differential Equations ," *Brazilian Sci. Math.*, **136**(7), pp. 803–819.

[111] Chicone, C., 1994, "Lyapunov-Schmidt Reduction and Melnikov Integrals for Bifurcation of Periodic Solutions in Coupled Oscillators ," *J. Diff. Equ.*, **112**(2), pp. 407–447.

[112] Cheban, D.N., *Global Attractors of Non-Autonomous Dynamical and Control Systems*, World Scientific, 2nd edition.

[113] Cawthorne, W.R., 1999, "Optimization of a Brushless Permanent Magnet Linear Alternator for Use With a Linear Internal Combustion Engine," Ph.D. thesis, West Virginia University, Morgantown, USA.

[114] Buica, A., Llibre, J., and Makarenkov, O., 2012, "Bifurcations from Nondegenerate Families of Periodic Solutions in Lipschitz Systems," *J. Differ. Equ.*, **252**, pp. 3899–3919.

[115] Boldea, I. and Nasar, S.A., 1997, *Linear Electric Actuators and Generators*, Cambridge, 1st edition.

[116] Boldea, I. and Nasar, S.A., 1987, "Permanent-Magnet Linear Alternators Part I: Fundamental Equations," *IEEE Trans. Aerosp. Electron.*, **AES-23**(1), pp. 73–78.

[117] Boldea, I. and Nasar, S.A., 1987, "Permanent-Magnet Linear Alternators Part II: Design Guidelines," *IEEE Trans. Aerosp. Electron.*, **AES-23**(1), pp. 79–82.

[118] Biemond, B., 2012, "Nonsmooth Dynamical Systems: On Stability of Hybrid Trajectories and Bifurcations of Discontinuous Systems," Ph.D. thesis, Technische Universiteit Eindhoven, Netherlands.

[119] Bernardo, M., Budd, C.J., Champneys, A.R., Kowalczyk, P., Nordmark, A.B., Tost, G.O., and Piiroinen, P.T., 2008, "Bifurcations in Nonsmooth Dynamical Systems," *SIAM Review*, **50**(4), pp. 629–701.

[120] Ageno, A. and Sinopoli, A., 2005, “Lyapunov’s Exponents for Nonsmooth Dynamics with Impacts: Stability Analysis of the Rocking Block,” *Int. J. Bifurc. Chaos Appl. Sci. Eng*, **15**(06), pp. 2015–2039.

[121] Wu, Y., Ma, F., and Yang, V., 2003, “System Performance and Thermodynamic Cycle Analysis of Airbreathing Pulse Detonation Engines,” *J. Propul. Power*, **19**(4), pp. 556–567.

[122] Fickett, W. and Davis, W.C., 2000, *Detonation: Theory and Experiment*, Dover.

[123] Litchford, R.J., Thompson, B.R., and Lineberry, J.T., 2000, “Pulse Detonation Magnetohydrodynamic Power,” *J. Propul. Power*, **16**(2), pp. 251–262.

[124] Bykovskii, F.A., Vedernikov, E.F., Polozov, S.V., and Golubev, Y.V., 2007, “Initiation of Detonation in Flows of Fuel-Air Mixtures,” *Combust. Explos. Shock Waves*, **43**(3), pp. 345–354.

[125] Bykovskii, F.A. and Mitrofanov, V.V., 1980, “Detonation Combustion of a Gas Mixture in a Cylindrical Chamber,” *Combust. Explos. Shock Waves*, **16**(5), pp. 570–578.

[126] Panicker, P.K., 2008, “The Development and Testing of Pulsed Detonation Engine Ground Demonstrators,” Ph.D. thesis, The University of Texas at Arlington, USA.

[127] Nicholls, J., Wilkinson, H., and Morrison, R., 1957, “Intermittent Detonation as a Thrust-Producing Mechanism,” *J. Jet Propuls.*, **27**(5), pp. 534–541.

[128] Aziz, A.K., Hurwitz, H., and Sternberg, H.M., 1961, “Energy Transfer to a Rigid Piston under Detonation Loading,” *Phys. Fluids*, **4**(3), pp. 380–384.

[129] Kailasanath, K., 2000, “Review of Propulsion Applications of Detonation Waves,” *AIAA Journal*, **38**(9), pp. 1698–1708.

[130] Kailasanath, K., 2003, “Recent Developments in the Research on Pulse Detonation Engines,” *AIAA Journal*, **41**(2), pp. 145–159.

BIOGRAPHICAL STATEMENT

Umang Umeshkumar Dighe was born in Ankleshwar, Gujarat, India in 1987. He received his undergraduate degree from Veer Narmad South Gujarat University, India, in 2009. Following his undergraduate education, he moved to United States in August 2009 for his masters degree in mechanical engineering from the University of Texas at Arlington (UTA). After the completion of his M.Engr degree, he worked as a design engineer in Ohio for 2 years. In late 2014, he returned to graduate school at UTA to pursue a doctoral degree in aerospace engineering. During the course of the doctoral degree, he conducted multidisciplinary research and was the recipient of a Graduate Teaching Assistantship. He also taught graduate gas dynamics and undergraduate fluid mechanics classes for two semesters in the mechanical and aerospace engineering department at UTA as an adjunct faculty.

In his free time, he enjoys cooking, camping and stargazing.